Titre: Title:	Purity and Tunability of a Highly Stable Hybrid Laser
Auteur: Author:	Mamoun Wahbeh
Date:	2016
Type:	Mémoire ou thèse / Dissertation or Thesis
Référence: Citation:	Wahbeh, M. (2016). Purity and Tunability of a Highly Stable Hybrid Laser [Thèse de doctorat, École Polytechnique de Montréal]. PolyPublie. https://publications.polymtl.ca/2429/

URL de PolyPublie: PolyPublie URL:	https://publications.polymtl.ca/2429/
Directeurs de recherche: Advisors:	Raman Kashyap
Programme: Program:	génie électrique

UNIVERSITÉ DE MONTRÉAL

PURITY AND TUNABILITY OF A HIGHLY STABLE HYBRID LASER

MAMOUN WAHBEH
DÉPARTEMENT DE GÉNIE ÉLECTRIQUE
ÉCOLE POLYTECHNIQUE DE MONTRÉAL

THÈSE PRÉSENTÉE EN VUE DE L'OBTENTION
DU DIPLÔME DE PHILOSOPIAE DOCTOR
(GÉNIE ÉLECTRIQUE)
NOVEMBRE 2016

UNIVERSITÉ DE MONTRÉAL

ÉCOLE POLYTECHNIQUE DE MONTRÉAL

Cette thèse intitulée:

PURITY AND TUNABILITY OF A HIGHLY STABLE HYBRID LASER

présenté par : WAHBEH Mamoun

en vue de l'obtention du diplôme de : Philosophiae Doctor

a été dûment acceptée par le jury d'examen constitué de :

M. WU Ke, Ph. D., président

M. KASHYAP Raman, Ph. D., membre et directeur de recherche

M. CARDINAL Christian, Ph. D., membre

M. KABIR M. Zahangir, Ph. D., membre externe

DEDICATION

To my family

ACKNOWLEDGEMENTS

The results included in this thesis represent not only a milestone in more than four years of work. They are also tangled with precious memories of great people, without whom this work would not have seen the light and to whom I would like to express my sincere appreciation.

I would like to thank my research director, Prof. Raman Kashyap, for his thoughtful guidance and encouragement. He has supported me throughout my work. Particularly at key moments, he has always been there, supporting with his continuous effort and offering inspiring expectations.

I would like to thank my colleagues: Mathieu Gagné, Sébastien Loranger, Elton Soares de Lima Filho, Jérôme Lapointe and Victor Lambin Iezzi. Every one of those wonderful people has contributed to my work in his own way that I will never forget. One of them is my colleague and friend Mohamad Diaa Baiad, to whom I would like to express my personal thanks for his lovely presence and willingness to support.

Many thanks go to the laboratory support team at the Poly-Grames Research Center. In particular, Mr. Steve Dubé and Mr. Jules Gauthier, whose technical support has been essential for my experiments, and Mr. Jean-Sébastien Décarie for his help with IT-related issues.

Above all, I am more thankful than I can express to my parents, my wife and my brother for their endless love, care and support.

RÉSUMÉ

Les sources laser ayant une structure simple et compacte et à faible coût sont un but ultime pour les industriels. En effet, plusieurs applications, telles que la détection et localisation de la lumière, la météorologie optique et la détection cohérente dans les systèmes de communication, exigent une largeur de ligne étroite ainsi qu'une source laser assez stable. À titre d'exemple, La course incessante vers des capacités de transmission de données de plus en plus importantes dans les systèmes de télécommunications avait comme conséquence le déploiement de la méthode d'accès : multiplexage de longueur d'onde ultra dense au sein de la bande de fréquences optiques. Toutefois, à cause du volume du trafic de données et l'augmentation incessante de la demande des utilisateurs, la conception de sources laser ayant une efficacité spectrale plus importante, une meilleure stabilité et une précision plus performante représente un défi sans précédent surtout pour les systèmes de détection cohérente. La stabilité et la largeur de bande étroite réduisent considérablement la dispersion inter modale et améliorent ainsi l'efficacité spectrale. Selon le critère de Shannon, la suppression du rapport des modes secondaires qui est indépendant du courant d'alimentation, a pour conséquence l'augmentation de la capacité d'un canal alloué ainsi qu'éviter des effets non linéaires qui se produisent lors de l'utilisation des puissances importantes. En effet, le potentiel spectral d'une fibre optique peut être amélioré en s'appuyant sur un control assez précis de la longueur d'onde utilisée. Jusqu'à présent, ces critères sont mis en évidence par le biais de systèmes haute gamme qui sont assez chers, de structures complexes et de taille assez grande. Au sein de cette thèse, on présente un laser hybride de taille compacte, ayant une structure trop simple, opérant à une largeur de ligne qui est au plus égale à 2 kHz, ayant un rapport de suppression modale supérieur à 40 dB et présentant une excellente stabilité sur une plage de 22 Hz. Un prototype assez simple a été réalisé dans le but de montrer en pratique les performances déjà évoquées.

Ce travail se focalise sur la combinaison des caractéristiques des fibres Bragg, de la fibre dopée de type polarization maintaining erbium ainsi que celles de l'amplificateur optique semi-conducteur tout au sein d'un laser hybride. Le prototype conçu a été fabriqué soigneusement et assemblé de manière à garantir une pureté spectrale assez considérable. En fait, la fibre Bragg a été insérée directement à l'intérieur de la fibre dopée dont l'absorption mesurée était de l'ordre de 30 dB aux alentours de la longueur d'onde 1528 nm. Alors que la fibre Bragg constitue le premier réflecteur, le second miroir qui ferme la cavité résonnante est localisé sur la facette haute de l'amplificateur optique à base de semi-conducteurs. L'autre facette est anti-réflectrice et couplée à la fibre par le

biais de microlentilles et elle sculptée sur la fibre à une distance de 34 cm de la fibre Bragg. Bien évidemment, la cavité de la fibre est totalement faite à base de fibre dopée de type polarization maintaining erbium. L'amplificateur semi-conducteur optique est monté sur un dissipateur de chaleur qui lui est placé sur un refroidisseur thermoélectrique de type Peltier. La cavité fibrée est enroulée autour d'un tambour dans une rainure en forme de U de 280 µm de large. La résistance électrique de chaque thermistor ainsi que le parcourt thermique entre le refroidisseur thermoélectrique et l'amplificateur semi-conducteur sont optimisés. Le fait que la cavité est totalement remplie des ions erbium a pour conséquence une auto-induction dynamique grillée, qui fonctionne à la manière d'un filtre coupe bande ce qui mène à la création d'un mode opératoire mono modal. À cause de la durée de vie de l'état haut de l'erbium (10 ms), le grillage de longue de durée de vie stabilise la fréquence d'opération et impose une limite maximale de 100 Hz pour la fréquence de coupure. L'utilisation de la fibre de type polarization maintaining erbium présente une contrainte énergétique pour l'intensité de l'onde stationnaire tout le long d'un seul axe de la cavité de la fibre. Cela augmente la probabilité de générer des transitions électroniques non-radiatives dans les niveaux supérieurs des ions d'erbium. Par conséquent, cela peut induire une recirculation coopérative de la population d'ions des niveaux supérieurs à long temps de vie avec les deux niveaux supérieurs. Ainsi, un mécanisme de stabilisation fréquentiel peut être établit en incorporant un filtrage par un réseau de Bragg dynamique avec ce processus de recirculation, processus qui permet de résister aux fluctuations de basses fréquences causées par la pénétration dans le réseau de Bragg. La génération de chaleur associée avec les transitions non-radiatives est dissipée efficacement par le refroidisseur thermoélectrique, soit celui utilisé dans cette nouvelle configuration de dispositif où un contrôleur de température à haute précision est optimisé expérimentalement. Le bruit thermique, limité par l'erreur en régime permanent de la boucle de rétroaction PID et qui affecte la longueur optique de la cavité fibrée, est ainsi minimisé à un niveau qui n'est pas « vue » par le mode oscillant grâce à au mécanisme de stabilisation en fréquence.

Désormais, en ne tenant pas en considération les effets des perturbations mécaniques et environnementales, on remarque que la stabilité fréquentielle obtenue et qui est de l'ordre de ±11 Hz ainsi que la longueur de ligne de 2.26 kHz n'ont jamais été rapportées en littérature. En effet, ces mesures sont faites à base de la technique d'auto battement et dans des conditions d'opération normales. Si le système n'est pas emballé, il sera sujet aux perturbations extérieures et la fréquence sera tenue à un mode d'opération de l'ordre d'un neuvième de l'espacement modal.

Au sein de ce travail de thèse, on a aussi présenté les résultats concernant la réalisation d’un réglage à précision linéaire ayant une résolution de l’ordre de 2.17 MHz/mA. Le réglage linéaire continu et le courant d’alimentation ont permis un balayage spectral au sein d’un seul espacement modal de 298 MHz. En fait, en alternant la température de la fibre Bragg externe, un balayage d’une bande de 1.78 GHz à une résolution de 178 MHz est rendu possible sans aucun saut modal. Ainsi, l’importance de ce travail se traduit dans la réalisation d’un transfert linéaire et précis du réglage qui est commandé par une source de courant bien sélectionnée (exemple : ~2 kHz/μA). Ceci peut être bien établit pour n’importe quelle fréquence d’un canal assez large qui est balayé en faisant le réglage thermique de la longueur d’onde Bragg.

ABSTRACT

Cost-effective, simple structure and compact laser sources with high spectral quality are sought by many segments of industry. Diverse applications require narrow linewidth and highly stable laser sources such as in light detection and ranging, optical frequency metrology and coherent detection communications. For instance in the telecommunication industry, the growing problem of transmission capacity congestion has led to the deployment of the dense wavelength-division-multiplexed systems utilizing the broad spectral window of optical fiber links. However, owing to the rapidly rising data-traffic volume and ever increasing demand for higher transmission capacities, portable laser sources with higher spectral purity, excellent stability and better accuracy form a significant milestone for a solution, especially in coherent detection. Such high stability and narrow linewidth reduces the intra-modal dispersion and hence, enhance the spectral efficiency. According to the Shannon limit, a high side-mode suppression ratio that is independent of the drive current increases the capacity of an allocated channel, while severe nonlinear effects emerging at high powers are avoided. In this case, the full potential bandwidth of fiber communication links can be exploited through a high precision wavelength control. To date, those needs are fulfilled by lasers that are usually bench-top systems, prohibitively expensive, large in size and high in complexity. In this dissertation, we report on a realization of a compact size, simple structure hybrid laser operating with ~2-kHz or less linewidth, more than 40-dB of side mode suppression ratio and featuring an excellent stability within 22 Hz. A simple and user-friendly device that may fulfill the stringent requirements of the above mentioned applications.

This work focuses on combining attributes of a fiber Bragg grating, polarization-maintaining erbium-doped fiber and semiconductor optical amplifier in a hybrid laser. The demonstrated single-frequency device is carefully engineered and assembled to operate with high spectral purity. The fiber Bragg grating is inscribed directly into the polarization-maintaining erbium doped fiber, whose absorption was measured at 1528 nm to be ~30 dB. While this grating constitutes the first reflector, the second mirror closing the cavity resonator is located at the high reflection coated facet of the semiconductor optical amplifier. The other facet is anti-reflection coated and coupled to the fiber via a micro-lens, sculpted on the fibre tip ~34 cm away from the fiber Bragg grating. Eventually, the fiber cavity is fully made of polarization-maintaining erbium-doped fiber. The semiconductor optical amplifier is mounted on a heatsink, placed on a thermoelectric cooler. The fiber cavity is spooled in a circular 280-μm wide U-groove, engraved on a copper substrate that is mounted on a thermoelectric cooler. The resistance of each thermistor and thermal paths between the thermoelectric cooler and semiconductor amplifier/fiber Bragg grating are optimized. The full occupation of erbium ions in the fiber cavity leads to a self-induced dynamic grating, which functions as a fine band-stop filter giving rise to single mode operation. Owing to the lifetime of the erbium upper state (~10 ms), this long-lived grating stabilizes the operating frequency as it imposes a maximum cut-off frequency of ~100 Hz on the instabilities that can be sensed by the operating mode. The use of polarization-maintain fiber constrains the energy of the standing wave intensity in a single-axis plane along the fiber cavity. This increases the probability of initiating non-radiative electronic transitions among upper energy levels of erbium ions. Consequently, this may give rise to a recirculation of ion population of the long-lived upper energy level cooperatively with two upper levels. As a result, a frequency-stabilizing mechanism may be established by incorporating the filtering effect of the dynamic grating with the recirculating process's resistivity to low-frequency disturbances allowed by that filter. Heat generation associated with the non-radiative transitions is efficiently dissipated by a thermoelectric cooler, used in the new device set-up where a high precision temperature controller is experimentally optimized. Thus the thermal noise, limited to the PID loop's steady-state error and affects the fiber cavity length, is consequently minimized to a level that cannot be seen by the operating mode due to the effect of the frequency-stabilizing mechanism.

Excluding the effect of mechanical and environmental disturbances on the cavity length, the long-term frequency stability is unprecedentedly demonstrated to be within ±11 Hz while the long-term linewidth is 2.26 kHz, measured using the self-beating technique under free running conditions. In the case of unpackaged device that is exposed to environmental perturbations and external noise, the lasing frequency is successfully locked to a particular operating mode within a long-term stability of one-ninth of the mode spacing. In this work, we report on a realization of a linear precision tunability at a resolution of 2.17 MHz/mA. Fully continuous linear tuning with the drive current is found to scan a spectral range within a single mode spacing of 298 MHz. Moreover by altering temperature of the external fiber Bragg grating, a range of 1.78 GHz is scanned without mode hops at a resolution of ~178 MHz. The significance of this work can be realized by transferring linear precision tunability, driven by a suitable precision current source, e.g. ~2 kHz/μA, to any operating frequency within a broad spectral channel that can be scanned by thermally tuning the Bragg wavelength.

TABLE OF CONTENTS

LIST OF TABLES

LIST OF FIGURES

LIST OF ABBREVIATIONS

AR	Anti-Reflection
CET	Cooperative Energy Transfer
DBR	Distributed Bragg Reflector
DFB	Distributed Feedback
EC	External Cavity
ED	Erbium Doped
Er^{3+}	Erbium Ion
ESA	Electrical Spectrum Analyzer
FBG	Fiber Bragg Grating
FWHM	Full Width At Half Maximum
HR	High Reflection
OSA	Optical Spectrum Analyzer
PID	Proportional–Integral–Derivative
PM	Polarization Maintaining
RBW	Resolution Bandwidth
SMSR	Side-Mode Suppression Ratio
SOA	Semiconductor Optical Amplifier
TEC	Thermo-Electric Cooler

T-matrix	Transfer Matrix
UV	Ultra Violet
WDM	Wavelength Division Multiplexing

CHAPTER 1 INTRODUCTION TO HYBRID LASERS

1.1 Semiconductor laser diodes

Semiconductor laser diodes industry has gone through a dramatic evolution since the early 1960s. Laser diodes are compact, efficient, easy to use and low-cost but they usually suffer from serious performance limitations that do not outfit the strict requirements of modern applications. From this perspective, multimode operation, short cavity photon lifetime, high phase noise and broad linewidth are the main drawbacks [1]. They therefore operate with poor wavelength control and low stability. Although the wavelength tunability is possible by varying bias current or temperature, it is limited to small ranges of the broad gain-bandwidth, offered by the active region of semiconductor Fabry-Perot laser diodes [2].

Understanding multimode operation of a laser diode can be a good starting point. This may be attained by determining the lasing conditions and resonant frequencies as follows. The electric field of the wave propagating along x-axis throughout the cavity length, L , and normal to the mirrors is

$$E(x,t)=A(x)e^{j(\omega t-\beta x)}, \tag{1.1}$$

Where $A(x)$ is the amplitude, t stands for time, ω is the angular frequency and the propagation constant is

$$\beta=2\pi\frac{n}{\lambda}, \tag{1.2}$$

where n is the refractive index of the cavity medium. The lasing condition at the resonant frequencies can be satisfied when the amplitude and phase of the original wave are equal to those of the returned wave [3], which can be expressed as

$$\begin{gathered} A(0)=A(2L) \\ 1=e^{-j2\beta L}. \end{gathered} \tag{1.3}$$

This condition gives

$$\cos(2\beta L) = 1 \Rightarrow 2\beta L = m\left(2\pi\right) \\ \beta L = m\pi, \tag{1.4}$$

where m is an integer, which can be written as

$$m = \frac{L}{\frac{\lambda}{2n}}. \tag{1.5}$$

Using the speed of light in vacuum $c = f\,\lambda$, Eq. (1.5) becomes

$$m = 2\frac{nL}{c}f\,, \tag{1.6}$$

where f is the frequency and λ is the wavelength. Thus, the cavity resonates with a standing wave when the optical cavity length, $n\,L$, between the two mirrors is an integer number of half-wavelengths. Multimode operation is therefore possible in the Fabry-Perot cavity of a laser diode, such as gain-guided laser diodes [4] as shown in Figure 1.1.

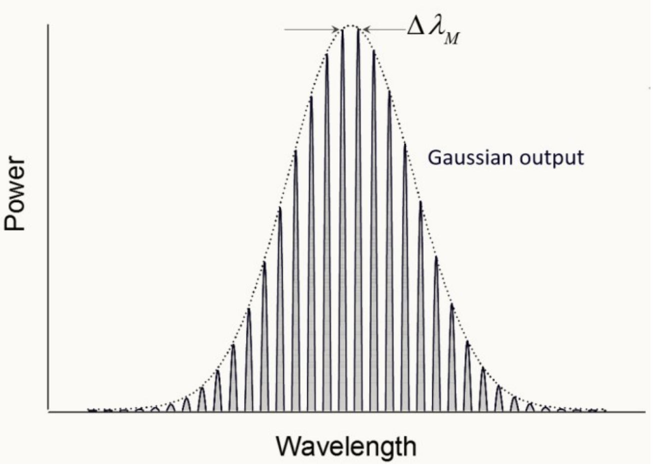

Figure 1.1: Gaussian output profile of a gain-guided laser spectrum illustrating multimode operation and the mode spacing, $\Delta\lambda_M$, separating successive modes.

The free spectral range (FSR) of the Fabry-Perot cavity, which is also referred to as the mode spacing Δf_M, is the spectral spacing between two successive modes operating at resonant frequencies f_m and f_{m+1} and can be obtained from Eq. (1.6)

$$\begin{aligned} \Delta m &= 2\frac{nL}{c}\left(f_{m+1} - f_m\right) \Rightarrow 1 = 2\frac{nL}{c}\,\Delta f_M, \\ \Delta f_M &= \frac{c}{2nL}. \end{aligned} \tag{1.7}$$

In terms of wavelength, $f = \frac{c}{\lambda} \Rightarrow \Delta f = c\frac{\Delta \lambda_M}{\lambda^2}$, which is substituted in Eq. (1.7) to get the mode spacing as

$$\Delta \lambda_M = \frac{\lambda^2}{2nL}. \tag{1.8}$$

1.2 Intracavity grating structures

In order to get a single frequency device with a reliable mechanism providing wavelength control, an internal grating structure acting as a wavelength selective element is placed within the laser cavity. This arrangement is usually categorized into three major configurations: distributed feedback (DFB) lasers, distributed Bragg reflector (DBR) lasers and external cavity (EC) lasers. These will now be discussed in the following sections.

1.2.1 Distributed feedback laser

A grating structure integrated into the cavity of a DFB laser is illustrated in Figure 1.2(a), where the grating period is defined as Λ. The grating acting as a Bragg reflector is incorporated continuously along the device and is closely coupled to the active region [5]. In this manner, non-spectral selective reflections of the Fabry-Perot cavity are replaced by the grating optical feedback, whose cumulative net reflection is limited to a narrow spectral bandwidth and centered at the Bragg wavelength, λ_B, given as

$$\lambda_B = 2 n_{eff} \Lambda, \tag{1.9}$$

where n_{eff} is the effective refractive index.

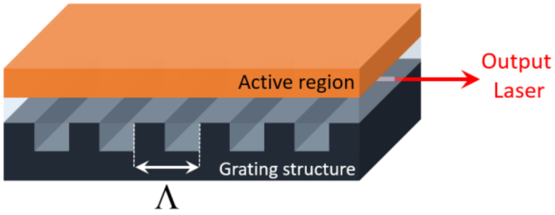

(a)

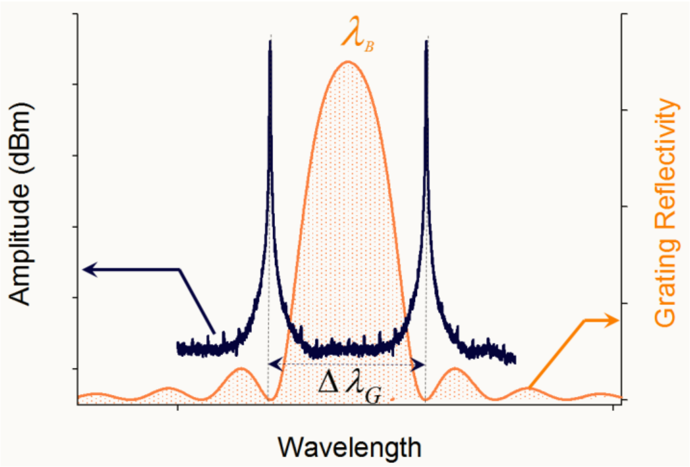

(b)

Figure 1.2: (a) Schematic of a DFB laser demonstrating the distributed grating structure along the laser cavity with a grating period of Λ. (b) Reflectivity of the grating structure of a DFB laser as a function of the wavelength (orange line) is shown along with the operating modes (dark blue line). The grating reflectivity bandwidth, $\Delta\lambda_G$, is limited by the first-zeros of reflectivity, at which the phase mismatch is maximum leading to dual-wavelength operation where the Bragg wavelength, λ_B, is in the middle of operating modes separation.

As a matter of fact, the light propagating at the precise Bragg wavelength cannot resonate within the distributed grating. This is because the light propagating in one direction is reflected back to propagate in the other. In the middle of such a grating, the counter-propagating lights are exactly out of phase leading to a high net reflection. Consequently in order for transmission resonance to occur, the wavelength of the propagating light has to slip away from the exact Bragg wavelength to accumulate some reflection from a span of the grating structure. The phase mismatch, needed to gain a cumulative constructive interference for lasing to take place, is maximum outside of the grating bandwidth [6], at the first zeros of the grating reflectivity as shown in Figure 1.2(b). Thus, there will be a gap at the Bragg wavelength. On the two sides of this gap, two modes of equal threshold operate symmetrically [7]. Hence, this grating leads to two operating modes [8]. In practical applications where single-mode operation at a predictable wavelength is desired, this degeneracy is a disadvantage. This problem was solved by designing quarter-wave-shifted DFB lasers, in which the DFB grating is quarter wavelength-shifted in the middle as shown in Figure 1.3(a). The shift is given as

$$\delta = n_{eff}\frac{\Lambda}{2} = \frac{\lambda_B}{4}. \tag{1.10}$$

This shift within the grating structure incorporates a phase jump of π opening up a spectral pass-band, splitting of the reflection bandwidth in the middle [6] as shown in Figure 1.3(b). As a result, single mode operation is achieved [9].

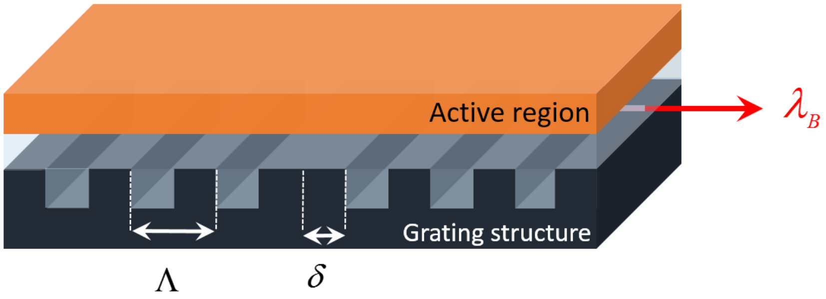

$$\delta = \frac{n_{eff}\Lambda}{2} = \frac{\lambda_B}{4}$$

(a)

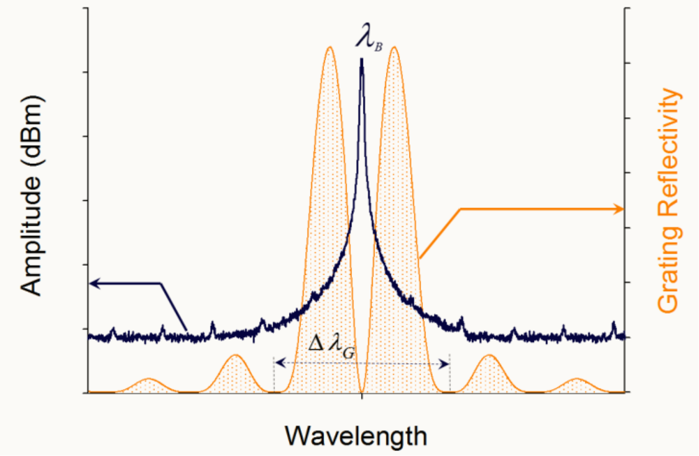

(b)

Figure 1.3: (a) Schematic representation of a quarter-wave-shifted FB laser showing the distributed grating structure shifted in the middle, which gives rise to a phase shift of π. (b) Reflectivity of the quarter wavelength-shifted grating structure of the DFB laser as a function of the wavelength (orange line) illustrating the spectral pass-band in the middle of the reflection bandwidth, $\Delta\lambda_G$. Single mode operation occurs at λ_B (dark blue line).

In order to avoid wasting power of a DFB laser, one facet may be high-reflection (HR) coated. This may also offer a folded phase-shifted cavity that can never be controlled exactly for manufacture while the output facet is usually anti-reflection (AR) coated. The laser performance is therefore determined by the position of the HR coated facet with respect to the grating phase. However, the majority of DFB lasers with HR rear facet have usually ample selectivity leading to single mode operation.

1.2.2 Distributed Bragg reflector laser

The grating structure(s) in DBR lasers is distributed outside the active region as shown in Figure 1.4(a,b) [10]. The cavity loss is minimum for the longitudinal mode at the Bragg wavelength and increases substantially for other modes. The grating reflectivity is hence maximum for the mode at the Bragg wavelength satisfying Eq. (1.9).

DBR lasers are longer than DFB lasers, whose output powers are usually not as high as those of DBR lasers. This is due to the relative short cavity length of DFB lasers in addition to their emission power from both AR coated facets in the case of quarter wavelength-shifted grating. DFB lasers have a lower threshold owing to the higher coupling efficiency between the gain medium and the Bragg reflector. The early 1980s saw a great deal of work involved in achieving single-frequency semiconductor lasers. DFB and DBR lasers were then presented as the best choice for widespread use while the telecommunication companies realized eventually that those devices would better serve their needs [2].

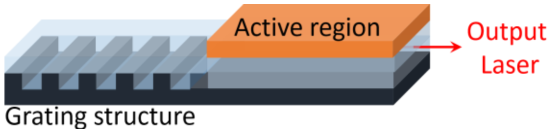

(a)

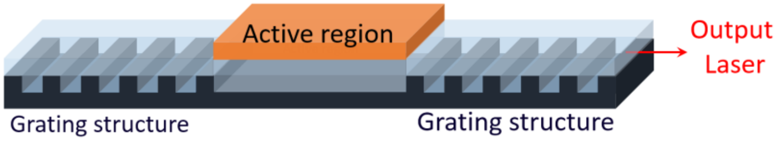

(b)

Figure 1.4: (a) Schematic of a DBR laser illustrating a single grating structure, placed outside the active region, and (b) a DBR laser terminated by two gratings on either side.

1.2.3 External cavity laser

An EC laser is made up of a semiconductor optical amplifier (SOA) coupled to a diffraction grating through a collimating lens. The SOA is a laser diode whose end facet(s) is AR coated as schemed in Figure 1.5. The early 1990s witnessed rising interest in EC lasers for spectroscopic applications and commercial test equipment for fiber optics. One of the key advantages of the EC lasers is the extremely narrow linewidth of a few kHz due to the long cavity photon lifetime, attained by a relatively long cavity.

EC lasers have versatile configurations that are compatible with standard and commercially available SOAs. The common Littrow configuration is shown in Figure 1.5. The cavity is formed between the HR rear facet of the SOA and the grating. The operating frequency is very sensitive to the optical length of the cavity including any variation in the refractive index of the cavity media.

The grating orientation is determined by the Littrow angle, where the incident and diffracted angles are equal. Using the well-known grating equation, the lasing wavelength can be expressed by

$$\frac{\lambda}{\Lambda} = 2\sin\theta, \tag{1.11}$$

where Λ is the grating period and θ is the incident (and diffracted) angle with respect to the grating normal. The first order diffracted beam ($m = -1$) is coupled back into the laser cavity leading to a standing wave while the zeroth-order diffraction emerges as the output beam.

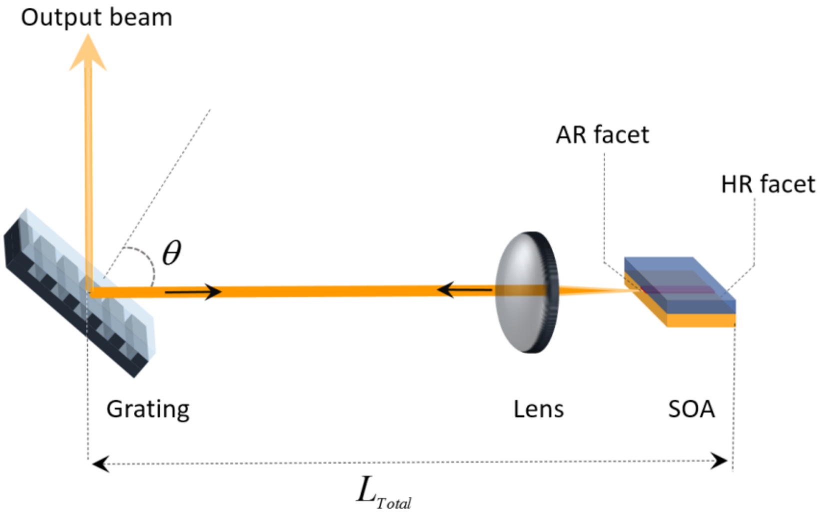

Figure 1.5: Schematic layout of an ECL in Littrow configuration involving an SOA, collimating lens and diffraction grating. The 1st order diffracted wave is reflected back collinear with the original wave and thus, a standing wave is established in the cavity.

Changing θ in Eq. (1.11) by rotating the grating around its axis that is parallel to the groove direction, the laser tunes by hopping from one EC mode to another. As shown in Figure 1.6 in the case of an SOA offering a flat gain over the grating bandwidth, the mode with a highest optical feedback, gained from the grating reflectivity and permitted by the lasing condition, dominates mode competition towards single mode operation. The Littrow configuration suffers from mode-hopping as the grating angle is adjusted to tune the lasing wavelength. A mode hop occurs when the difference between the grating frequency, determined by reflection peak, and the operating frequency, determined by the lasing condition, exceeds half of the mode spacing. Thus, continuous or mode-hop free tuning requires the grating and cavity operating frequency to be superimposed by adjusting cavity length along with changing grating selection. A cumbersome two-step synchronized procedure is therefore required to achieve smooth tuning.

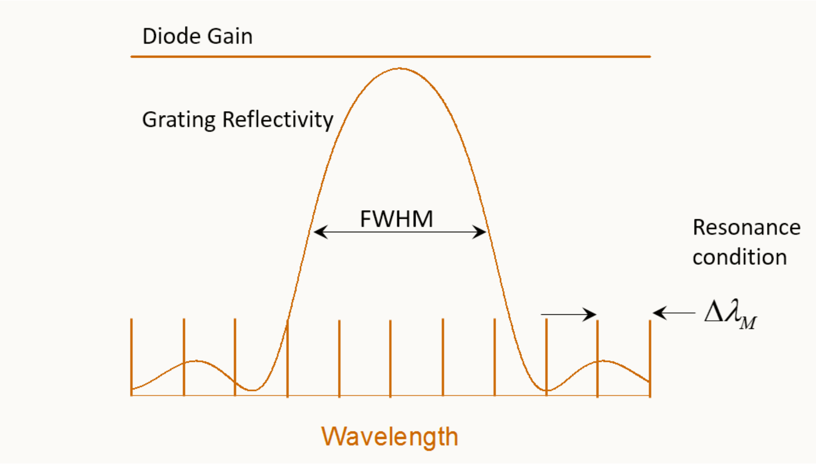

Figure 1.6: Diagram of the factors determining the operating mode of an EC laser. The grating reflectivity is depicted along with the spectral locations of the modes meeting the resonant lasing condition. Those modes are represented by the vertical lines and equally separated by the mode spacing $\Delta\lambda_M$. The mode receiving the highest optical feedback dominates the adjacent modes and hence, single frequency operation is therefore obtained.

1.3 Problem

A mode-hop free tunable single-frequency laser operating with a kHz linewidth can in principle be achieved by a relatively long cavity. However, as the cavity length increases the EC modes get spectrally packed because of decreasing mode spacing as expressed in Eq. (1.8). As a result, three challenging operational complications are imposed:

1) Owing to the wide grating bandwidth relative to the mode spacing, a chaotic behavior of the operating mode may occur. Since the EC modes are spectrally located close to the center of the grating bandwidth within the reflection peak, the operating mode can readily respond to any small gain variation by jumping among those modes [11]. Also under this condition, single-mode operation can easily deteriorate to uneven multimode operation. This design

limitation constitutes the first problematic operational behavior affecting the frequency and intensity stability.

2) The operating wavelength is susceptible to any fluctuations induced by environmental conditions, which affect the cavity optical length and randomly change the refractive index of the cavity media with the pressure and temperature [12]. Also, acoustic disturbances and mechanical vibrations that are combined with the bias current noise broaden the linewidth severely. Moreover, the combination of these external effects or environmental noise disturbs the stability of the output power owing to the loss variation of the laser cavity [13].
3) As can be seen in Figure 1.5, the laser cavity is constructed from discrete components of different media, located between the HR coated facet at one end, and the diffraction grating at the other. This improves the sensitivity of the operating frequency to environmental noise due to, for example, the different thermal expansion of the cavity components, which may simply exacerbate the misalignment amongst those components. This leads to random variations in the power flux and gain relation determining the operating mode [11]. In addition, adding other intracavity parts such as an etalon, in order to enhance wavelength selectivity makes the frequency and intensity stability more vulnerable to the above mentioned noise.

1.4 Motivation & solution

Narrow linewidth single-mode lasers operating with excellent stability and providing precision tunability are sought by many segments of industry. However, a cost-effective, simple structure, robust and compact device is the best to suit not only a wide range of commercial applications but also scientific, military and medical equipment. In other words, high quality laser performance, associated with small footprint, cost-effective components and, of course, capability of mass production, may refine the best technological solution winning the day. The spectral purity offered by the EC laser scheme makes it the most attractive configuration for establishing that solution.

Generally, the first step towards the stability improvement of a long EC laser can be realized by incorporating intracavity filter allowing a single mode to lase, while the adjacent EC modes falling within the grating bandwidth are filtered out. For the first time, this will be demonstrated theoretically and verified experimentally in the presented device. The second step is to make the cavity construction impervious to external noise aforementioned. Thirdly, integrating the lens, wavelength filter and grating reflector into one medium forming the external cavity seems to be a better practical solution to reduce alignment implications, associated with discrete components. This also enhances the device stability and robustness, which facilitates step two as well. The structure of a hybrid laser is thus proposed, where single mode fiber is often utilized as the basis of the external cavity as shown in Figure 1.7. The fiber external cavity is a piece of fiber whose one end is terminated by a fiber Bragg grating (FBG) and the other is sculpted into a lens, through which the fiber cavity is coupled to an SOA.

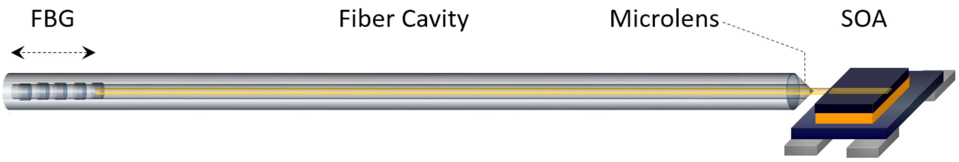

Figure 1.7: Schematic of a hybrid laser that consists of an SOA whose AR coated facet is coupled via a fiber micro-lens to the long fiber cavity, terminated by a short FBG that functions as an external reflector and output coupler.

Using a fiber backbone to construct the external cavity makes the device mechanically rugged and thermally more stable than DFB lasers as the grating, the short FBG, is integrated within the fiber cavity. The deployment of FBGs offers inherently narrower linewidth of the order of a few kilohertz [14] and capability of mass production with lower noise [15] and better predefined wavelength control [16]. In addition, this configuration allows the well-established packaging techniques of DFB lasers to be used, making the fiber EC lasers potentially low cost.

A band-stop filter with a finer resolution than that of the FBG is required in order to build a single-frequency stable device [17]. The dynamic grating based on the self-induced FBG in erbium doped (ED) fiber was impressively deployed in a hybrid laser as a distributed intracavity band-stop filter [18], which improves the selectivity of a single and stable operating mode. Adopting this simple technique, the improvement in performance will be investigated in this work.

1.5 Objectives

The main objective of this work is to provide a potential low cost solution for compact single-frequency lasers operating under free running conditions with ultra-high performance, which can be fully defined by measuring the following operational parameters:

1- Single-mode operation

2- Output power

3- Linewidth and frequency accuracy

4- Side-mode suppression ratio (SMSR)

5- Long-term stability

6- Precision and coarse tunability

This goal can be achieved by designing, assembling and stabilizing hybrid lasers in our laboratory. Special attention will be paid to measure those specifications for any potential application by using high resolution optical and electrical test equipment. The control and test equipment will be remotely controlled and the data acquisition will be synchronized. Eventually, the operating wavelength (frequency), output power, SMSR, fiber cavity temperature and drive current will be recorded simultaneously with high precision. Eventually by studying the relationships among those measurements, the behavior of the hybrid laser device will be theoretically explained and experimentally characterized.

1.6 History of hybrid lasers & literature review

In 1986, Liou *et al* succeeded in reducing the linewidth of a 1.55-µm DFB laser by a factor of 1000 [19]. This was achieved by extending the cavity with 5.5-cm-long fiber as outlined in Figure 1.8. A high reflective mirror was deposited at the fiber end facet and a fiber lens is formed at the other end. Using the lens, the fiber cavity was coupled to the AR coated facet of a DFB laser, whose output facet has a power reflectivity of ~35%. Thus, a Fabry-Perot cavity is established between the fiber mirror and the output facet of the DFB laser.

The DFB grating, which is a relatively weak reflector compared to the cavity mirrors, acted as an intracavity wavelength selector. Owing to sufficient wavelength selectivity provided by the DFB grating, single frequency operation was achievable by the DFB laser before and after extending the cavity and AR coating. However, a 1000-fold reduction in the linewidth of the DFB laser to 70 kHz was achieved. This technology was considered attractive and practical as the fiber is rugged and can be easily fitted in a conventional DFB lase package. In addition, the length of the fiber cavity can be modified to meet specific requirements for coherent detection systems in lightwave communication and interferometric sensors.

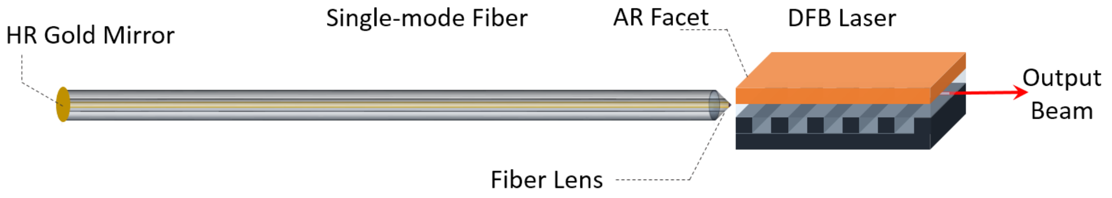

Figure 1.8: Schematic diagram of the fiber external cavity DFB laser. The single-mode fiber cavity is terminated by a HR gold mirror, deposited on the cleaved end, and a micro-lens is formed on the other end that is coupled to the AR coated facet of the DFB.

It was claimed that the high reflectivity of the fiber mirror and strong fiber-chip coupling led to a stable device. Improbably, the stable performance was attributed to the device insensitivity to the external reflection variations, which were negligible compared to the large intracavity photon energy [19]. However, placing the wavelength selective element outside the laser diode could enhance the stability. This is because FBGs have a better temperature stability than that of semiconductor lasers. Explicitly, the temperature sensitivity of the operating wavelength of the semiconductor laser gratings is ~6-8 times higher than that of the fiber Bragg grating [20]. This better stability, in particular, is expected to improve the stability of single-frequency operation of a hybrid laser.

1.6.1 External fiber Bragg grating

In 1986, the use of an in-fiber Bragg grating, FBG, as a wavelength selective element was reported by Brinkmeyer *et al* for the first time [21]. This hybrid laser was built by splicing an etched FBG to the single-mode-fibre pigtail of an uncoated 1.3-µm laser diode. 2-meter-long fiber cavity was constructed and the FBG end constituted the output coupler as illustrated in Figure 1.9. Although the reflectivity of the FBG, $\left|\rho_{FBG}\right|^2 = 0.01\%$, was too small compared to that of the laser diode facet , $\left|\rho_{Diode}\right|^2 = 32\%$, the constructive/destructive interference of the reflectivity amplitudes resulted in a contrast ratio of $\left|\rho_{Diode} + \rho_{FBG}\right|^2 / \left|\rho_{Diode} - \rho_{FBG}\right|^2 \simeq$. This contrast was sufficient for the modes of the external cavity to have a differential gain higher than that of the laser diode. Therefore, the operating modes of the device were tuned to the modes of the external cavity, whose mode spacing is 50 MHz. As the grating bandwidth was 26 GHz, the operating mode was locked to a single mode of the laser diode cavity that had a mode spacing of 140 GHz. Single frequency operation of this device was reported with a linewidth of 60 kHz and output power of 1 mW.

Even though the stability was not presented, this device was, however, found to avoid mechanical adjustments and stability problems, associated with bulk-optical arrangements of air-extended-cavity lasers [22].

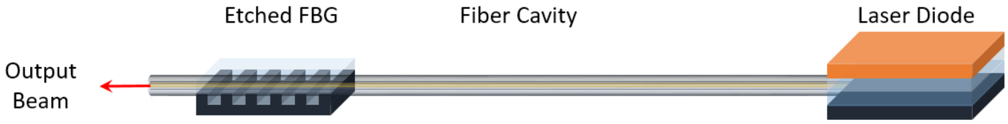

Figure 1.9: Schematic structure of a hybrid laser formed by splicing an etched FBG to the single-mode-fibre of a pigtailed uncoated 1.3-µm laser diode.

Based on an etched FBG integrated within the external cavity, sub-10-kHz linewidth of single frequency operation was also presented by using a standard uncoated 1.55-µm laser diode [23]. In 1989 led by the progression of Bragg gratings formation in optical fibers [24], a photoinduced FBG was coupled to a laser diode and demonstrated as a tuning element of the operating wavelength [25]. In 1991, a unique configuration of a single-mode hybrid laser deploying a photoinduced FBG was presented by Bird *et al* [26]. The attributes of the narrow reflectivity bandwidth of the FBG and AR coating were integrated unprecedentedly in one device. An AR coated 1.55-µm laser diode was used as the gain chip, which was efficiently coupled via an integrated fiber lens to a low loss fiber forming the external cavity as displayed in Figure 1.10. The FBG closed the cavity as a reflecting end with a 3-dB bandwidth of 0.1 nm and, at the same time, its partial reflectivity, 40%, enabled the output to be taken through its end.

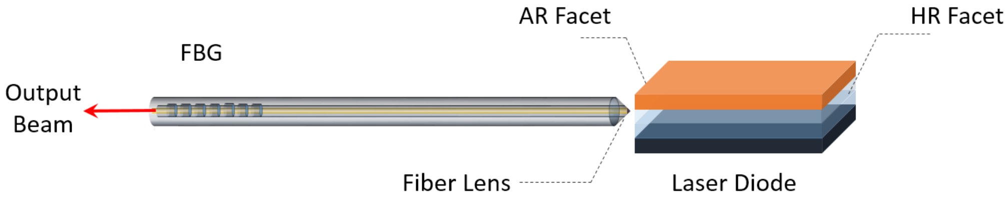

Figure 1.10: Schematic view of a hybrid laser, constructed from an SOA whose cavity is extended by a fiber that is terminated by an FBG. The FBG end functions as an output coupler while the fiber cavity is coupled via its lensed end to the AR coated facet of the SOA.

This scheme allowed for a simple design with a very practical structure that was adopted later even for other applications [27,28].The 6-cm long cavity of the packaged device gave 50-kHz linewidth laser. The device was proposed as a viable alternative to DFB lasers in wavelength division multiplexing (WDM) systems because of two reasons. Firstly, the deployment of this device can enhance the degree of control of the operating wavelength through the manufacturing process without major post fabrication selection. Secondly, the linewidth requirement can be readily customized by controlling the fiber cavity length.

Morton *et al* used the same configuration to build a single-mode high power laser in 1994 [29]. However, they used an AR coated hyperbolic lens providing a high coupling efficiency [30] while the cavity length was 4.1 cm. The rear facet of the SOA was HR coated (~90%) and the lasing threshold was as low as that measured for the uncoated laser diode, which gave rise to a high output power of 27.5 mW. Moreover, a chirped FBG was deployed for the first time in such a configuration with a fairly low reflectivity of 33%. Twofold improvement of the laser performance was resulted.

- Firstly, the operating EC mode of a hybrid laser is associated with the highest differential gain [21]. The perturbations in the cavity optical length due to environmental and external noise change the phase of the reflected “feedback” light and hence, shift the operating mode to pick up a higher gain. Eventually, the operating wavelength changes as the mode pulls randomly within the grating bandwidth following the external noise. This random shift of the operating wavelength can be countered and attenuated by a chirped FBG imposing slight variations in the phase of the external feedback [31]. Thus using the chirped FBG with the decreased grating period facing the output coupler as shown in Figure 1.11, the wavelength of the operating mode red shifted when the cavity length increased while it blue-shifted when the cavity length decreased. As a result, the intensity was stabilized and hence, the short-term frequency stability was improved.

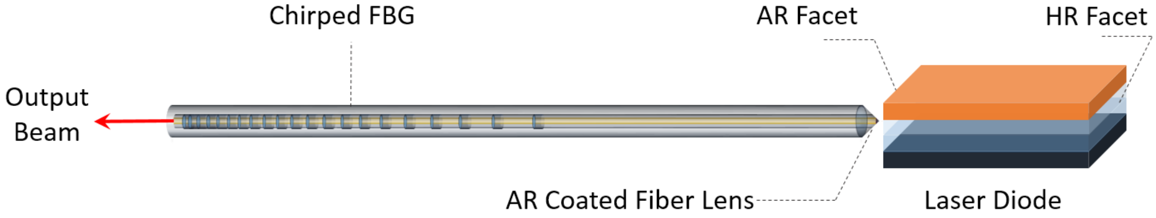

Figure 1.11: Schematic depiction of a hybrid laser constructed from an SOA coupled to a fiber cavity, where the fiber-chip coupling is achieved by an AR coated fiber micro-lens. The cavity is terminated by a chirped FBG at the output end while the HR coated facet of the SOA forms the other.

- Secondly, single-mode operation was claimed to be guaranteed regardless of any changes affecting the cavity length. Although occasional mode hops occurred to reset the operating mode to a maximum feedback coinciding with the peak reflectivity [29,31], they were not associated with spurious noise or side modes leading to mode beating.

Since the cavity length of the laser diode is very short relative to the fiber external cavity, the dominant mode operates within the grating bandwidth as already shown in Figure 1.6. Thus, the SMSR must be measured at a resolution of the mode spacing of the entire cavity, which is much smaller than that of the laser diode cavity (see Eqs. (1.7&1.8)).

However, the spectral purity of the above mentioned devices, provided by the SMSR measurements, did not represent the actual and precise SMSR that can be reliable for industry. This is because the SMSR was measured with a resolution of the mode spacing of the diode cavity as can be seen, for example, in Figure 1.12 [29,31]. It shows a SMSR of 56 dB, which could be easily less than 10 dB if the resolution of the optical analyzer was able to realize the resolution of the mode spacing of the entire cavity which is ~20 pm in this case. Consequently, the EC modes were not resolved and the actual long-term stability could not be reported.

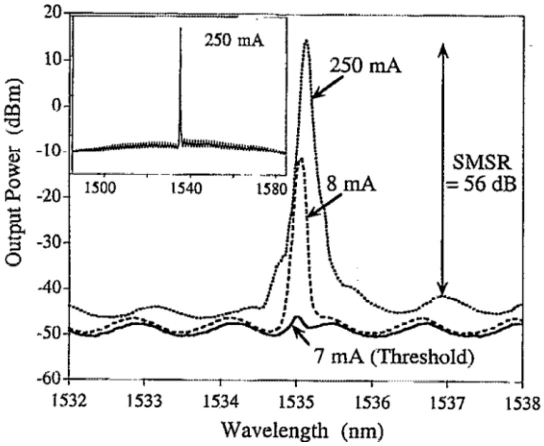

Figure 1.12 Optical spectra of the hybrid laser with a chirped FBG operating at various bias currents. The SMSR measurement is not actual as the spectral resolution did not resolve the EC modes that are separated by a mode spacing of 0.02 nm. Reproduced from Ref. [31].

In fact, a low SMSR and poor long-term frequency stability can be attributed to the lack of an intracavity high-resolution filter. The FBGs, deployed in those devices, functioned as a reflector terminating the cavity and was supposed to act as a wavelength selector (filter), regardless the wide reflectivity bandwidth relative to the fine mode spacing of the long cavity.

1.6.2 Intracavity filter

The development in practical research and application of rare-earth-doped fiber in the field of fiber amplifies [32] had delivered ED fibers as the basic building blocks for fiber amplifiers, used in broadband optical networks. In 1992, Frisken brought up the possibility of using the self-induced (dynamic) grating in a piece of ED fiber as an optical filter with a narrow bandwidth (16 MHz) [33]. Based on the bandwidth of such a grating, stable single-frequency fiber loop laser was demonstrated by Cheng *et al* later in 1994 [34]. The first deployment of the dynamic grating as an intracavity filter to build a single-frequency hybrid laser was demonstrated by Loh *et al* in 1995 [18]. A 3-m long ED fiber end was tapered, lensed and coupled to the AR coated facet of a 500-μ-long laser diode. The absorption of this fiber was measured to be 1 dB/m at 1535 nm. The other end of the ED fiber was spliced to a 25-cm-long passive fiber that was terminated by an FBG forming the external reflector as shown in Figure 1.13. The laser cavity was 3.25 m in length and the FBG was 80% reflecting with a bandwidth of 0.2 nm (25.5 GHz), centered at a wavelength of

1535 nm. The mode spacing of the external cavity was ~31 MHz separating ~820 external modes that fall within the FBG reflectivity bandwidth. Out of theses external modes, one mode was chosen to dominate the others by the high feedback of a fine resolution band-stop filter. This filter has a bandwidth of ~30 MHz, which is the low reflectivity bandwidth of the 3-m-long dynamic grating distributed along the ED fiber. Eventually, a single EC mode was picked to lase with a kHz linewidth. Unfortunately, the linewidth obtained was limited by the resolution of the measurements. This paper [18], in particular, is also of great importance as it mentioned the possibility of fine-tuning the operating frequency within a single mode spacing (without a mode-hop) with the bias current. However, this was not really demonstrated as the stability was poor due to the smooth drift of the operating frequency back and forth within one or two mode spacings.

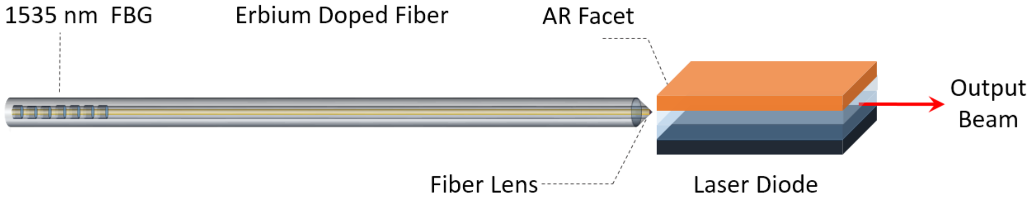

Figure 1.13: Schematic structure of a 325-cm-long cavity of a hybrid laser, built by coupling the fiber cavity to an SOA via a fiber lens. A 300-cm-long ED fiber is inserted within the cavity to investigate the dynamic grating effect on the laser operation.

An attempt to produce a robust pigtailed packaged hybrid laser was demonstrated in 2003 by Timofeev *et al* [35]. A 63-cm-long ytterbium doped fiber was spliced into a 27-cm-long passive fiber, whose one end is terminated by an FBG centered at 976 nm and the other is coupled to a laser diode packaged in a butterfly case. However, a poor SMSR of 10 dB was associated with a frequency drift of ~940 MHz among the external modes, separated by a mode spacing of ~113 MHz of the 90-cm-long external cavity.

In 2006, Liu *et al* demonstrated a better SMSR of ~16 dB, produced by a 1490-nm hybrid laser. The FBG has a peak reflectivity of 78% and a piece of ED fiber with an absorption of 16 dB/m was spliced into the external fiber cavity. That SMSR was inferred from an electrical spectrum, measured at a sufficient resolution to resolve the external modes that are spaced by ~154 MHz [36]. Yet, a SMSR of 16 dB is low and can be attributed to the partial occupation of a 28-cm-long ED fiber in the 67-cm-long fiber cavity. The mode spacing of the cavity is therefore finer than the bandwidth of the dynamic grating. Also, it was reported that the single-frequency operation deteriorated depending on the SOA drive current or, equivalently, on the intracavity power in contrast to what was reported by Loh *et al* [18]. This could be attributed to the different filling ratio of the ED fiber relative to the entire cavity as well as to the different absorption of the ED fibers, used to construct the external cavity. However, the bias current effect on the spectral purity (or the SMSR) was ignored when the tunability of that device was studied afterwards in 2007 [37]. Regardless the actual SMSR that was not measured while tuning the wavelength, the operating mode was found to tune across ~60 modes at a resolution of ~51 MHz/mA when the bias current tuned within a range of 160 mA (30-190mA). Also, a frequency-temperature coefficient was measured to be ~3 GHz/ºC when the temperature of the laser diode tuned at a resolution of 0.1 ºC, while the temperature of the external FBG was not affected .The operating wavelength was therefore tuned within the bandwidth of the FBG to scan 100 pm before it jumped back every 4 ºC [37].

1.7 Dissertation outline

Having the motivation and objectives introduced along with an overview on hybrid lasers, the aim of the presented work can be better realized by organizing the project's results and the relevant literature as follows:

Chapter 2. Concepts and components

The FBGs concept is outlined. An FBG inscription technique is demonstrated using a scanning phase mask Talbot interferometer. A theoretical model calculating the quantitative characteristics of FBGs is presented based on solving the coupled-mode equations. The reflectivity and transmissivity of various FBGs are simulated in order to demonstrate the effect of the grating parameters on an FBG function. As the external FBG in our hybrid laser operates in reflection, the relationship among the grating bandwidth, maximum reflectivity and length is given in detail. The ideal fiber micro-lens coupling the SOA to the fiber cavity is illustrated by a theoretical model satisfying the conditions of phase and amplitude distributions. The lens is designed to ensure the wavefront conversion of the diode beam waist onto parallel wavefront of the fiber beam waist, where the emitted beam waist matches exactly the fiber spot size. Finally, an ideal optical coupling efficiency is shown by depositing an AR coating film on the fiber lens.

Chapter 3. Hybrid laser device

The main components of the hybrid laser device including the polarization maintaining (PM) ED fiber cavity, fiber micro-lens and SOA are clarified. The device assembly is presented. The purpose of using a PM fiber to construct the cavity is revealed in terms of the birefringent difference to eliminate polarization mode dispersion. Therefore, the energy of the standing wave intensity will be confined within the slow axis plane. This will be shown later to have a key role in stabilizing the operating frequency. The use of a cavity that is fully made up of ED fiber is reported. Thus, the formation of an intracavity high-resolution band-stop filter is shown as a unique solution to achieve single frequency operation. The ideal fiber lens that can offer a high coupling efficiency and match the SOA, used in the device, is simulated and the fabrication parameters are presented. The fiber-chip coupling is performed while the optimal thermal stability scheme including both the fiber cavity and SOA is achieved. Also, the materials and structure of the ridge waveguide SOA are described along with the physical and operational specifications that are listed.

Chapter 4. Single frequency operation

The concept of selecting a single mode to lase is illustrated based on the reflectivity of the dynamic grating that is simulated using the T-matrix method to solve its coupled-mode equations. Out of several tens of allowed modes that fall within the external FBG bandwidth, the dynamic grating reflectivity bandwidth is shown to allow only one mode to oscillate in the cavity. Single frequency operation of this device is experimentally proven through optical spectra showing a single and sharp spike. Also, electrical spectra show very low amplitude and flat pattern that has no self-beating notes, which confirms the optical measurements. Moreover using heterodyne-beating technique, side mode suppression is confirmed and single frequency operating is verified.

Chapter 5. Purity of the operating mode

The spectral purity of the demonstrated device in terms of the linewidth is accurately measured using subcavity formation to avoid environmental and external noise. The subcavity that is coupled to the main cavity of the hybrid laser is theoretically explained and simulated. A perfect agreement with the measurements is shown through optical and electrical spectra, which illustrate the spectral positions of the subcavity modes, coupled to the allowed modes of the main cavity. The electrical measurement are taken at a high bandwidth resolution to resolve the actual linewidth. The SMSR along with the power at wavelength peak is determined using the optical spectra. The high SMSR ensures that most of the output power is carried by the operating mode at the expense of a very low baseline noise floor.

Chapter 6. Tunability of the operating wavelength

For the first time, the precision tunability at a high resolution of a couple of MHz is demonstrated by tuning the bias current. This tunability is found to scan a single mode spacing for a span of the whole drive current range. In other words, we get a fully continuous linear tunability with the current within a single mode spacing. Moreover while the SMSR is maintained at its high value, mode-hop free tuning at a resolution of a couple hundreds of MHz is unprecedentedly reported over a spectral range of several mode spacing. This tunability is actually performed by tuning the temperature of the fiber cavity so that the Bragg wavelength of the external FBG is shifted. The significance of this achievement can be realized by the possibility of transferring the linear precision tunability, driven by a high resolution current, to any frequency that can be roughly reached by the coarse tunability range.

Chapter 7. Stability of the operating wavelength

The ability to stabilize the operating wavelength within a couple tens of Hz is shown for the first time under free running conditions. Also for unpackaged device exposed to external environmental noise, a long-term frequency stability within one-eighth of the mode spacing is reported while the possibility of locking a device with such a configuration to a single mode, or within two mode spacings, has not been reported to date. This achievement is attributed to the frequency stabilizing mechanism that was established by the combination of the filtering effect, imposed by the dynamic grating, with the resistance of the recirculating process to low-frequency disturbances penetrating the dynamic grating filter. The recirculating process is inferred based on the operational characteristics of the hybrid laser. The possibility of this process can be established through non-radiative transitions among upper energy levels of erbium ions. Using our new device set-up scheme, the associated heat generation noise affecting the fiber cavity length has been removed utilizing a high resolution PID loop of a thermoelectric cooler (TEC) that is experimentally optimized.

Chapter 8. Conclusions and potential applications

The novel achievements towards building the unique hybrid laser device, presented in this work, are pointed out in terms of single frequency, spectral purity, stability and tunability. A summary of the work is presented and future work direction is provided. Potential applications that can be better served by our device are highlighted along with the possible deployment benefits.

CHAPTER 2 CONCEPTS AND COMPONENTS

Hybrid lasers design is based on combining different technologies. In this chapter, FBGs fabrication technique using a scanning phase mask Talbot interferometer will be shown. The Bragg condition of an FBG will be derived from the familiar grating equation. A theoretical model to determine the spectral dependence of an FBG reflectivity and transmissivity will be developed based on the coupled-mode equations and executed using the transfer-matrix method. The ideal micro-lens to achieve the best coupling efficiency for single mode operation will be demonstrated.

2.1 Bragg condition

The diffraction of a light wave incident on a grating diffraction, whose grating period is Λ, can be described by the familiar grating equation [38]

$$n \sin\theta_2 = n \sin\theta_1 + m\frac{\lambda}{\Lambda}, \tag{2.1}$$

where θ_1 is the incident angle, θ_2 is the diffraction angle, n is the effective refractive index and m is an integer determining the diffraction order as shown in Figure 2.1.

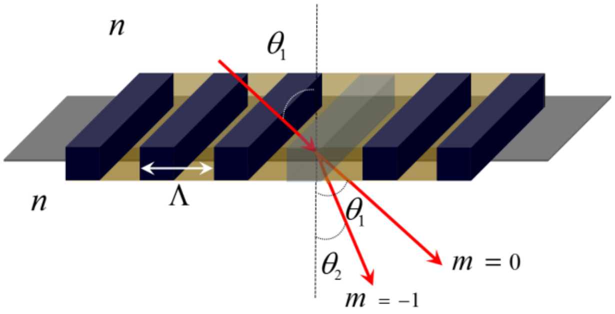

Figure 2.1: Schematic of a diffraction grating showing the diffraction of an incident beam at an angle θ_1 and the 1st order diffraction at an angle θ_2.

In the case of a uniform fiber Bragg grating, the constructive interference occurs when an incident light wave is diffracted in the opposite direction, i.e., $\theta_2 = \pi + \theta_1$, and the 1st order diffraction, $m = -1$, dominates the reflection of a uniform FBG as shown in Figure 2.2.

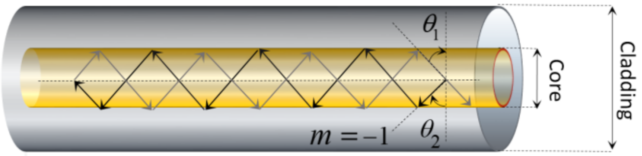

Figure 2.2: Ray diagram representation of the core mode reflection by a uniform FBG.

In this case, Eq. (2.1) becomes

$$2n_{co} \sin\theta_2 = \frac{\lambda_B}{\Lambda}, \tag{2.2}$$

where n_{co} is the refractive index of the fiber core and λ_B is the Bragg wavelength. Substituting the effective refractive index, $n_{eff} = n_{co} \sin\theta_2$, in Eq. (2.2), the Bragg condition can be written as

$$\lambda_B = 2\, n_{eff}\, \Lambda. \tag{2.3}$$

This equation, representing the 1st order Bragg grating condition, is resulted from both energy and momentum conservations. Energy conservation requires that the frequency of the incident light wave to be the same as the frequency of the reflected light wave, which is associated with the Bragg wavelength, λ_B . In the case of total reflection at λ_B , momentum conservation requires that

$$K_{Inc} + K_G = K_{Diff}\,. \tag{2.4}$$

The diffracted wave-vector, K_{Diff} , equals the sum of the incident wave-vector, K_{Inc} , and grating wave-vector, K_G , which are depicted in Figure 2.3.

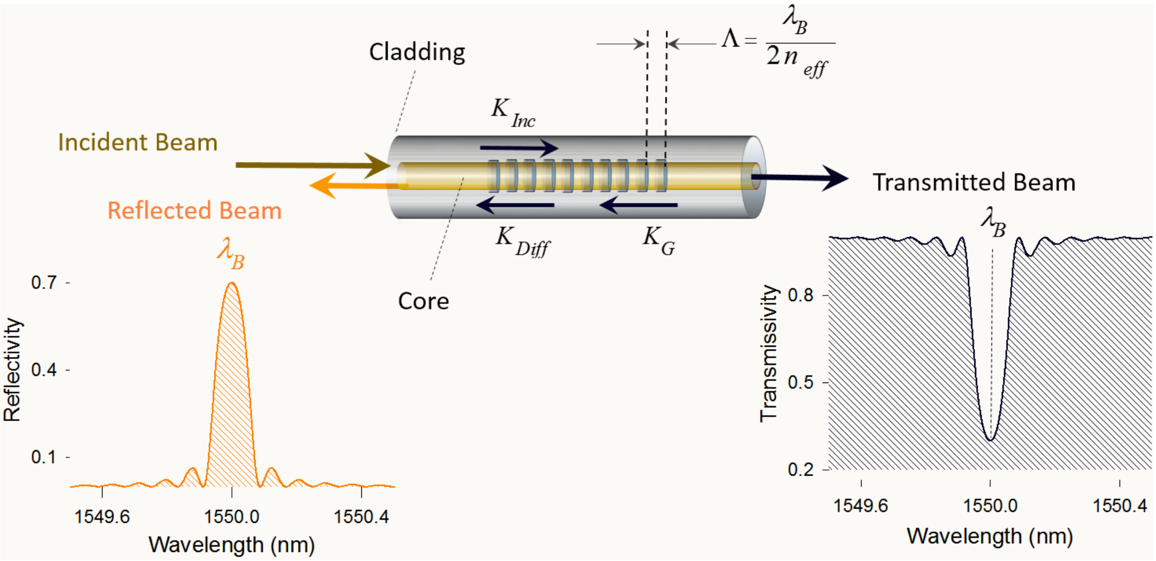

Figure 2.3: Operation of a uniform FBG reflecting the guided core mode when the Bragg condition is satisfied, i.e., the incident wave-vector, K_{Inc}, is reversed in response to the grating wave-vector, K_G, giving the diffracted wave-vector K_{Diff}. The simulated spectra, centered at 1.55 µm, represent the reflectivity and transmissivity of a 1-cm-long FBG as a function of the wavelength.

The grating and diffracted wave-vectors have the same direction that is perpendicular to the grating plane and, also, the incident wave-vector is equal in magnitude and opposite in direction to the diffracted wave-vector. The momentum energy conservation, represented in Eq. (2.4), can be then expressed using the related wavenumbers as

$$-\frac{2\pi}{\lambda_B} n_{eff} + \frac{2\pi}{\Lambda} = \frac{2\pi}{\lambda_B} n_{eff} \Rightarrow \lambda_B = 2n_{eff}\Lambda \tag{2.5}$$

2.2 FBG fabrication

A uniform short-period FBG can be produced by exposing a photosensitive fiber to a spatial distributed pattern of ultraviolet intensity. An FBG can be written in the fiber cavity of a hybrid laser by using a scanning phase mask Talbot interferometer [39]. This interferometer is based on the holographic grating inscription scheme, in which a single input ultraviolet (UV) beam is divided by a beam splitter into two beams that are then redirected by two mirrors to interfere at the fiber as shown in Figure 2.4, where a phase mask is used as a beam splitter.

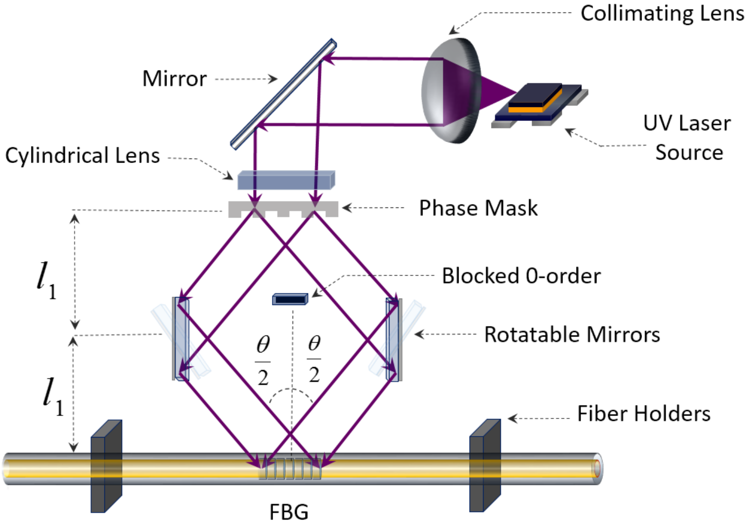

Figure 2.4: Diagram of a scanning phase mask Talbot interferometer used for FBGs inscription. The Bragg wavelength of the FBG can be modified independently from the wavelength of the UV writing beam by rotating the mirrors in order to adjust the mutual angle θ.

The periodic grooves of the phase mask are structured on a UV-transmitting silica plate allowing its operation in transmission. At perpendicular incidence, the UV beam is diffracted and hence, is split into $m = 0, \pm 1$ orders as schematically represented in Figure 2.5.

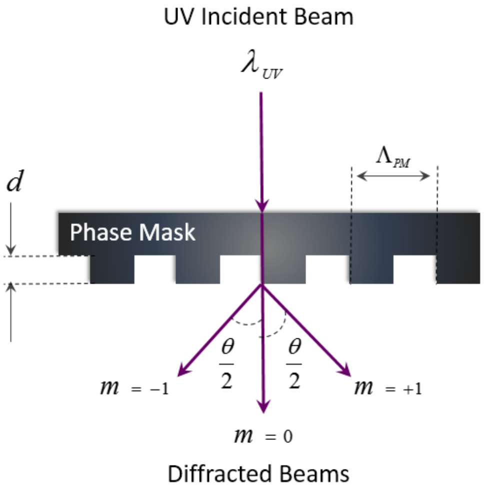

Figure 2.5: Operation of a phase mask in transmission splitting the intense UV writing beam.

When the period grating of the phase mask, Λ_{PM} , relative to the incident wave, λ_{UV} , varies within a range of $\frac{\lambda_{UV}}{2} < \Lambda_{PM} < \lambda_{UV}$, the UV radiation is only split into the 0th and 1st orders. Thus using the grating diffraction Eq. (2.1), the principal of operation, based on the diffraction, can be expressed by substituting $\theta_1 = 0^o$ and $\theta_2 = \frac{\theta}{2}$ for the 1st order as [39]

$$\Lambda_{PM} = \frac{\lambda_{UV}}{n_{UV} \sin\frac{\theta}{2}}, \tag{2.6}$$

where n_{UV} is the refractive index of the UV in silica mask plate. Recalling Eq. (2.2) $\Lambda = \frac{\lambda_B}{2n_{co}\sin\theta_2}$ and substituting $\frac{\lambda_{UV}}{n_{UV}} = \frac{\lambda_B}{n_{co}}$, the grating period of the FBG becomes $\Lambda = \frac{\lambda_{UV}}{2n_{UV}\sin\theta_2}$ that can be found to be related to Λ_{PM} as [39]

$$\Lambda_{PM} = 2\,\Lambda \tag{2.7}$$

Substituting Eq. (2.3) in Eq. (2.7) gives

$$\Lambda_{PM} = \frac{\lambda_B}{n_{eff}} \tag{2.8}$$

Comparing Eq. (2.6) and Eq. (2.8), the Bragg wavelength is then may be related to the angle of the 1st order diffraction mode as

$$\lambda_B = \frac{n_{eff}}{n_{UV}} \frac{\lambda_{UV}}{\sin\frac{\theta}{2}}. \tag{2.9}$$

In fact, when the mirrors are precisely aligned and oriented to transfer the diffraction angles from the phase mask plate to the fiber axis, the phase mask predefines the Bragg wavelength of the FBG as illustrated in Eq. (2.8). The reflecting Bragg wavelength of the FBG can be then modified independently from the wavelength of the UV writing beam by rotating the mirrors to adjust the mutual angle, θ, between the two beams recombined at the fiber. Taking the derivative of λ_B given in Eq. (2.9), the Bragg wavelength changes as a function of the half writing angle θ as

$$\Delta\lambda_B = -\left(\lambda_B \cot\frac{\theta}{2}\right)\Delta\frac{\theta}{2}, \tag{2.10}$$

Where $\Delta\lambda_B$ is the variation of the Bragg wavelength with changing diffraction angle by $\Delta\frac{\theta}{2}$.

A procedure of two steps is required in order to adjust the Bragg wavelength of an FBG that can be written in a fiber using such an interferometer. The mirrors must be rotated to a calibrated mutual angle and the fiber must be displaced to receive the best focusing interference pattern with keeping its parallel orientation with respect to the phase mask as shown in Figure 2.4. Also, care must be taken to maximize the mutual coherence of the UV writing beams, recombined at the fiber core, by ensuring that the identical path lengths between the phase mask/mirrors and mirrors/fiber [39,40] through balancing l_1 as shown in Figure 2.4.

The phase mask zero order must be physically blocked while it can be minimized by controlling the grove depth d of the grating, etched in the mask plate and shown in Figure 2.5. The groove depth of the relief grating must be $d = \frac{\lambda_{UV}}{2(n_{UV}-1)}$ at least [39]. The phase mask should also be AR coated to not disturb the quality of the interference fringes [41].

A 20-cm focal length cylindrical focusing lens, shown in Figure 2.4, may be placed just before the phase mask. It focuses and helps to align the UV writing beams along the grating at the fiber, allowing the power density to increase without altering the grating length. However, the grating length can be increased independently of the focused beams intersection by placing either the fiber holder or the phase mask/mirrors unit on a one-dimensional translation stage. This arrangement allows to scan precisely a longer piece of the fiber. The fiber should be photosensitive and/or hydrogen loaded to create a permanent refractive index modulation.

2.3 Theoretical model

The periodic perturbation, or modulation, of the effective refractive index constituting a uniform grating in the fiber may be described as [42]

$$\Delta n_{eff}(z) = \overline{\Delta n_{eff}}(z)\left[1+\upsilon\cos\left(\frac{2\pi}{\Lambda}z\right)\right], \tag{2.11}$$

where υ is the fringes visibility and $\overline{\Delta n_{eff}}$ is the "dc" refractive index change averaged spatially over the uniform grating period Λ while there is no grating chirp or arbitrary phase change. $\Delta n = \upsilon\overline{\Delta n_{eff}}$ is the amplitude of the "ac" refractive index modulation.

In a uniform short-period FBG, coupling occurs between modes that travel in opposite directions. However, mode coupling is not possible unless the modes are phase matched, $\beta_2 = \beta_1$. Substituting the mode propagation constant, defined as $\beta = \frac{2\pi}{\lambda} n_{eff}$, in Eq. (2.4&2.5), we get

$$-\beta_1 + \frac{2\pi}{\Lambda} = \beta_2, \tag{2.12}$$

where β_1 and β_2 represent the incident and reflected modes, respectively. Considering these modes traveling in a single-mode fiber, the couple-mode theory is used as a vital tool to describe the FBG. The quantitative information of the transfer characteristics and spectral dependence of the FBG can be obtained from the coupled-mode equations [39]. Applying the synchronous approximation [42], only the synchronous terms that have a major contribution to the amplitude modulation are kept. Eventually, the resulting coupled-mode equations are given as

$$\begin{aligned} \frac{dR}{dz} &= i\ \sigma R(z) + i\ \kappa_{ac} S(z) \\ \frac{dS}{dz} &= -i\ \sigma S(z) - i\ \kappa_{ac}^{*} R(z), \end{aligned} \tag{2.13}$$

where the amplitudes of the forward-going ($R(z)$ reference) and backward ($S(z)$ signal) identical modes propagating in the +z and -z directions, respectively, are

$$R(z) = A(z)\, e^{i(\Delta\beta z - \phi)/2}$$

$$S(z) = B(z)\, e^{-i(\Delta\beta z + \phi)/2} \tag{2.14}$$

$$\sigma = \kappa_{dc} + \frac{\Delta\beta}{2} - \frac{1}{2}\frac{d\phi}{dz}, \tag{2.15}$$

Where κ_{ac} and κ_{dc} are the "ac" and "dc" coupling coefficients, respectively, that are related to each other with $\kappa_{ac} = \frac{\upsilon}{2}\kappa_{dc}$ and $d\phi/dz$ is the phase variation.

For a single-mode reflection uniform FBG and fringe visibility of unity, the variation in the phase $d\phi/dz = 0$ (no chirp in the grating), κ_{ac}, κ_{dc} are constants and κ_{ac} is given as [42]

$$\kappa_{ac} = \frac{\pi}{\lambda}\Delta n \tag{2.16}$$

Under those conditions and at $z = 0$, the analytical solution of Eq. 2.13 gives the amplitude reflection coefficient

$$\rho = \frac{S(z=0)}{R(z=0)} = \frac{-\kappa_{ac}\sinh(\alpha L)}{\sigma\sinh(\alpha L) - i\,\alpha\cosh(\alpha L)}, \tag{2.17}$$

where L is the grating length and

$$\alpha = \sqrt{\left|\kappa_{ac}\right|^2 - \sigma^2}. \tag{2.18}$$

The bandwidth of the uniform grating, $\Delta\lambda_G$, is usually determined by the spectral spacing between the first minima on each side of the reflection peak. From eq. (2.17), those minima can be determined when equating aL to π, which can be combined with Eq. (2.18) to give

$$\sqrt{\kappa_{ac}{}^2 - \sigma^2}\, L = i\pi \Rightarrow \sigma = \frac{1}{L}\sqrt{\kappa_{ac}{}^2 L^2 + \pi^2}. \tag{2.19}$$

Substituting $d\phi/dz = 0$ and $\kappa_{dc} = 0$ in Eq. (2.15), the phase detuning becomes $\sigma = \frac{\Delta\beta}{2}$, which can be used in Eq. (2.19) to give

$$\Delta\beta L = 2\sqrt{\kappa_{ac}{}^2 L^2 + \pi^2}. \tag{2.20}$$

Recalling Eq. (2.12) and substituting $\beta_1 = \beta_2 = \beta_B$ since the FBG is uniform we get

$$\begin{aligned} \beta_B &= \frac{\pi}{\Lambda}, \\ \Delta\beta &= 2\beta_1 - 2\beta_B. \end{aligned} \tag{2.21}$$

The phase mismatch is therefore can be rewritten as

$$\Delta\beta = 2\beta_1 - 2\beta_B = 4n_{eff}\,\pi\frac{\lambda_B - \lambda}{\lambda_B\lambda}. \tag{2.22}$$

when $\lambda \approx \lambda_B$, Eq. (2.22) can be written as

$$\Delta\beta = 4n_{eff}\,\pi\frac{\Delta\lambda}{\lambda^2}\ . \tag{2.23}$$

Combining Eq. (2.20) and Eq. (2.23), the grating bandwidth between the first zeros is

$$\Delta\lambda_G = 2\Delta\lambda = \frac{\lambda^2}{\pi n_{eff} L}\sqrt{\kappa_{ac}{}^2 L^2 + \pi^2}. \tag{2.24}$$

From Eq. (2.17), the power reflectivity of the uniform Bragg grating can be obtained

$$|\rho|^2 = \frac{\sinh^2(\alpha L)}{\cosh^2(\alpha L) - \dfrac{\sigma^2}{|\kappa_{ac}|^2}}. \tag{2.25}$$

At the Bragg wavelength, the phase matching is satisfied $\beta_1 = \beta_2$. In other words, the detuning expressing the phase mismatch is $\Delta\beta = 0$ and $\sigma = 0$ when substituting $\kappa_{dc} = 0$. Therefore, $\alpha = \kappa_{ac}$ and the peak reflectivity at Bragg wavelength becomes [39]

$$|\rho|^2 = \frac{\sinh^2(\kappa_{ac}L)}{\cosh^2(\kappa_{ac}L)} = \tanh^2(\kappa_{ac}L). \tag{2.26}$$

Eqs. (2.13) can be solved and the power reflectivity of the grating, given by Eq. (2.25), can be simulated as a function of the wavelength by using the transfer-matrix (T-matrix) method, in which the grating length, L, is divided into short sections δl .The parameters of the coupling coefficients and phase are constant for each section, which may be independent from each other and dependent on the spatial parameter. Each section, such as δl_1, can be considered as a four-port device, in which the input fields are $R(z = -\frac{\delta l_1}{2})$ and $R(z = \frac{\delta l_1}{2})$ while the output fields are $S(z = \frac{\delta l_1}{2})$ and $S(z = -\frac{\delta l_1}{2})$. Using the T-matrix method, shown in Eq. (2.27), the coupled-mode equations are solved to determine the amplitude reflection, amplitude transmission and phase for each section.

$$\begin{bmatrix} R(z = -\frac{\delta l_1}{2}) \\ S(z = -\frac{\delta l_1}{2}) \end{bmatrix} = \begin{bmatrix} T_{11}^1 & T_{12}^1 \\ T_{21}^1 & T_{22}^1 \end{bmatrix} \begin{bmatrix} R(z = \frac{\delta l_1}{2}) \\ S(z = \frac{\delta l_1}{2}) \end{bmatrix}, \tag{2.27}$$

The calculated quantities are then considered the input parameters for the two adjacent four-port sections. Applying the boundary conditions to Eq. (2.27); the reference wave incident from $z = -\infty$ in the +z direction is normalized to unity while no signal (reflected) wave exists at $z = \frac{l_1}{2}$ or, equivalently, $R(z = -\frac{\delta l_1}{2}) = 1$ and $S(z = \frac{\delta l_1}{2}) = 0$. Thus, Eq. (2.27) becomes

$$\begin{bmatrix} 1 \\ S(z=-\frac{\delta l_1}{2}) \end{bmatrix} = \begin{bmatrix} T^1 \end{bmatrix} \begin{bmatrix} R(z=\frac{\delta l_1}{2}) \\ 0 \end{bmatrix}, \qquad \begin{bmatrix} T^1 \end{bmatrix} = \begin{bmatrix} T_{11}^1 & T_{12}^1 \\ T_{21}^1 & T_{22}^1 \end{bmatrix} \tag{2.28}$$

in which the transmitted amplitude (reference wave) is clearly

$$R(z=\frac{\delta l_1}{2}) = \frac{1}{T_{11}^1} \tag{2.29}$$

and the reflected amplitude (signal wave) is

$$S(z=-\frac{\delta l_1}{2}) = \frac{T_{21}^1}{T_{11}^1}, \tag{2.30}$$

where the T-matrix, representing the grating amplitudes and phase response, is defined as [39]

$$\begin{bmatrix} T_{11}^1 & T_{12}^1 \\ T_{21}^1 & T_{22}^1 \end{bmatrix} = \begin{bmatrix} \cosh(\alpha\delta l_1) - \frac{i\sigma\sinh(\alpha\delta l_1)}{\alpha} & -\frac{i\kappa_{ac}\sinh(\alpha\delta l_1)}{\alpha} \\ \frac{i\kappa_{ac}\sinh(\alpha\delta l_1)}{\alpha} & \cosh(\alpha\delta l_1) + \frac{i\sigma\sinh(\alpha\delta l_1)}{\alpha} \end{bmatrix}. \tag{2.31}$$

Thus, the reflection amplitude is

$$\rho = \frac{S(0)}{R(L)} = \frac{T_{21}^1}{T_{11}^1}. \tag{2.32}$$

Ultimately, the diffraction efficiency and spectral dependence of the entire grating that is divided into N sections, $L = \sum_{j=1}^{N} \delta l_j$, can be written as

$$\begin{bmatrix} R(z=-\frac{L}{2}) \\ S(z=-\frac{L}{2}) \end{bmatrix} = [\mathbf{T}] \begin{bmatrix} R(z=\frac{L}{2}) \\ S(z=\frac{L}{2}) \end{bmatrix}, \tag{2.33}$$

where

$$[\mathbf{T}] = [T^N]...[T^2][T^1] = \prod_{j=1}^{N} [T^j] \tag{2.34}$$

The transmission amplitude, τ, and the reflection amplitude, ρ, of the uniform grating are [39]

$$\tau = (1-\rho) = \frac{R(z=\frac{L}{2})}{R(z=-\frac{L}{2})} = \frac{1}{\mathbf{T}_{11}}. \tag{2.35}$$

$$\rho = \frac{S(z=-\frac{L}{2})}{R(z=-\frac{L}{2})} = \frac{\mathbf{T}_{21}}{\mathbf{T}_{11}}. \tag{2.36}$$

Proceeding with Eq. 2.35 and Eq. 2.36 and taking their square, the power reflectivity and transmissivity can be then obtained and plotted as functions of the wavelength as illustrated in Figure 2.6.

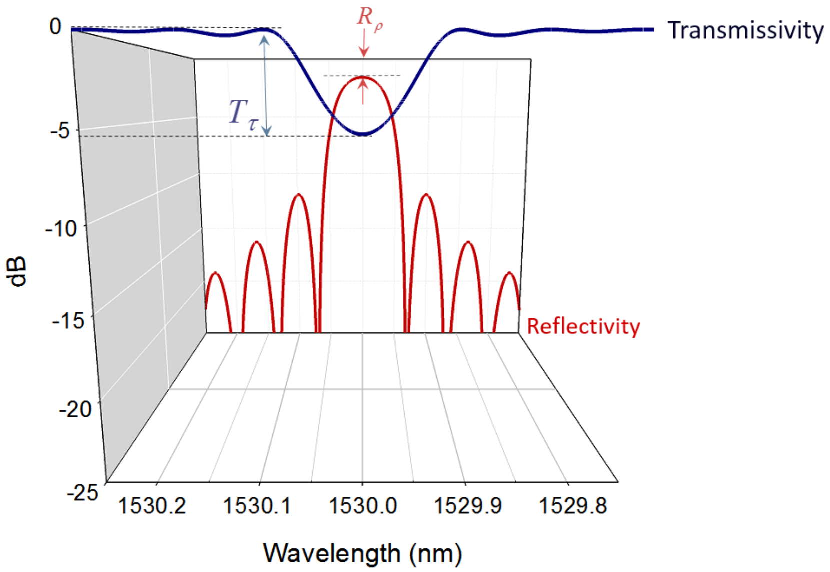

Figure 2.6: Power reflectivity and transmissivity of a 1-cm long uniform FBG simulated as a function of the wavelength using the T-matrix method to solve the coupled-mode equations. The grating reflectivity is centered at the Bragg wavelength $\lambda_B = 1530\text{ nm}$ with a peak reflectivity $R_\rho = 1.549\text{ dB}$ and minimum transmissivity $T_\tau = 5.229\text{ dB}$.

The power peak reflectivity of the FBG, shown in Figure 2.6, can be calculated from the minimum transmissivity $T_\tau = 5.229\text{ dB}$ by using the following equation

$$|\rho|^2 = 1 - 10^{\frac{-T_\tau}{10}}, \tag{2.37}$$

or from the peak reflectivity $R_\rho = 1.549\text{ dB}$ by

$$|\rho|^2 = 10^{\frac{-R_\rho}{10}} \tag{2.38}$$

As a result, the reflectivity of plotted uniform FBG is 70% while the transmissivity is 30% at the Bragg wavelength, 1530 nm.

In order to demonstrate the effect of the grating length on its bandwidth, three FBGs that share the same reflectivity of 70% and have different lengths, $L = 5, 10, 15\text{ mm}$, are simulated and plotted in

Figure 2.7. Increasing grating length, the amplitude of the “ac” refractive index modulation, Δn , reduces and the grating bandwidth, $2\Delta\lambda$, decreases. However, the grating bandwidth is not affected when maintaining the same grating length and varying the peak reflectivity by changing the amplitude of the refractive index modulation, Δn . As can be inferred from Eq. (2.24), the last two statements are valid for short uniform FBGs, which are usually used to build hybrid lasers.

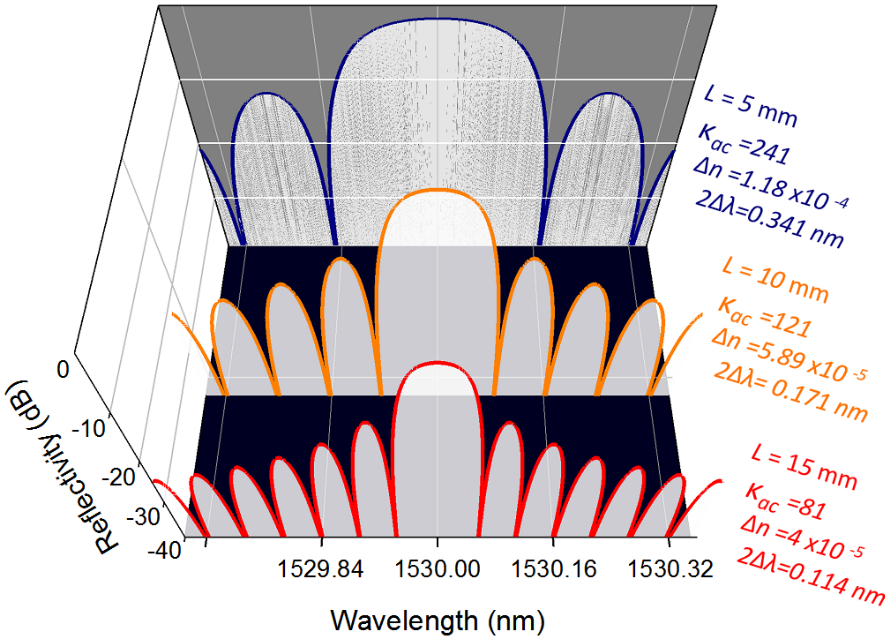

Figure 2.7: Power reflectivity spectra of three uniform FBGs having different lengths and sharing the same peak reflectivity of 70%. The “ac” coupling constant κ_{ac} , amplitude of the refractive index modulation Δn and grating bandwidth $\Delta\lambda_G \equiv 2\Delta\lambda$ are highlighted.

The side lobe suppression ratio in a uniform FBG is ~10 dB. Apodized FBG can have lower side lobs. This may be a vital FBG characteristic to stabilize single frequency operation of a hybrid laser since one mode can easily dominates the others without disturbing mode competition by the side lobes. The suppression of the side lobes in an apodized FBG reflectivity spectrum can be done by applying a gradual increment to the “ac” coupling coefficient, followed by a gradual decrement as can be expressed by the functional dependence on the spatial parameter z over the grating length, given by

$$\kappa_{ac} = \frac{\pi\,\Delta n}{\lambda}\frac{1}{2}\left[1+\cos\left(\frac{\pi(z-L/2)}{L}\right)\right]. \tag{2.39}$$

As a result, the side lobes can be suppressed by ~15 dB as can be seen in Figure 2.8.

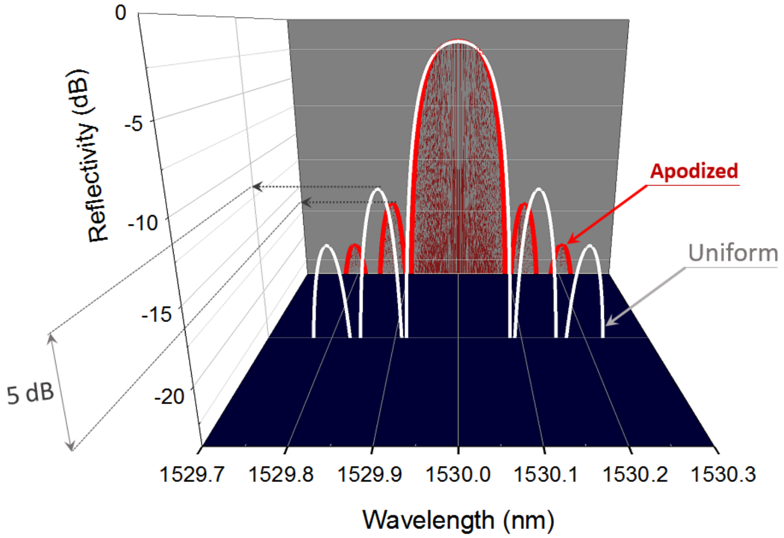

Figure 2.8: Power reflectivity spectra of a uniform FBG compared to that of an apodized FBG, which have the same length and peak reflectivity that are centered at 1530 nm. The side lobes in the apodized FBG are suppressed 5 dB more than that of the uniform FBG.

2.4 Fiber micro-lens

Efficient optical coupling between an AR coated laser diode and fiber is generally achieved by a micro-lens, formed on the fiber tip, for optimal performance of hybrid lasers. The compactness, ease of fabrication [43] and packaging make micro-lenses the best choice for such an application [44]. However, the beam waist, spot size, of a laser diode must be matched to the spot size of single-mode fiber, usually used to extend the cavity of single frequency devices. This requires two conditions on phase and amplitude distribution. Firstly, the phase condition is achieved by imaging the wavefront of the diode beam waist onto the parallel wavefront of the fiber beam waist. Secondly, the divergent elliptical beam waist, emitted from the AR coated facet of the SOA, must be transformed and modified to match the fiber spot size [45]. Hemispherical micro-lenses truncate the guided core mode when reducing the fiber spot size to match that of the diode. Consequently, poor optical coupling is resulted in 50% loss [44]. Four criteria are set for an ideal lens [46]: 1) accept the SOA emission within a large aperture, 2) be free of spherical aberration, 3) have a perfect focal length that can match the modes of the fiber and laser diodes, and 4) be AR coated to prevent Fresnel reflection and avoid formation of undesired subcavities. In view of that, hyperbolic AR coated micro-lenses are the best for fiber-chip coupling [47].

Figure 2.9 demonstrates the fiber-chip coupling scheme of a hybrid laser. The front end of the fiber micro-lens is located at a distance D from the AR coated facet of the gain chip. Considering a spherical wave, emitted by the chip and centered at q , the curvature radius of the incident wavefront on the lens end is therefore z_2. Given that the mode radius is defined as the 1/e amplitude radius of the field, the minimum mode radius of the laser chip is ρ_0 while ρ_1 is the guided core mode radius of the fiber.

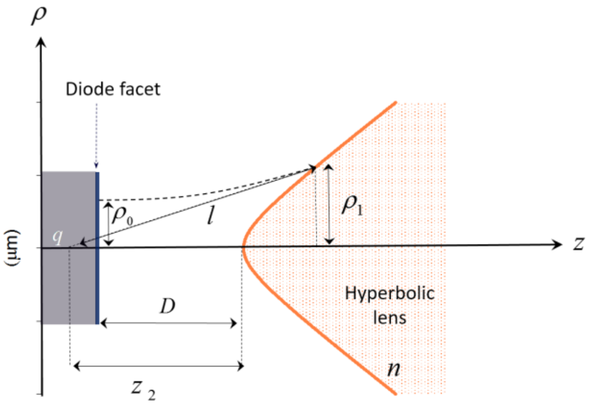

Figure 2.9: Schematic illustration of the fiber-chip coupling. The hyperbolic micro-lens is placed at a distance D from the AR coated facet of the diode and has a focal point at q . The lens is used to couple the spot size of the guided core mode ρ_1 with the beam waist of the diode ρ_0 .

However, the operating mode widens as it propagates from the AR coated facet of the laser chip to the front end of the fiber lens. The expanded mode radius, ρ_2, and the associated, z_2, are given as [48]

$$\rho_2 = \rho_0 \sqrt{1+\left(\frac{\lambda D}{\pi \rho_0^2}\right)^2} \tag{2.40}$$

$$z_2 = \frac{1}{D}\left(\frac{\pi}{\lambda}\rho_0\rho_2\right)^2 \tag{2.41}$$

In fact, the combination of phase matching and having an aberration-free lens can be expressed in the following condition. All the paths to the mutual focal point, q , from any given point on the wavefront are equal. As shown in Figure 2.9, this condition can be satisfied when [46,47]

$$l = f + n z , \tag{2.42}$$

where f is the focal length. By requiring zero phase error, l is also given by

$$l = \sqrt{\rho^2 + (f + z)^2}. \tag{2.43}$$

Substituting Eq. (2.43) in Eq. (2.42), the ideal lens profile is therefore given as [47, 49]

$$\frac{(z + a)^2}{a^2} - \frac{\rho^2}{b^2} = 1, \tag{2.44}$$

where

$$a^2 = \left(\frac{1}{n+1}\right)^2 f^2 \text{ and } b^2 = \left(\frac{n-1}{n+1}\right) f^2. \tag{2.45}$$

In this case, the efficiency of power transfer between the fiber and SOA is referred to as the coupling efficiency η and is given as [47]

$$\eta = \frac{\left|\int_0^\infty \psi_1\psi_2\rho\, d\rho\right|^2}{\int_0^\infty \psi_1^2\rho\, d\rho . \int_0^\infty \psi_2^2\rho\, d\rho}, \tag{2.46}$$

Where $\psi_1 = e^{-\rho^2/\rho_1^2}$ is the amplitude of the guided core mode and $\psi_2 = e^{-\rho^2/\rho_2^2}$ is the amplitude of the expanded mode, whose wavefront curvature radius, centered at q , is z_2.

The coupling efficiency is then can be maximized up to >90% when the distance, D , separating the lens from the AR coated facet of the chip is chosen to ensure the matching between the divergent beam waist and guided core mode radius of the fiber, i.e. $\rho_1 = \rho_2$ and hence, $Z_2 = f$. Substituting those parameters in Eq. (2.45) and Eq. (2.44), the hyperbolic micro-lens can be fabricated using laser micromachining with submicron precision [43], where the spinning stripped fiber tip is moved in a focused CO_2 laser beam ablating the silica fiber.

Depositing an AR coating film on the micro-lens, the coupling efficiency may then approach unity. Normally at the interface boundary between two media of different refractive indices, there will be Fresnel reflection. This reflection occurs, in particular, at the front end of the fiber lens at air/glass interface resulting in power loss. Also, the loss in power can probably be spent on forming subcavity resonators between the lens and the HR rear facet of the SOA. This leads to destabilize the single-mode operation or even to chaotic multi-mode operation of a hybrid laser. This problem can be addressed by coating an AR thin film on the front end of the fiber micro-lens. A single quarter-wavelength thick film may cancel out the reflection owing to the destructive interference, occurring between reflections from the lens and film as shown in Figure 2.10. The coating thickness is

$$D_{thickness} = \frac{\frac{\lambda}{n_{film}}}{4}, \tag{2.47}$$

where λ is the operating wavelength and n_{film} is the refractive index of the film material, which is defined as $n_{film} = \sqrt{n_{air}\, n_{core}} = \sqrt{n_{core}}$ to completely cancel the reflected beam [50]. This ensures that the amplitude of the reflection waves are comparable as the reflectances at the film and micro-lens are almost equal, where the reflectance between the air and film, for example, is $R = \left(\frac{n_{air} - n_{film}}{n_{air} + n_{film}} \right)^2$.

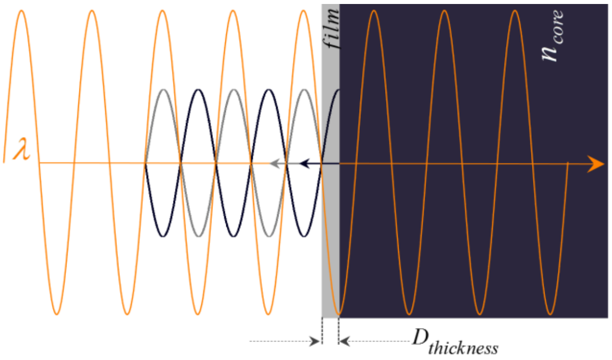

Figure 2.10: Schematic representation of the destructive interference achieved by coating an AR quarter-wavelength thick film.

2.5 Conclusion

The concept of FBGs as a periodic perturbation of the effective refractive index with the length has been presented. A fabrication technique based on using a scanning phase mask Talbot interferometer has been illustrated. A theoretical model based on solving the coupled-mode equations to calculate the reflectivity and transmissivity of an FBG has been explained and executed. In order to understand the effect of the grating parameters on an FBG function, various FBGs have been simulated. Since the external FBG, used as a key component in our hybrid laser, operates in reflection, the relationship among the grating bandwidth, maximum reflectivity and grating length has been discussed. The ideal geometry of the fiber micro-lens that ensures a high optical coupling efficiency between the SOA and fiber cavity has been derived.

CHAPTER 3 HYBRID LASER DEVICE

3.1 Introduction

A hybrid laser operating with high spectral purity and exhibiting mode-hop free tunability due to its excellent stability is demonstrated. The advantage of constructing the external cavity of PM fiber is illustrated. In addition, the PM fiber cavity is doped by erbium ions and hence, the concept of integrating a high resolution intracavity filter operating within the bandwidth of the external FBG grating is explained. The fiber lens that matches the SOA beam is simulated to optimize the optical coupling efficiency and the corresponding fabrication parameters are given. The characteristics of the SOA generating stable single frequency operation are outlined. The PM-ED fiber cavity is temperature stabilized by a high precision PID loop of a thermoelectric cooler (TEC), which is experimentally optimized to cancel out heat generation inside the fiber cavity. In this way, thermal noise affecting the cavity length and operating wavelength is removed since the SOA is also thermally stabilized. In addition, the ability to tune the operating mode thermally at a high resolution through the Bragg wavelength is therefore realized. The device assembly is carefully performed and demonstrated for final packaging steps.

3.2 Device set-up

The hybrid laser is constructed from a 34-cm-long fiber cavity, coupled to a single angled-facet SOA (SAF 1126 from Covega) via a fiber micro-lens as schematically illustrated in Figure 3.1(a). The fiber cavity is made of a piece PM-ED fiber, PANDA fiber from CorActive, ER-25-05-PM-03. The birefringence of this fiber is 1.14×10^{-4}. A centimeter away from the FBG and outside the cavity, the PM-ED fiber is spliced to a 52-cm-long piece of PM fiber, terminated by an FC/APC connector. The fiber cavity is inspected by a Luna (OBR 4600) optical backscatter reflectometer. The various sections of the cavity can be discerned easily from the spatially resolved back-scattered signal as can be seen in Figure 3.1(b).

(a)

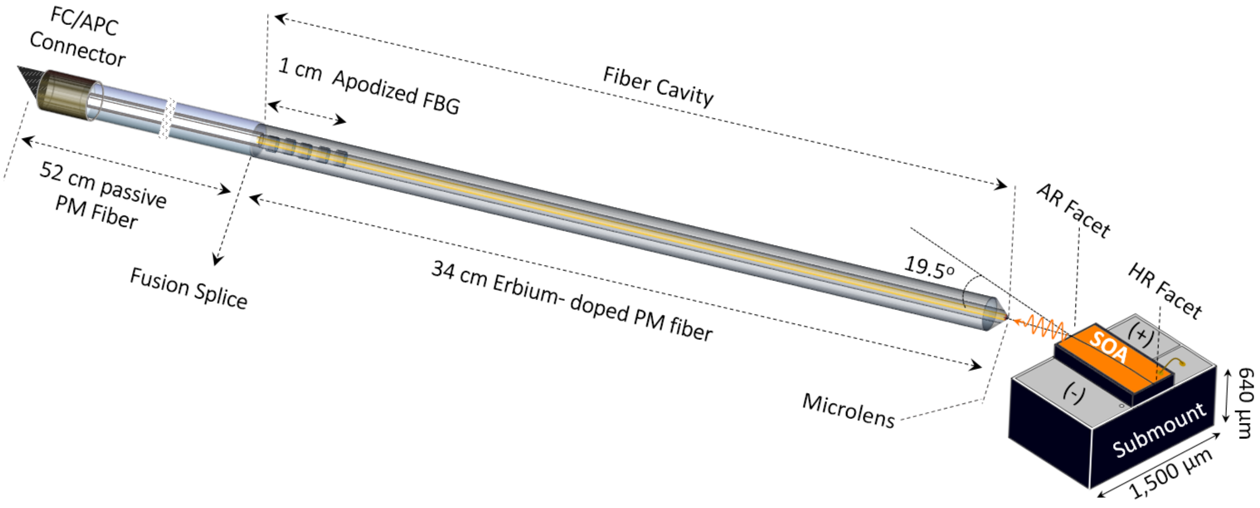

(b)

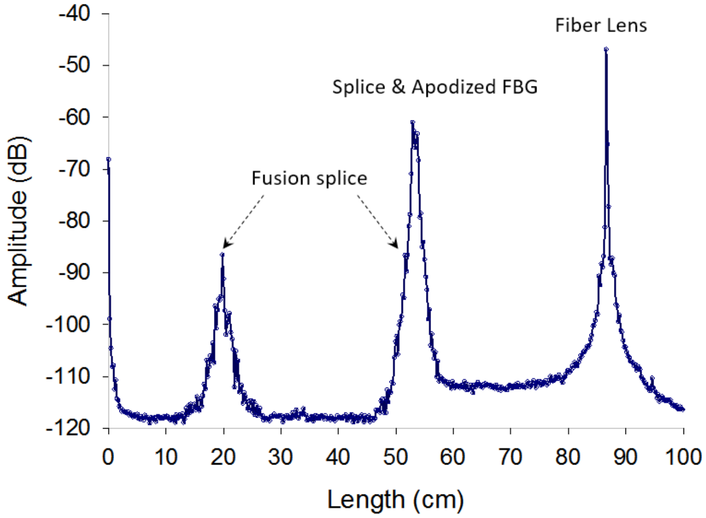

Figure 3.1: (a) Schematic of the hybrid laser showing its main components assembly. (b) Optical backscatter reflectometer (OBR 4600) spectrum of the fiber cavity illustrating the exact length of each fiber section in the hybrid laser device, where the scan range of the OBR is set to 41 nm (1525-1566 nm).

One end of the fiber cavity is sculpted into a micro-lens while an FBG, catered at 1527.8 nm, is directly written on the other end. The 1-cm-long FBG with a peak reflectivity of 70% at a Bragg wavelength ~1527.8 nm is raised-cosine apodized to suppress secondary lobes. The absorption of this PM fiber is measured at 1528 nm to be ~30 dB/m as can be seen in Figure 3.2. The SOA is designed for C-band operation with a high optical power gain at a maximum current of 350 mA. The reflectivity of the rear-facet of this SOA is enhanced to 90% while the front facet is AR coated. The fiber micro-lens is hyperbolic, designed to couple the elliptical diverging light beam from the SOA into the fiber core with high efficiency.

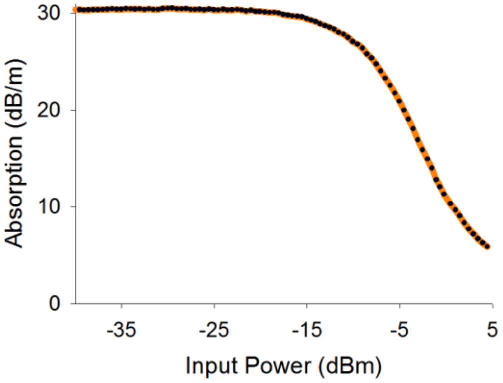

Figure 3.2: Absorption of the PM-ED fiber cavity measured at a wavelength of 1528 nm.

3.2.1 Why polarization maintaining fiber?

In an anisotropic material, the birefringence refers to the dependence of the refractive index on the polarization direction or, in other words, the dependency of the velocity of light on the polarization direction. In standard single mode fibers, any external asymmetrical stress induces birefringence through the photo-elastic effect [51]. The stress-induced phase difference lifts the degeneracy of the polarization state. In single frequency hybrid lasers, maintaining the polarization state is essential for achieving a stable dynamic grating by an intense standing wave and it is necessary to avoid polarization mode dispersion. In PM fibers, the threshold of the photo-elastic effect to take place is highly increased and hence, the amplitude of a given electric field has a higher chance to be preserved. A scheme of PANDA PM fiber is illustrated in Figure 3.3, where the core is placed between two boron-doped stress rods along the fiber [52]. Those stress rods have a larger thermal expansion coefficient compared to that of the cladding (an order of magnitude). During the fabrication process, tensile stress is generated between the stress rods as they shrink more than the cladding. The flanked core is then frozen in tension. The stress-induced birefringence creates a higher core refractive index in the plane of the applied stress forming the slow axis. As a result, two orthogonal polarization states forcing a given mode to propagate at a low or fast speed, with the electric field oscillates along the slow or fast axis, respectively.

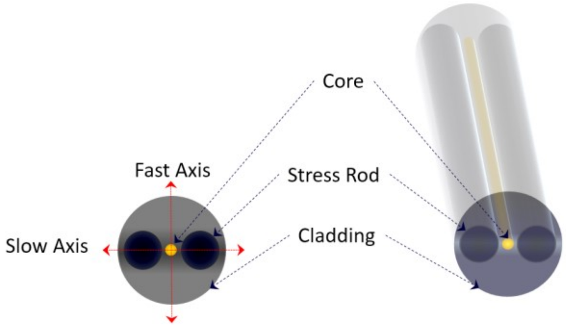

Figure 3.3: Schematic of a Panda fiber cross-section illustrating the core between the two stress rods.

The external cavity, developed in this work, is a single mode PM-ED fiber (PANDA fiber from CorActive with birefringence of $1.14\text{x}10^{-4}$). Thus, maintaining the polarization is possible once the linear polarized light is coupled with either slow or fast axis, where the fiber cavity will be inserted in a ~3-cm radius circular groove. In our setup, the light emission of the SOA is linearly polarized. This polarized light wave is then appropriately coupled to one axis of the PM fiber, which in this case is the slow axis of the fiber cavity. Thus, the energy of the standing wave intensity will be confined to the slow axis plane along the fiber cavity. In Chapter 7, this will be shown to have a vital role in stabilizing the operating frequency of the device.

In the case of random coupling, the polarization may be a combination of two orthogonal polarization states as a stress-free positioning is not convenient for packaging the device. In this case, the variation of the phase difference is subject to the external perturbations and, also, will undesirably contribute in broadening the laser linewidth. So, it is desired to align the polarization axes of the SOA and fiber cavity.

3.2.2 Why erbium doped fiber?

The spectral characteristics of ED fiber locate within the optimum transmission window (at 1.55 μm), i.e., at the absolute minimum of optical attenuation in silica, the fiber substance. From the perspective of the fiber cavity, the spectral location of the radiative transitions of erbium ions is attributed to the fundamental electronic transitions linking the two lowest energy levels, shown in Figure 3.4.

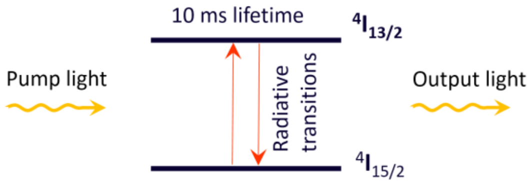

Figure 3.4: Schematic diagram illustrating the relative long lifetime of the upper level and the main electronic transitions between the energy levels of erbium ions, stimulated by the intracavity power flux.

The ground and upper energy levels of erbium ions, $^4I_{15/2}$ and $^4I_{13/2}$, are 8-fold and 7-fold degenerate, respectively [53]. Thus, the local field experienced by each ion is different and have a random value and orientation owing to the amorphous nature of the silica glass matrix [54]. As a result, the absorption and emission cross section of ED fiber has homogeneously broad spectral band. This becomes of great interest to construct hybrid lasers that can operate at any wavelength within the C-band transmission window.

The ED fiber cavity is a saturable absorber, where the depth of the absorption bleaching is dependent on the intracavity power flux as shown in Figure 3.2. The standing wave intensity bleaches the absorption of erbium ions in the fiber cavity producing a large refractive index modulation, translated to a relatively strong dynamic grating via the Kramers-Kronig effect. Thus, a long dynamic grating distributed along the fiber cavity functions as a high resolution band-stop filter, whose narrow bandwidth can only enclose one mode as shown in Figure 3.5. Consequently, the reflectivity of the dynamic grating supports a single mode to dominate the others falling within the bandwidth of the external FBG toward single frequency operation. Also, the dynamic grating is long-lived owing to the lifetime of the upper state $^4I_{13/2}$ (~10 ms), which has a crucial effect in stabilizing the operating frequency against faster environmental and external noise.

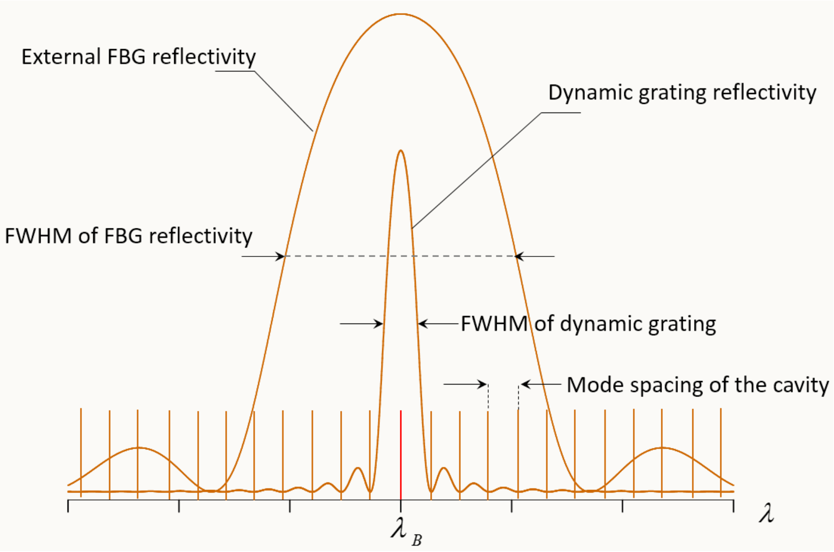

Figure 3.5: Schematic diagram illustrating a single operating mode selected by the dynamic grating while its lasing wavelength is mainly determined by the external FBG.

3.2.3 Fiber lens

In the case of the presented hybrid laser, the fiber cavity was made with a commercially purchased hyperbolic micro-lens, designed to provide a high coupling efficiency. The theory provided here is to understand the shape to arrive at the parameters of the lens that maximizes the coupling efficiency, although these were not the exact parameters used to design it. The guided core-mode radius is $\rho_1 = 2.6\ \mu\text{m}$, the minimum mode radius of the SOA is $\rho_0 = 1.5\ \mu\text{m}$, the refractive index of the fiber core is $n = 1.468$ and the operating wavelength is centered at $\lambda = 1.528\ \mu\text{m}$. Recalling Section 2.4, the optimal coupling efficiency may be obtained when the working distance, D, separating the AR coated facet of the chip from the lens front end, is set to ensure the matching of the divergent beam waist with the guided core-mode radius, i.e., $\rho_1 = \rho_2$ and thus $Z_2 = f$. Substituting ρ_1 and ρ_2 in Eq. (2.40), the working distance is

$$D = \frac{\pi\rho_0^2}{\lambda}\sqrt{\left(\frac{\rho_2}{\rho_0}\right)^2 - 1}\ . \qquad 3.1$$

This working distance, calculated to be $D = 6.55\ \mu\text{m}$, has been considered in all the experiments. The fiber-chip coupling is performed in order to minimize the lasing threshold by maximizing the coupling efficiency based on the working distance of the lens, and the lateral beam exit angle of the SOA, which is discussed in the next section.

Substituting the calculated working distance in Eq. (2.41) to calculate the focal length

$$Z_2 = \frac{1}{D}\left(\frac{\pi}{\lambda}\rho_0\rho_2\right)^2 . \qquad 3.2$$

This gives $z_2 = f = 9.816\ \mu\text{m}$. Substituting the ideal focal length, f , for this fiber-chip combination in Eqs. (2.45)

$$a^2 = \left(\frac{1}{n+1}\right)^2 f^2 \text{ and } b^2 = \left(\frac{n-1}{n+1}\right) f^2 . \qquad 3.3$$

The hyperbola constants are then determined as $a = \sqrt{15.819}\ \mu\text{m}$ and $b = \sqrt{18.271}\ \mu\text{m}$, which are substituted in the following Eq. (3.4)

$$\frac{(z+a)^2}{a^2} - \frac{\rho^2}{b^2} = 1. \qquad 3.4$$

This equation produces the three-dimensional hyperbolic surface of the ideal micro-lens satisfying the amplitude and phase conditions as simulated and shown in Figure 3.6. The two-dimensional profile of this micro-lens is plot in Figure 3.7.

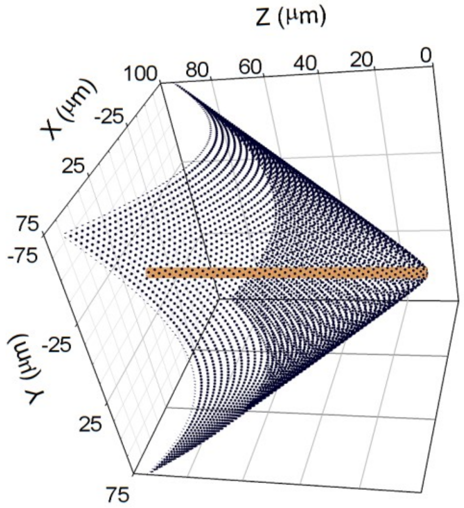

Figure 3.6: Simulation of the ideal hyperbolic micro-lens surface for the demonstrated hybrid laser. This lens allows the optimal coupling of the divergent elliptical beam waist of the SOA to the fiber core while stratifying the phase and amplitude conditions.

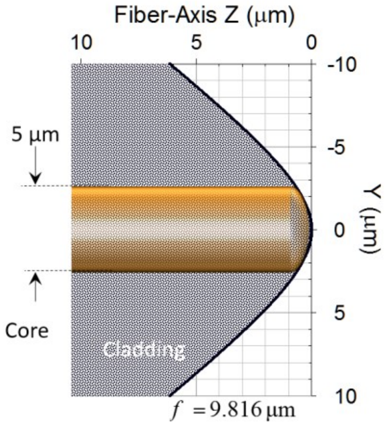

Figure 3.7: Hyperbolic micro-lens profile simulated at $x = 0$ plane.

The illustrated micro-lens is expected to transform the incident wave, emitted by the laser diode, into a plane wave that can propagate in the fiber core with a minimum distortion. Also in order to minimize the loss in practice, the micro-lenses surface is slightly altered to be more biconic because of the asymmetric beam divergence. This is believed to better couple the diverging light beam from the SOA into the fiber core with a high efficiency.

3.2.4 Semiconductor optical amplifier (SOA)

Presently, edge-emitting semiconductor lasers reserve a strategic position in opto-electronic components for the cable television, telecommunication and medical industries. Ridge-waveguide lasers are recognized for single mode operation with a high beam quality. COVEGA's single angled facet (SAF-1126) SOA is chosen to construct the demonstrated hybrid laser. This gain chip is made up of indium phosphide (InP) active region, whose direct bandgap is suitable for optical communication, amplification and detection within the C-band. The SAF-1126 uses a ridge waveguide and proprietary multi-quantum well design offering high power and broad gain bandwidth [55].The front facet is AR coated while the rear-facet of this SOA is enhanced to 90%. In order to remove the residual reflections from the SOA cavity that often limit the spectral quality and the stability of the laser, the ridge waveguide is tilted relative to the front facet to form an angle of 19.5° with the normal as shown in Figure 3.8.

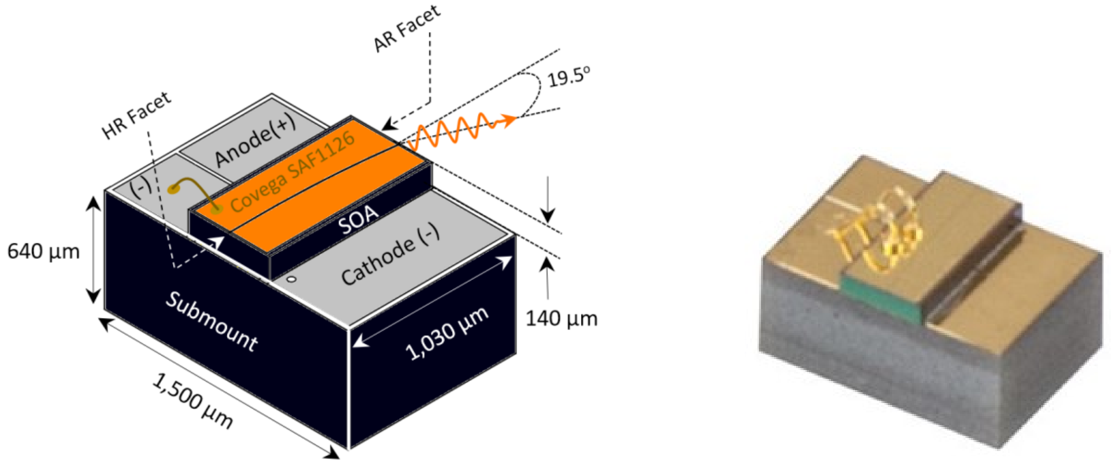

(a) (b)

Figure 3.8: (a) Schematic structure illustrating the physical dimensions of the SOA, SAF1126, placed on a submount. (b) Photograph of the SAF 1126 [55] on the submount.

Eventually, any residual reflection is suppressed and hence, the actual reflectivity of the AR coated facet is reduced to ~10 $^{-5}$ [56]. Most of the inherent feedback, attributed to any resonant cavity formed between the chip facets and the front end of the fiber lens, is therefore weakened and axial mode instabilities are removed. The specifications of this SOA is summarized in Table 3.1 [57].

Table 3.1: Specifications of the Covega's SAF1126, the SOA, used to construct the presented hybrid laser.

Operating current	Max. 350 mA
Threshold current	60- 75 mA
Forward voltage	1.3-1.8 V
Operating wavelength	1528-1568 nm
Front AR coated facet reflectivity	0.001%
Rear HR coated facet reflectivity	90%
Chip length	1 mm
Ridge waveguide refractive index	3.2
Lateral beam exit angle	19.5°
Beam divergence angle (FWHM)	
Transverse	30°
Lateral	16°

The SAF is provided on a heatsink as shown in Figure 3.9, where the electrodes are deposited on insulating pads that are fixed to the heatsink for the laboratory use.

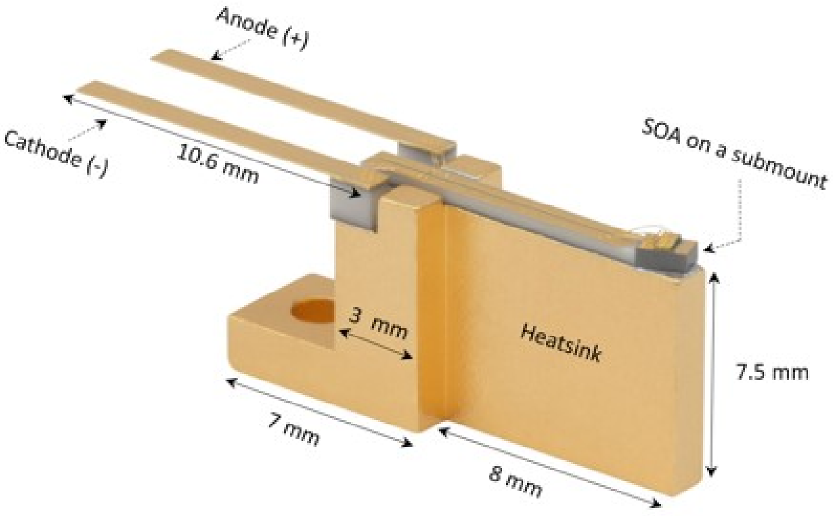

Figure 3.9: Photograph of the SOA, SAF1126 [55], submount is placed on a heatsink, supplied by extended electrodes, whose dimensions are demonstrated.

3.2.5 Thermal stability & assembly

The SOA heatsink is installed on a copper plate, mounted on a 1.5 × 1.5 cm TEC that in turn is placed on a Newport three-axis translation stage as shown in Figure 3.10. The Newport stage is driven manually.

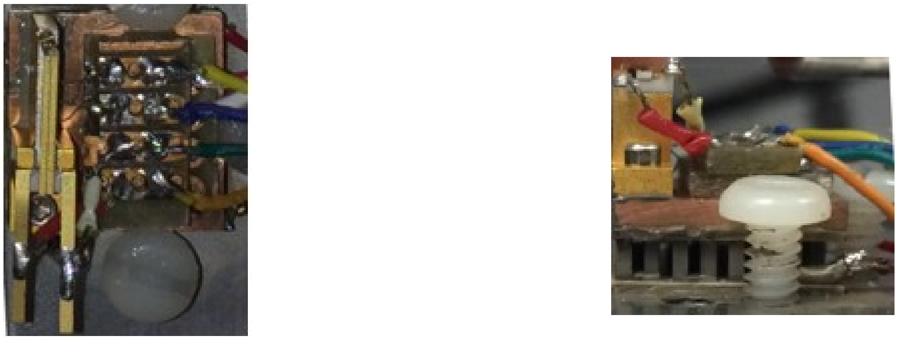

(a) Top view

(b) Side view

Figure 3.10: Photograph of the SOA heatsink placed on a 1.5 × 1.5 cm copper plate, which in turn is mounted on a 1.5 × 1.5 cm TEC.

The fiber cavity including the FBG is inserted in a spiral 280-µm-wide U-groove, engraved on a 7 × 7 cm copper plate whose base is mounted on a 6 × 6 cm TEC as shown in Figure 3.11. The fiber holder unit is fixed on a Nanomax six-axis translation stage assembly, which is remotely controlled using APT software, provided by Thorlab. The stepper motor adjusting the cavity length (x-axis) has a step resolution of 30 nm while the piezo actuators moving on y-axis and z-axis has a step resolution of 100 nm.

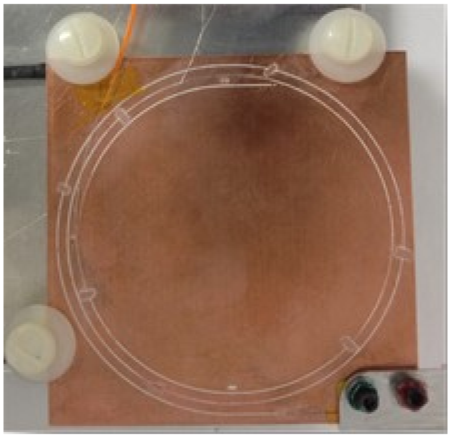

Figure 3.11: Top-view photograph of the fiber cavity inserted in a spiral 280 µm wide U-groove, engraved on a 7 × 7 cm copper plate which is placed on a 6 × 6 cm TEC.

Therefore, a procedure of two steps is executed to couple the fiber cavity to the SOA. Firstly, the SOA is brought manually to a close proximity of the fiber micro-lens as shown in Figure 3.12.

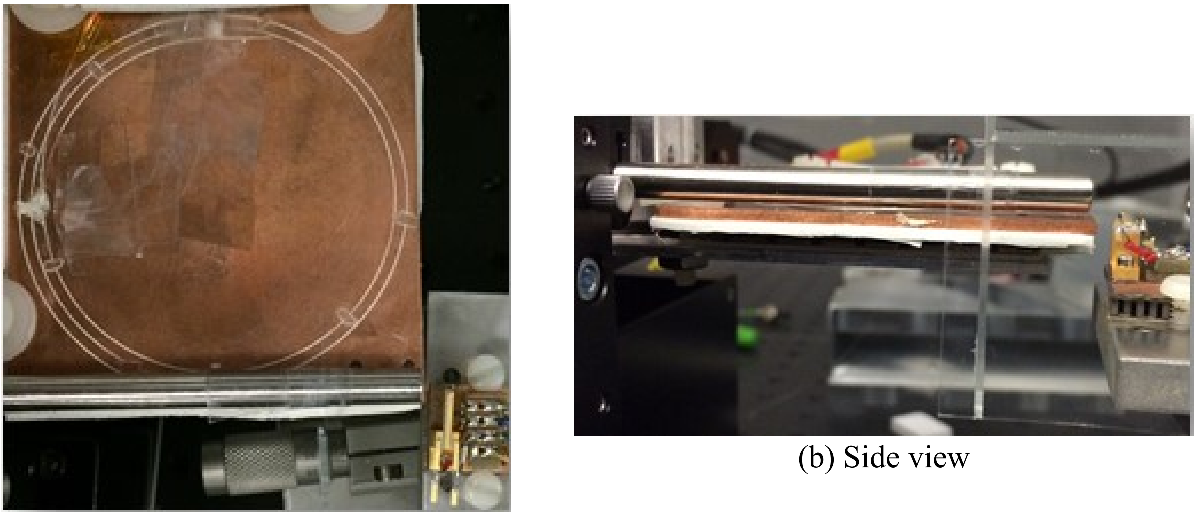

(b) Side view

(a) Top view

Figure 3.12: Photograph of the fiber cavity unit, placed on the Nanomax 6-axis stage that is aligned to the SOA unit fixed on the Newport 3-axis stage.

Using a Thorlab camera, the relative distance between the front end of the lens and the AR coated facet of the SOA is monitored as shown in Figure 3.13.

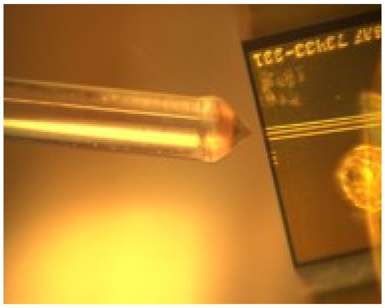

Figure 3.13: Photograph of the fiber-chip pre-alignment.

Secondly using the APT control panel, the fiber-chip coupling are remotely achieved by placing the focal point of the fiber lens at the SOA waveguide port, where the polarization axes of both the laser diode and the slow axis of the PM fiber cavity are aligned. The optimal coupling leading to stable single frequency operation, which may be monitored on optical and electrical spectrum analyzers, as well as the output power that is monitored using a power meter. Thus, the higher the coupling efficiency, the lower the lasing threshold so that the ED fiber absorption can be sufficiently bleached [58].

The temperatures of the fiber cavity and SOA are stabilized and monitored by two separate ILX controllers, LDT-5910B and LCM-39420, installed in an LDC-3900 laser driver system, respectively. Using NI LabVIEW, the drive current, temperature controller and test equipment are remotely controlled and the data acquisition is synchronized.

Every effort is made to enhance the thermal path between the TEC and the SOA or the FBG with all the precautions taken to avoid low-frequency interference noise in the connectors. Optimizing the resistance of each thermistor, thermal noise associated with the steady state error of the PID loop is minimized by choosing the optimal gain values of the ILX controllers. This includes a high temperature sensitivity measured to be 0.6 mK/step. This also ensures ultra-long-term temperature stability for the SOA and fiber cavity as will be seen in Chapter 6&7.

3.3 Conclusion

A hybrid laser has been demonstrated with a 34-cm-long fiber cavity coupled to an SOA. The external cavity has been made entirely with PM-ED fiber without any passive sections. The advantage of using PM-ED fiber to build the external cavity has briefly been mentioned as it provides the dynamic grating that functions as an operational narrow-band filter. Also, it eliminates polarization mode dispersion and hence, the energy of the standing wave intensity is confined to a plane of one axis. The apodized FBG and ideal micro-lens have been presented. The fiber cavity has been inserted in a U-groove that is engraved on a copper heatsink mounted on a TEC, whose PID feedback control system is optimized to eliminate heat generation and thermal noise. The SOA, fabricated with InP along with a curved ridge waveguide design, has been shown to promote a broadband gain and high operational stability. The device has been assembled on the optical breadboard and thermally stabilized using active TECs.

CHAPTER 4 SINGLE FREQUENCY OPERATION

4.1 Introduction

Writing the external FBG and forming the micro-lens directly at the ends of the PM-ED fiber cavity for the first time, the long distributed dynamic grating functions as a high resolution band-stop filter, whose reflectivity will be devoted to a single mode, the only one falls within its bandwidth. A robust device exhibiting single mode operation is therefore resulted. In this chapter, single frequency operation will be theoretically explained and confirmed by optical and electrical measurements.

4.2 Modeling for mode selection

The operational principle of the hybrid laser is based on two gratings. The external 1-cm long raised-cosine apodized FBG and the dynamic grating. As demonstrated earlier in chapter 2, the reflectivity of the gratings can be simulated using the T-matrix method to solve the coupled-mode equations that are given as

$$\begin{aligned}\frac{dR}{dz} &= i\,\sigma R(z) + i\,\kappa_{ac} S(z)\\ \frac{dS}{dz} &= -i\,\sigma S(z) - i\,\kappa_{ac}^{*} R(z),\end{aligned} \tag{4.1}$$

where the amplitudes of the reference $R(z)$ and signal $S(z)$ modes propagating in the +z and -z directions, respectively, are

$$\begin{aligned}R(z) &= A(z)\,e^{i(\Delta\beta z-\phi)/2}\\ S(z) &= B(z)\,e^{-i(\Delta\beta z+\phi)/2}\end{aligned} \tag{4.2}$$

$$\sigma = \kappa_{dc} + \frac{\Delta\beta}{2} - \frac{1}{2}\frac{d\phi}{dz}, \tag{4.3}$$

where κ_{ac} and κ_{dc} are the "ac" and "dc" coupling coefficients, respectively.

The analytical solution of Eq. 4.1 gives the amplitude reflection coefficient

$$\rho = \frac{S(z=0)}{R(z=0)} = \frac{-\kappa_{ac}\sinh(\alpha L)}{\sigma\sinh(\alpha L) - i\,\alpha\cosh(\alpha L)}, \tag{4.4}$$

where L is the grating length and

$$\alpha = \sqrt{\left|\kappa_{ac}\right|^2 - \sigma^2}. \tag{4.5}$$

Therefore, the power reflectivity of the grating is

$$\left|\rho\right|^2 = \frac{\sinh^2(\alpha L)}{\cosh^2(\alpha L) - \dfrac{\sigma^2}{\left|\kappa_{ac}\right|^2}}. \tag{4.6}$$

For the raised-cosine apodized FBG with a fringe visibility of unity, the coupling coefficient κ_{ac} has a functional dependence on the spatial parameter z over the grating length $L = 1.1$ cm and is given as

$$\kappa_{ac} = \frac{\pi\,\Delta n}{\lambda}\frac{1}{2}\left[1 + \cos\left(\frac{\pi(z - L/2)}{L}\right)\right], \tag{4.7}$$

where Δn is determined by the peak reflectivity (70%) of the grating from Eq. 2.26.

On the other hand, the coupling coefficient of the dynamic grating is estimated as [39]

$$\kappa_{ac} = \frac{2\Delta n}{n\,\lambda}, \tag{4.8}$$

where $\Delta n = 1.2\times10^{-6}$ is the periodically spatial variation of the refractive index [58] along the whole length of the fiber cavity $L = 34.26$ cm and $n = 1.468$.

As a result, the power reflectivity of the dynamic grating is simulated and plotted in Figure 4.1. The grating FWHM bandwidth of 2.16 pm is obtained compared to the mode spacing $\Delta\lambda = 2.32\,\text{pm}$.

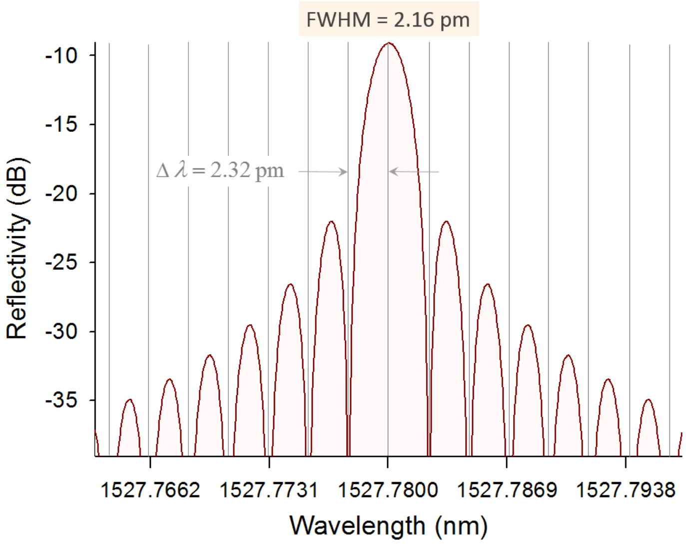

Figure 4.1: Simulated power reflectivity of the dynamic grating is shown along with the spectral locations (vertical lines) of the allowed equally-spaced cavity modes, which all have near zero reflectivity except the one in the main lobe.

The power reflectivity of the external FBG is simulated. The 3-dB bandwidth is found to be 80 pm as shown in Figure 4.2. The SOA's broadband emission covers a wide spectral gain range of 100 nm (1500-1600 nm). The lasing wavelength, which normally drifts towards 1515 nm where the intra-cavity loss is at a minimum, is selected by the external FBG to be around 1528 nm. The mode spacing, $\Delta\lambda = \lambda^2 / 2\,n\,L$, is calculated to be Δλ=2.32 pm (298 MHz) at the wavelength peak λ=1527.78 nm. Thus, increasing the bias current up to the lasing threshold, around 34 EC modes are allowed to oscillate within the FWHM=80 pm of the external FBG's bandwidth. Their standing waves share the same node, located at the SOA's reflecting rear-facet and hence, they may share the same spatial hole-burning pattern in the close vicinity. On the other hand, the optical length of the SOA cavity is 3.35 mm so that the displacement between the side-mode patterns and the central one is at a maximum of ~ ±86 nm from the AR front-facet. Each pattern is associated with a nonuniform distribution of excess electrons and holes. In fact, multi-mode operation is encouraged by such a nonuniform distribution. However in semiconductor lasers, the spatial diffusion of the carriers tends to wipe out the differences in carrier concentrations [59,60]. In the SOA, that diffusion tends to smooth out the gain profile to some extent, which suppresses mode competition unless it is optically synchronized by developing a single dynamic grating centered at the Bragg wavelength of the external FBG. In this case, a fewer number of selected modes are iteratively fed by additional reflection and increasing power leading towards single-frequency operation. This can be explained based on the simulation, shown in Figure 4.2, as the following. The external FBG is apodized to exclude the optical feedback of the side lobes and hence, to increase the SMSR of the laser. The FBG is centered at ~1527.8 nm as the ED fiber exhibits maximum photon absorption [58]. Consequently, the standing wave intensity bleaches the fiber cavity absorption with a refractive index modulation, translated to a strong dynamic grating via the Kramers-Kronig effect [61]. This self-induced FBG functions as a band-stop filter [62] with an FWHM of 2.16 pm selecting a single mode only. A high SMSR can be realized as the other allowed modes have near zero reflectivity as shown in Figure 4.1. Consequently, the reflectivity and the phase matching between the reflected light from the external FBG and the optical feedback of the dynamic grating play a key role in controlling mode competition.

Owing to the spatial distribution of the bleached erbium ions inside the silica glass matrix of the fiber core, the reflectivity spectrum deviates slightly from the theoretical overlap between the allowed side modes and zero-reflections, shown in Figure 4.1. This gives rise to weak side modes that are expected to be observed in the optical and electrical spectra as will be shown later in Figure 4.4 and Figure 4.8, respectively.

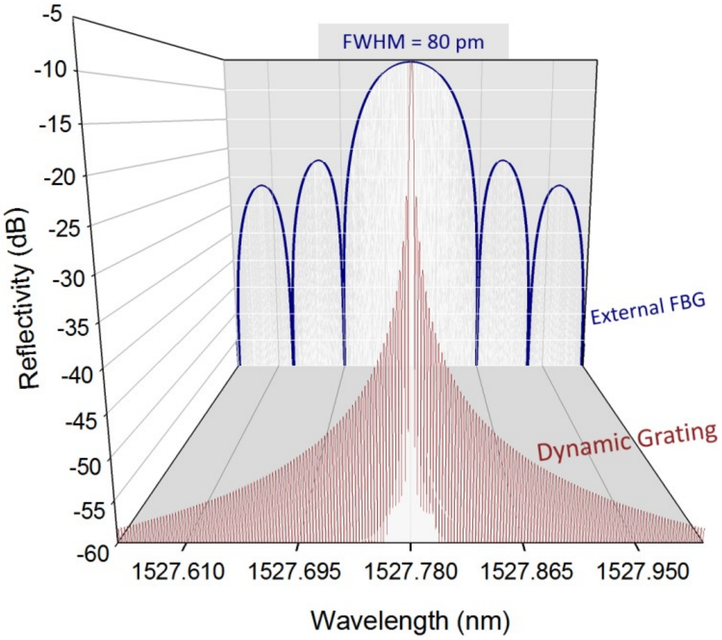

Figure 4.2: Simulated reflectivity of the external 1-cm-long FBG whose FWHM bandwidth is 80 pm compared to 2.16 pm of the 34-cm dynamic grating, zoomed in and plotted in Figure 4.1.

4.3 Experiments

4.3.1 Optical & electrical self-beating measurements

The device is connected to an isolator of ~52 dB return loss as schematically shown in Figure 4.3. APC connectors are used to minimize Fresnel reflection occurring because of sudden changes of the refractive index, which may be driven back to the device. The incident optical power is split by a 1/99 coupler. 1% of the incident power goes to an Anritsu (MU931311A) power meter. 99% of the incident power is then split by another 10/90 coupler. The 10%-power port is connected to a 3dB coupler feeding an optical spectrum analyzer (OSA), Apex (AP2050A), and a Burleigh (WA-1000) laser wave meter, which verifies the presence of a single operating mode within a wider spectral range that cannot be realized by the OSA. The other port of the second coupler delivers 90% of the power to a photodetector, whose electrical signal is monitored on an Agilent (E4446A) electrical spectrum analyzer (ESA).

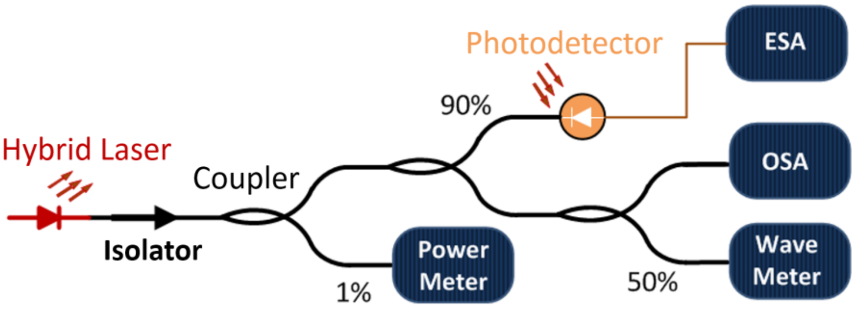

Figure 4.3: Experimental setup to observe single-frequency operation of the hybrid laser.

A bias current of 300 mA is used to drive the laser for 30 minutes. The photodetector receives ~9 dBm optical power and the generated photo current is directed to the Agilent ESA, whose resolution bandwidth (RBW) filter is set to 3 MHz and the trace is averaged.

The optical spectrum, shown in Figure 4.4 [63], is monitored on the Apex OSA, which is set at a resolution of 0.16 pm. A single, symmetrical and very sharp peak with a high relative peak-power confirms single mode operation and exhibits only weak side modes. The Burleigh wave meter, with a resolution of ±0.7 pm, verifies the presence of a dominant mode operating at a wavelength of 1527.780 nm, in agreement with the OSA data.

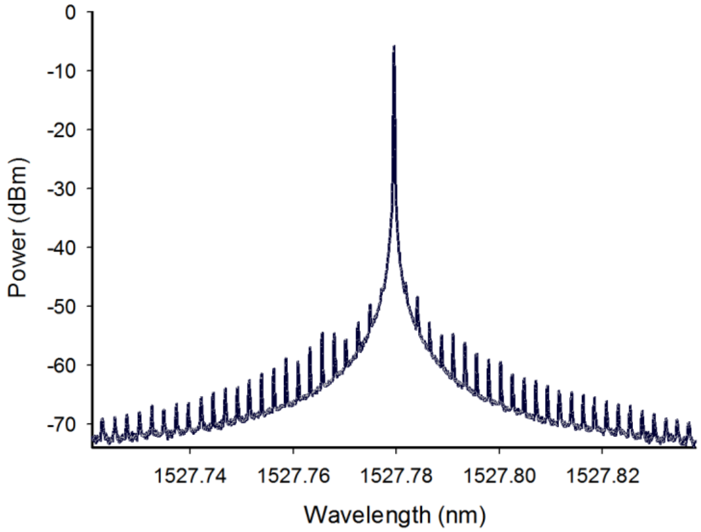

Figure 4.4: Optical spectrum showing a single and sharp spike indicating single-frequency operation.

Another hybrid laser is built with a ~64-cm-long fiber cavity, which is fully made up with the same PM-ED fiber (PANDA fiber from CorActive). This device has a similar design, except for the Bragg wavelength, which is centered at 1548.28 nm. Even though the operating wavelength is red-shifted by ~20 nm away from the wavelength exhibiting maximum photon absorption by erbium ions [58], long-term single frequency operation is also resulted with the same high side mode suppression as shown in Figure 4.5. This indicates to efficient absorption bleaching of erbium ions in the cavity leading to a sufficient depth of refractive index modulation, which in turn is translated to a high resolution band-stop filter via the dynamic grating. Recalling, section 3.2.2, this may be explained by the inherent interaction of erbium ions due the amorphous nature of the silica glass matrix, substance of the fiber core.

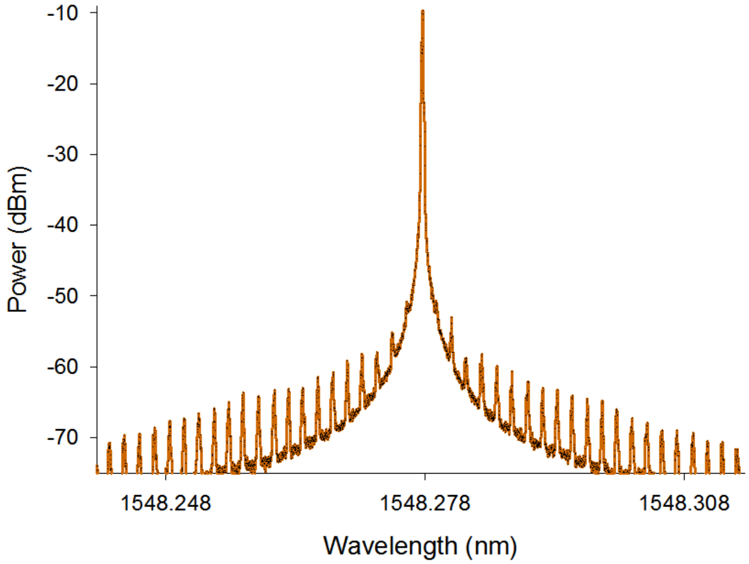

Figure 4.5: Optical spectrum showing long-term single frequency operation at ~1548 nm.

In the electrical spectra, plotted in Figure 4.6, the noise floor is identified when the laser current source is switched off. With the laser switched on, the spectra are taken every 1 second for a period of 30 minutes and plotted together. No mode beats are observed. The only increase above the noise floor is detected within 0-3 GHz range by a maximum of 4 dB. These RF spectra show that there is only a single mode oscillating in the cavity. The amplitude of any RF beat-signals is lower than -74 dBm, which indicates a high SMSR [63]. This confirms the previous results, obtained by the optical measurements. Consequently, a single oscillating mode is inferred. It is worth mentioning that the hybrid device exhibits single frequency operation at any bias current above the lasing threshold which is found to by ~80 mA depending on the fiber-chip coupling.

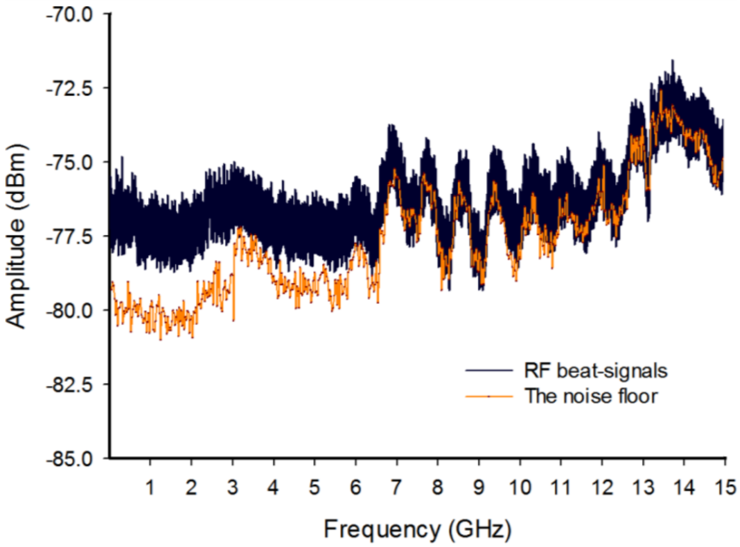

Figure 4.6: Averaged electrical spectra of the hybrid laser, collected every 1 second over a period of 30 minutes, are overlaid (dark lines) and compared to the noise floor spectrum (orange line).

4.3.2 Electrical heterodyne-beating measurements

The mode spacing aforementioned and observed in the optical spectrum, shown in Figure 4.4, may be verified by electrical measurements. However, the self-mode beating spectra do not show any mode beat notes as shown in Figure 4.6, which is expected in the case of single frequency operation. Thus, heterodyne technique may be used to detect those mode spacings and to confirm single frequency operation. The tunable single-mode laser of the Apex is used for heterodyne detection. The experimental setup is shown in Figure 4.7. The incident optical power, passed the 52-dB return loss isolator, is split by a 1/99 coupler. 1% of the incident power is directed to the Anritsu power meter. 99% of the incident power is then divided by the second 10/90 coupler. The 10%-power port is driven to a 50/50 coupler, connected to the Apex OSA and the Burleigh laser wave meter. The other port of 90% power is led to an input of another 3 dB coupler whose the other input is fed by the tunable Apex laser source. Thus, the light waves of the hybrid and Apex lasers will be mixed at the photodetector and the photocurrent will include the heterodyne beat notes, which can be resolved by the Agilent ESA. The operating conditions of the hybrid laser are the same as the previous measurement, shown in Figure 4.4.

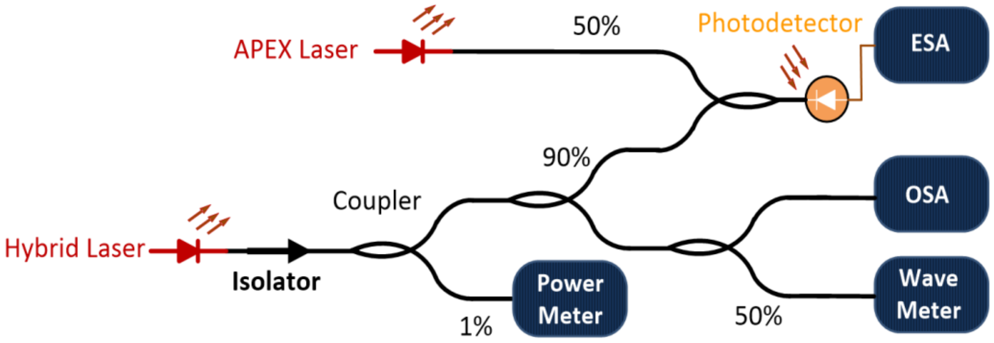

Figure 4.7: Experimental setup to verify the mode spacing and to confirm single frequency operation of the hybrid laser using heterodyne detection.

The electrical heterodyne spectra are plotted in Figure 4.8 [63]. Owing to the 3-MHz linewidth of the APEX laser, the RF beat notes with the first side modes can be barely observed due to a high SMSR of the hybrid laser device. However, the mode spacing is measured from the beating with the subsequent side modes. In good agreement with the optical measurements, plotted in Figure 4.4, it is found to be ~2.32 pm (298 MHz). This proves the side mode suppression and hence, confirms single frequency operation of the hybrid laser.

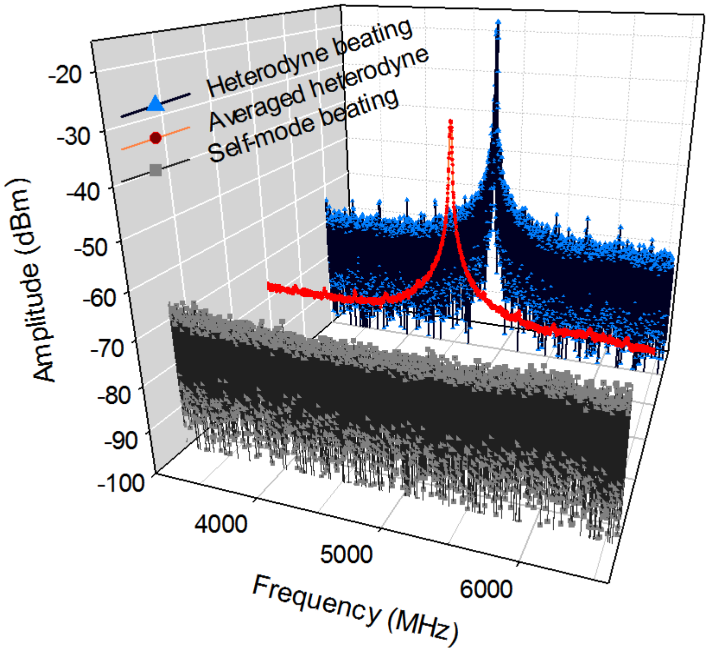

Figure 4.8: Electrical spectra of heterodyne beat notes of the hybrid laser and Apex laser compared to the self-mode beat spectrum of the hybrid laser.

4.4 Conclusion

The optical length of the fiber cavity is 150 times longer than that of the SOA. This usually leads to multi-mode operation because many EC modes fall within the bandwidth of the external FBG reflectivity. Nevertheless, poor single-frequency operation may be resulted, hopping among EC modes within the peak reflectivity of the external FBG in response the differential gain variations, owing to environmental conditions. However, the configuration and assembly of the presented hybrid laser have shown a significant improvement of long-term single frequency operation. The concept of integrating an intracavity high resolution bass-stop filter that strictly allows only a single mode to lase has been theoretically presented and experimentally proven. A theoretical model for a single mode selection by a dynamic grating distributed throughout the EC has been performed. Long-term single frequency operation has been confirmed by optical and electrical measurements at any bias current above the lasing threshold.

CHAPTER 5 PURITY OF THE OPERATING MODE

5.1 Overview

The spectral purity of a laser source is measured by the SMSR and linewidth. The linewidth of a laser source is determined by the combination of the quantum-limited spontaneous emission, attributed to the random spontaneous-recombination phase fluctuations [64], and other noise sources affecting the optical cavity length [65,66]. The latter component affects also the frequency stability based on its strength and frequency.

As yet, fiber lasers have shown excellent performance that is more impervious to noise sources relative to semiconductor lasers. This is because of larger intracavity power and negligible change in the refractive index due to the gain variations. However, fiber lasers suffer from a modest power conversion efficiency compared to that of semiconductor lasers. This main limitation can be overcome by using the hybrid laser scheme, where high power of an SOA is combined to a long fiber cavity that increases the cavity photon lifetime and has no spontaneous phase fluctuations. Thus, the in-phase stimulated photons increase with the intracavity power while the spontaneous (random-phase) photons reach their maximum at the lasing threshold [67]. Also, an energy part of the spontaneously emitted photon is stored in the fiber cavity and spontaneous emission rate will therefore be reduced [68]. Consequently, the linewidth reduction due to the cavity extension can be seen in the linewidth $\Delta\nu$ dependence on the EC length as [68]

$$\Delta\nu \propto \frac{\left(E_D l_D\right)^2}{\left(E_D l_D + E_{ex} L_{ex}\right)^2}, \tag{5.1}$$

where E_D and l_D are the optical energy density and cavity length of the laser diode, respectively, while E_{ex} and L_{ex} represent these quantities for the external cavity.

In the case of our hybrid laser where the SOA is AR coated, the continuity of power flow between the SOA cavity and fiber cavity occurs when

$$\upsilon_D\, E_D = \upsilon_{ex}\, E_{ex}\,, \tag{5.2}$$

where υ_D and υ_{ex} are the group velocities of the SOA and the fiber cavity mainly. Substituting Eq. (5.2) in Eq. (5.1) we get

$$\Delta \nu \propto \frac{\left(\upsilon_{ex} l_D\right)^2}{\left(\upsilon_{ex} l_D + \upsilon_D L_{ex}\right)^2} = \frac{\left(n_D l_D\right)^2}{\left(n_D l_D + n_{ex} L_{ex}\right)^2}, \tag{5.3}$$

where the group velocity is related to the group index as

$$\upsilon = \frac{c}{n}. \tag{5.4}$$

Eq. (5.3) shows that the linewidth of a hybrid laser decreases with the square of the optical length of the fiber cavity. Nevertheless, the penalty of extending the cavity length of a laser diode when seeking a linewidth reduction is normally revealed by poor side mode suppression, which prevents the laser from operating purely in a single mode of the external cavity.

Over the past two decades, research effort has been focused on designing, stabilizing and enhancing the spectral purity of hybrid lasers [18,19,23,26,31,35,36,37]. In fact, single-frequency operation was verified but the output power was low compared to results previously reported on hybrid lasers without intra-cavity doped fiber [26,31]. Later, the output power at the lasing wavelength peak was enhanced to ~14 dBm, but this time with a poor SMSR of only 10 dB [35]. This problem was afterwards addressed and the SMSR was enhanced to 16 dB [36]. However, the output power was not specified and the single-frequency regime was also found to deteriorate depending on the SOA drive current or, equivalently, on the intra-cavity power.

In this chapter, the linewidth of our hybrid laser will be revealed by direct measurements. Subcavity formation will be performed since the device is presently not packaged. Thus, the consequent coupled-cavity modes allow the use of self-mode beating technique, which is insensitive to environmental and external noise. Also, a resolution of a half mode spacing, 1.16 pm, will be used to resolve EC modes and measure the actual SMSR at various bias currents. The output power at the peak lasing wavelength will be specified.

5.2 Side mode suppression & maximum power

While a narrower linewidth is intended as the main advantage of a long fiber cavity, the penalty is usually seen by a poor SMSR. In fact, when the cavity is extended, the EC mode spacing decreases as well, which is normally finer than the bandwidth of the FBG and leads to multi-mode operation. In chapter 4, it has been shown that the device has a band-stop filter with a finer resolution than that of the FBG integrated within the cavity. However, the enhancement in the SMSR of a long fiber cavity is still challenging as the mode spacing is usually finer than the band-stop filter. The highest SMSR, reported for a hybrid laser with a 28-cm-long intra-cavity ED fiber, was 16 dB [36]. As explained in section 1.6, this modest SMSR may be attributed to a partial occupation of the ED fiber in the 67-cm-long fiber cavity.

5.2.1 Experimental setup & results

Long-term single-frequency operation of our device has already been confirmed in Chapter 4. In order to measure the SMSR and the power at the peak lasing wavelength. 99% of the device optical power is delivered directly to the Apex OSA. 1% of the incident power is directed to the Anritsu power meter by a 1/99 coupler receiving the power from a 52-dB return loss isolator as shown in Figure 5.1.

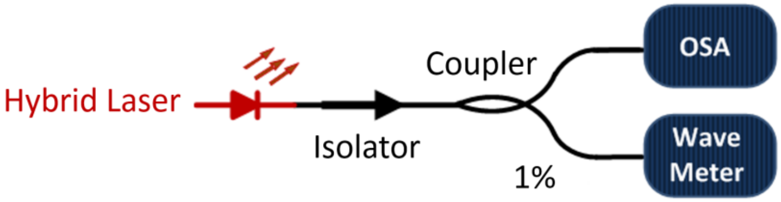

Figure 5.1: Experimental setup to measure the SMSR, the power at the peak lasing wavelength and the output power.

The absolute power accuracy of the Apex OSA is ±0.3 dB. The fiber-chip coupling is set to have a lasing threshold at a drive current of 84 mA. The equally-spaced weak side-modes are detected in the optical spectrum and a SMSR of 42 dB is measured as shown in Figure 5.2 [63]. However at a bias current of 250 mA, the output power at the lasing wavelength peak increases to 11.24 dBm with an SMSR of 44 dB. Recalling Figure 4.1and since the SMSR is defined as the ratio of the power in the dominant mode to that of the strongest side mode, 44-dB SMSR is therefore measured at a resolution of Δλ/2 = 1.16 pm. The significance of this resolution can be realized by recalling Figure 1.12, where the SMSR were measured at a resolution of ~2 nm, the mode spacing of the SOA cavity.

Adjusting the fiber-chip coupling and at the maximum bias current of 350 mA, a higher power is obtained (13.3 dBm), which is very close to the highest peak power (14 dBm) reported previously with a ytterbium doped hybrid laser [35], operating at 976nm. The latter device was, however, pumped by a high-power pigtailed laser producing 300 mW at the current of 500 mA. This shows a clear advantage of our device compared to the ytterbium doped fiber system, in which partial cavity-occupation of the dynamic grating was compensated for by a high intra-cavity flux to reduce the linewidth, following the Schawlow-Townes relationship [69]. However with a SMSR of only 10 dB and 14-dBm peak power, the high power was turned out to be unusable as it was spent on the side mode structure along with noise floor. This is contrary to the purity of our laser where the output power is focused in the operating mode, whose power at the peak wavelength is 13.3 dBm with a SMSR of 44 dB.

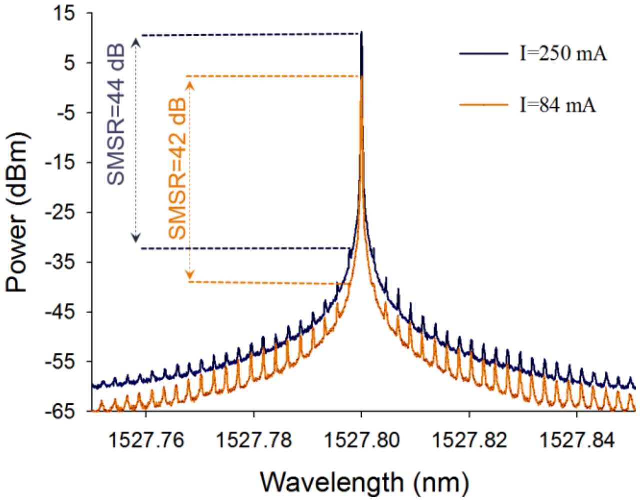

Figure 5.2: Optical spectra of the hybrid device illustrating the equally-spaced side-modes and their SMSRs at different drive currents.

On the other hand, the SMSR of a commercial DFB laser (Lucent D2570H57) [70] is found to be strongly bias-current dependent as shown in Figure 5.3 [71]. Setting the power at the peak wavelength to be close to that of the hybrid laser, a 25-dB SMSR of the Lucent DFB laser is measured as illustrated in Figure 5.3.

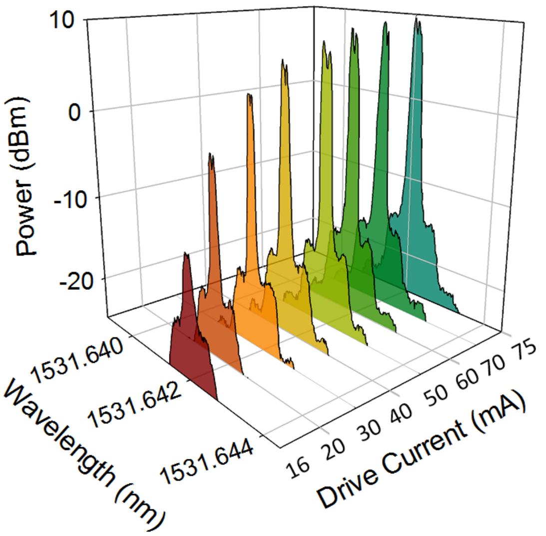

Figure 5.3: Optical spectra of a commercial DFB laser illustrating a strong dependency of the SMSR on the drive current. The double peaks of the single mode are observed as the OSA is set to be polarization independent [71].

As a matter of fact, the variations of the spectral purity with the bias current may impose conflicting constrains when it comes to precision wavelength tunability. Apart from a higher SMSR, this clarifies another advantage of our hybrid laser.

5.3 Linewidth measurement

The demonstrated device is currently not packaged and the fiber lens of our device is held presently in free space. The cavity length fluctuates, as does the lasing wavelength, in response to environmental noise and transient thermal drifts, associated with the variations in the power flux through the fiber-chip connection. This severely restricts the resolution of linewidth measurement whether it is based on the delayed self-heterodyne interferometer or heterodyned with an external oscillator. Fortunately utilizing the coupled-cavity modes, the electrical self-beat notes are insensitive to the above mentioned instabilities.

5.3.1 Theoretical study of subcavity modes

By precise positioning, the reflection on the front end of the fiber lens may be sufficient to form a subcavity [72,73]. The front facet of the SOA has an AR coating, so that the subcavity is formed between the fiber lens and the rear reflecting facet of the SOA. However, the subcavity optical length is determined by the number of the multi passes, *N*, made by the wave that has coupled back to the SOA cavity's field with an efficient field overlap [72]. The effective field reflectance of the subcavity with the appropriate phase factor is expressed as [73]

$$R_{eff}(L_{sub},\lambda) = R + \frac{1-R^2}{R}\sum_{N=1} C\left(\sqrt{RR_f}\exp(-i\,2\pi\frac{n_{sub}L_{sub}}{\lambda})\right)^{2N}, \tag{5.5}$$

where R_f is the reflectance of the fiber lens, $C \equiv C(2Nn_{sub}L_{sub})$ is the overlap integral of the laser mode field and $n_{sub}L_{sub}$ is the optical length of a single pass in the subcavity.

Also, the hybrid laser can be modeled as three coupled Fabry-Perot cavities: i.e., the chip, air and the fiber. The effective field reflectance of the equivalent cavity is given as [74]

$$R_{eff}(L,\lambda) = \frac{R_A\left(1-R_f\rho g_f\right)-g_{air}\left(R_f-\rho g_f\right)}{1-R_AR_f g_{air}-R_f\rho g_f+R_A\rho g_{air}g_f}, \tag{5.6}$$

where R_A is the reflectance of the AR coated facet. The roundtrip gain in the fiber cavity is

$$g_f = \exp\left(-2a_f nL - i\,4\pi nL/\lambda\right) \tag{5.7}$$

and a_f is the fiber cavity loss coefficient, which is negligible when the absorption is fully bleached.

$$g_{air} = \exp\left(-2a_{air}d - i\,4\pi d/\lambda\right) \tag{5.8}$$

is the roundtrip gain in the gap d separating the fiber lens and the AR coated facet of the SOA, where a_{air} denotes the related loss coefficient. Recalling Eq. (4.6), the FBG reflectance $\rho(\lambda)$ is the square root of the power reflectivity obtained from the solution of the coupled-mode equations, executed by the T-matrix method giving

$$\rho(\lambda) = \sqrt{\frac{\sinh^2(\alpha L)}{\cosh^2(\alpha L) - \frac{\sigma^2}{|\kappa_{ac}|^2}}}. \tag{5.9}$$

Satisfying the resonance conditions at the same wavelengths, the subcavity and fiber cavity modes can be coupled and their reflectances add when they are phase matched. As a result, gain mode competition in the SOA is disturbed by the optical feedback of the subcavity, which gives rise to side modes whose amplitudes are determined by their spectral positions within the reflection profile of the external FBG.

5.3.2 Experiment & results

The device is connected through an isolator of ~52 dB return loss to a 10/90 coupler as schematically shown in Figure 5.4. The 10%-power port is directed to a 3dB coupler whose output powers are delivered to the Apex OSA and the Anritsu power meter. The other port of the first coupler carries ~90% of the power to a photodetector, whose photocurrent is monitored on the Agilent ESA.

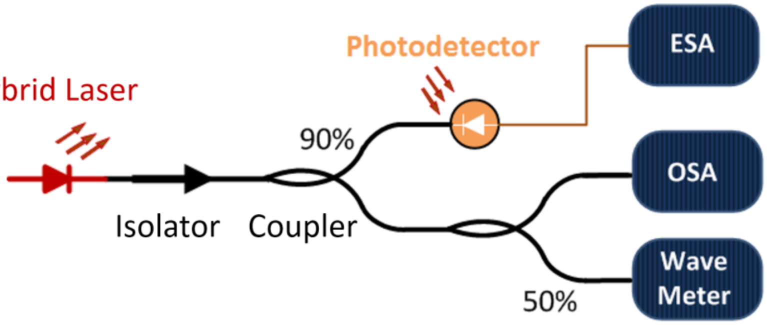

Figure 5.4: Experimental setup to measure the linewidth of the hybrid laser by the coupled-cavity modes, created by the subcavity formation.

Single-frequency operation deteriorates when forming a subcavity by tuning temperature of the SOA and using a stepper motor of the Nanomax stage to adjust the cavity length. Its optical length is set to exactly one-tenth of the main cavity's optical length as deduced from the spectral positions of the subcavity modes, observed in the optical spectrum shown in Figure 5.5(a). The formation conditions of this coupled subcavity are sustained for ~18 seconds and are found to be easily altered to accommodate another subcavity, which in turn initiates different operating modes. Nevertheless, alternative self-recovery of each subcavity is observed. It appears likely that the interplay between the two subcavities is governed by associated heat generation in the fiber cavity and the gain relations among the modes oscillating in the SOA [11].

The number of multi passes, N, constituting the subcavity length between the two reflectors can be estimated using the coupled-cavity model. Simply, any subcavity mode must be coupled to an allowed mode of the hybrid laser cavity to lase. Therefore, phase matching between the two modes has to be met while the subcavity optical length is precisely one-tenth of that of the hybrid laser cavity. In other words, any two consecutive subcavity modes have to spectrally overlap with two suppressed modes and must be exactly separated by 10 mode spacings of the main cavity. Using the effective field reflectance equations, Eq. (5.5) and Eq. (5.6), the above mentioned condition is only satisfied when the optical feedback of the subcavity is simulated with N =15, according to which the results are plotted in Figure 5.5(b) [63].

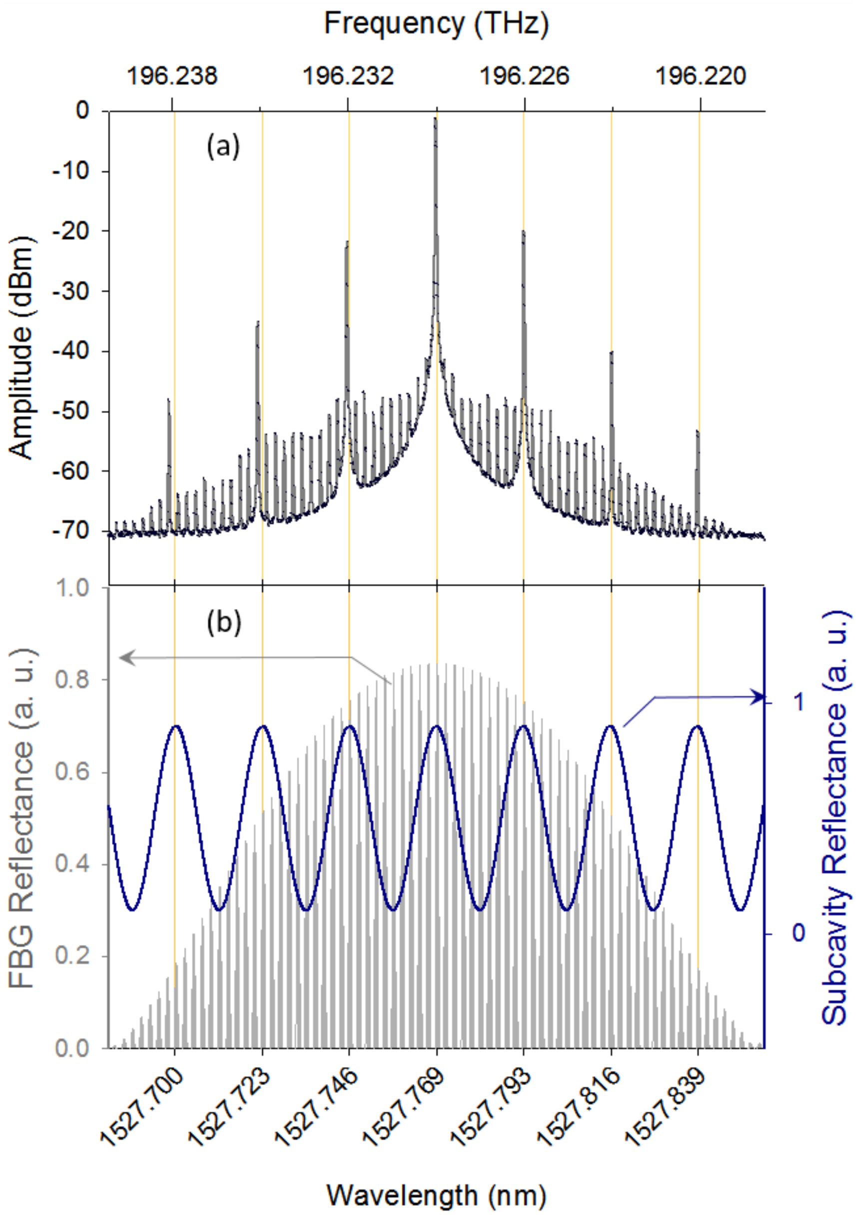

Figure 5.5: (a) Optical spectrum of the hybrid device illustrating the subcavity modes along with the dominant mode, observed in single-frequency operation. The operating modes are spaced equally by 10 mode spacings. (b) Simulation of the effective field reflectance as a function of the operating wavelength is illustrated for the subcavity (blue line) and the hybrid laser (gray line). The reflection peaks of both are overlapped when the subcavity's optical length is constituted by 15 passes (15×3.35 mm), which is exactly one-tenth of the optical length of the hybrid device cavity (50.3 cm). The resultant optical feedback disturbs mode competition and hence, the side modes are observed in the optical measurement and spaced at 10× the mode spacing of the main cavity.

In the electrical spectrum, the power of the strongest beat note, displaced in frequency by 10 mode spacings, shown in Figure 5.6, is mainly attributed to the convolution of the dominant mode with the two strongest side modes at each side, shown in the optical spectrum in Figure 5.5(a).

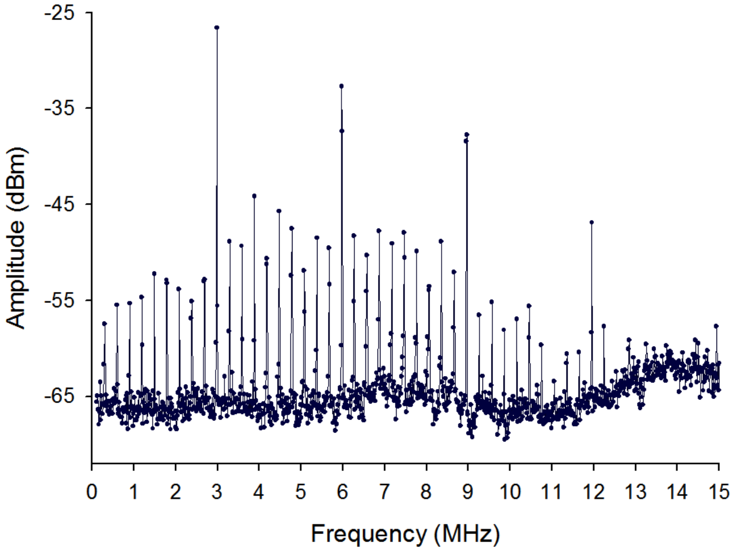

Figure 5.6: Electrical spectrum showing the equally-spaced microwave self-beat notes of the operating modes, demonstrated in the optical spectrum shown in Figure 5.5(a).

The linewidth of this beat note is therefore twice the actual linewidth in single-frequency operation [75]. Therefore, the ESA is centered at the frequency of that beat note as illustrated in Figure 5.7, while the RBW is set to 6.8 kHz. The instantaneous linewidth of our laser is measured to be 2.238 kHz at 3 dB [63].

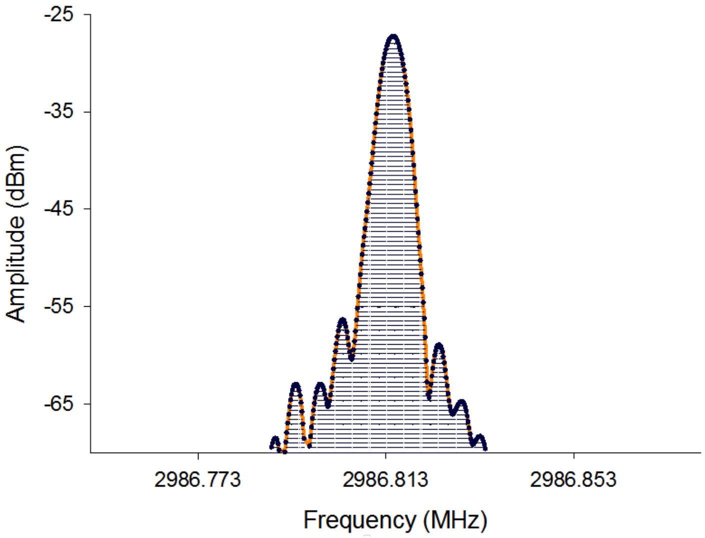

Figure 5.7: Linewidth measurement of the hybrid device using the self-beating technique. The first strongest beat note shown in Figure 5.6 is zoomed in and the frequency is centered at 2986.8 MHz. The instantaneous FWHM linewidth is 2.238 kHz, half the width of the beat note.

5.4 Conclusion

The instantaneous linewidth has been measured to be 2.238 kHz using the self-beating technique. An SMSR of ≥ 42 dB at any current above the lasing threshold has been measured at a resolution of 1.16 pm (149 MHz). This, in combination with a power at the wavelength peak of 13.3 dBm, enables the presented device to operate purely with a linewidth of a single EC mode, giving the device high spectral purity and excellent power efficiency. To our knowledge, the latter two values, 42 dB and 13.3 dBm, have never been reached by any hybrid laser before this work. The linewidth can be further reduced by extending the fiber cavity and hence, this hybrid laser provides an elegant and attractive single-frequency device for WDM systems, coherent systems as well as for RF optical generation using beat frequency in hybrid fiber radio networks, and as a simple source for nonlinear optics using amplification.

CHAPTER 6 TUNABILITY OF THE OPERATING WAVELENGTH

6.1 Overview

The fine-tunability of the EC mode of a hybrid laser has never been demonstrated within a single mode spacing of a few pm. In the past, the tunability with the bias current across tens of EC mode spacings was reported for a 1490-nm hybrid laser [37]. However as already clarified in section 1.6, single-frequency operation of that device deteriorated depending on the SOA drive current. A modest SMSR of 16 dB was attributed to the partial occupation of a 28-cm-long ED fiber in the 67-cm-long fiber cavity, where the mode spacing of the cavity is finer than the bandwidth of the dynamic grating. Eventually, the bias current effect on the spectral purity (or the SMSR) was ignored when the tunability of that device was studied. Regardless the actual SMSR that was not measured, the operating mode found to tune across ~60 modes at a resolution of ~51 MHz/mA when the bias current tuned within a range of 160 mA (30-190mA). Also, a frequency-temperature coefficient was measured to be ~3 GHz/ºC when the temperature of the laser diode tuned at a resolution of 0.1 ºC, while the temperature of the external FBG was not affected. The operating wavelength was therefore tuned within the bandwidth of the FBG to scan 100 pm before it jumped back every 4 ºC [37].

In this chapter, a precision tunability of 2.17 MHz/mA is demonstrated due to the full occupation of the dynamic grating along the fiber cavity. Moreover, at this resolution the operating frequency scans 218 MHz within a single mode spacing, 298 MHz, when the bias current is tuned within a range of ~100 mA [71].

Also by changing temperature of the external FBG while the SOA is thermally stabilized, a range of 1.78 GHz is smoothly scanned without mode hopping at a resolution of ~178 MHz [76], where the SMSR has been simultaneously measured and found to be more than 40 dB.

6.2 Experimental setup

The device is followed by an isolator of ~52 dB return-loss as schematically shown in Figure 6.1. Single-frequency operation and the operating wavelength is monitored on the Apex OSA, whose resolution is set to 0.16 pm. The Burleigh wave meter, with a resolution of ±0.7 pm, verifies the presence of a single operating mode within a wider spectral range. The output power is measured using the Anritsu power meter. The photo current, generated by a photodetector, is directed to the Agilent ESA. An ILX module is used as a current source limited to a maximum operating current of 350 mA, specified for the SOA. The temperature of the fiber cavity and the SOA are stabilized and monitored by two separate ILX controllers, LDT-5910B and LCM-39420, installed in an LDC-3900 laser driver system, respectively. The drive current and temperature controller are remotely controlled using NI LabVIEW and the data acquisition is synchronized as shown in Figure 6.2 and Figure 6.6, respectively.

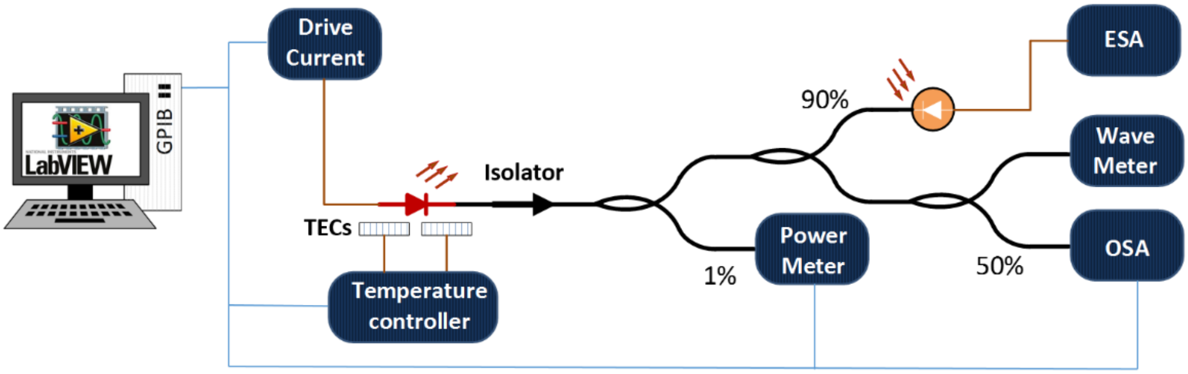

Figure 6.1: Experimental setup to observe the tunability of single-frequency operation of the hybrid laser. The laser cavity’s temperature and bias current are remotely controlled using LabVIEW and the data acquisition is thus synchronized to define the relationship between the lasing characteristics.

6.3 Frequency tunability

6.3.1 Fine & precision tunability

The bias current is programed to ramp-up from a lasing threshold of 81.5 mA to a maximum of 350 mA in 1.5 mA steps every ~10 seconds over a period of ~30 minutes.

While the FBG temperature is fixed at T=23.4011 ºC, the thermal noise, associated with the steady state error of the PID loop, is minimized experimentally by choosing one of the six presets featuring the gain values of the LDT-5910B. The excellent performance of the 16-bit analog-to-digital convertor chip, used in the temperature controller, gives a resolution of 0.6 mK/step as shown in Figure 6.2(b). The accuracy of the current source, LCM-39420 module, is ±100 µA. The current noise changes the refractive index of the optical cavity length, $L_d = 3.35\,\text{mm}$, of the SOA. This affects the spectral width of the laser radiation, or the linewidth. The dependency of the linewidth on the drive current can be derived from the theoretical limit to laser linewidth. The spectral linewidth of a single-frequency laser diode is fundamentally given as [77]

$$\Delta\nu = \left(1+\alpha^2\right)\frac{2\pi^2 h\nu}{P}(\Delta\nu_{cavity})^2, \tag{6.1}$$

where $\alpha \approx 6$ [78] is the linewidth broadening factor, $\Delta\nu_{cavity}$ is the cold cavity bandwidth, $h\nu$ is the photon energy in the operating mode, whose output power is P . The output power is related to the drive current, I , through the probability, η , of the radiative recombination of an injected carrier in the active region [79] and expressed as [80]

$$P = \eta h\nu \, \frac{-\ln\sqrt{R_{FBG}}}{\beta L_d - \ln\sqrt{R_{eff}}} \frac{\left(I - I_{th}\right)}{e}, \tag{6.2}$$

where β denotes the effective internal loss of the SOA, e is the electron charge and $R_{eff} = \kappa_c^2 R_d R_{FBG}$ expresses the combined reflectivity of the reflecting facet, $R_d = 0.9$, and the external FBG, $R_{FBG} = 0.7$ including the fiber-chip coupling, $\kappa_c = 0.9$, which results in a threshold current I_{th} of 81.5 mA. When the laser diode operates as an SOA in a hybrid laser the cavity bandwidth is given by [80]

$$\Delta\nu_{cavity} = \frac{c}{2\pi L_{cavity}}(\beta L_d - \ln\sqrt{\mathrm{R}_{eff}}), \tag{6.3}$$

where the optical length of the entire cavity is $L_{cavity} = 50.3\,\text{cm}$ and c is the speed of light in vacuum. Considering $\beta = 0.1$, $\eta = 0.7$ [81], the linewidth changes with the current as

$$\delta\Delta\nu = \frac{\left(1+\alpha^2\right)}{2\eta L_{cavity}^2}\frac{c^2 e}{\left(I - I_{th}\right)^2}\frac{\left(\ln\sqrt{R_{eff}} - \beta L_d\right)^3}{\ln\sqrt{R_{FBG}}}\delta I. \tag{6.4}$$

Consequently, by virtue of the long fiber cavity increasing the photon lifetime, the linewidth fluctuations due to a current noise of ±100 µA, generated by the current source operating at 250 mA, is estimated from Eq. (4) to be <0.01 Hz. This value can be neglected when investigating the tunability of the 2-kHz measured linewidth.

The change in the absolute wavelength as well as the corresponding output power as a functions of the SOA drive current are shown in Figure 6.2(a).

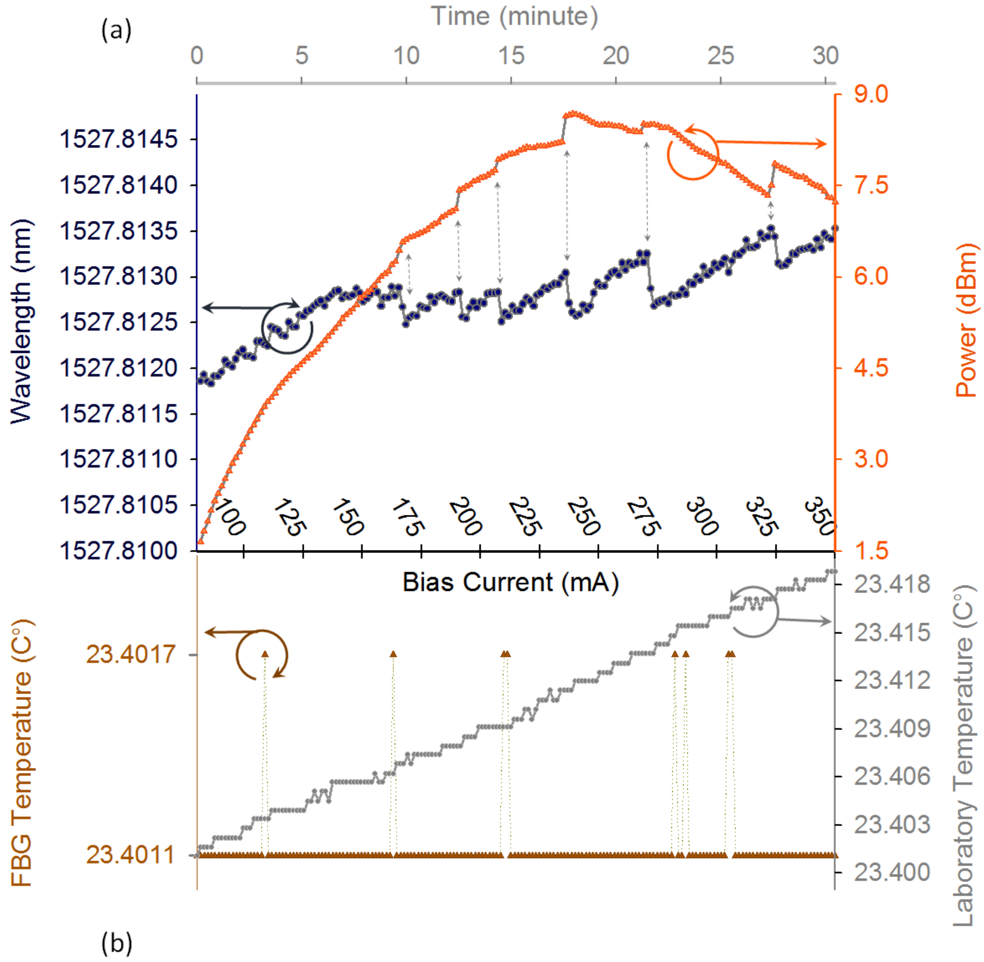

Figure 6.2: (a) Wavelength (blue circles) and output power (orange triangles) of the hybrid laser versus drive current, gradually swept over a period of ~ 30 minutes. (b) Temperature stability of the fiber cavity at T=23.4011 ºC (brown triangles) while the irregular jumps to T=23.4017 ºC are attributed to the airflow affecting the unpackaged copper holder. The gray circles represent the temperature drift of a replica of the fiber cavity holder following the laboratory temperature, measured in the absence of the temperature controller, while the drive current is increased [82].

Despite sweeping the entire current range over a period of ~30 minutes, the device is evidently locked to a single EC mode as the wavelength-shift is measured to be limited to 1.7 pm, which is within a single mode spacing, Δλ=2.32 pm (298 MHz), measured from the data shown in Figure 6.3.

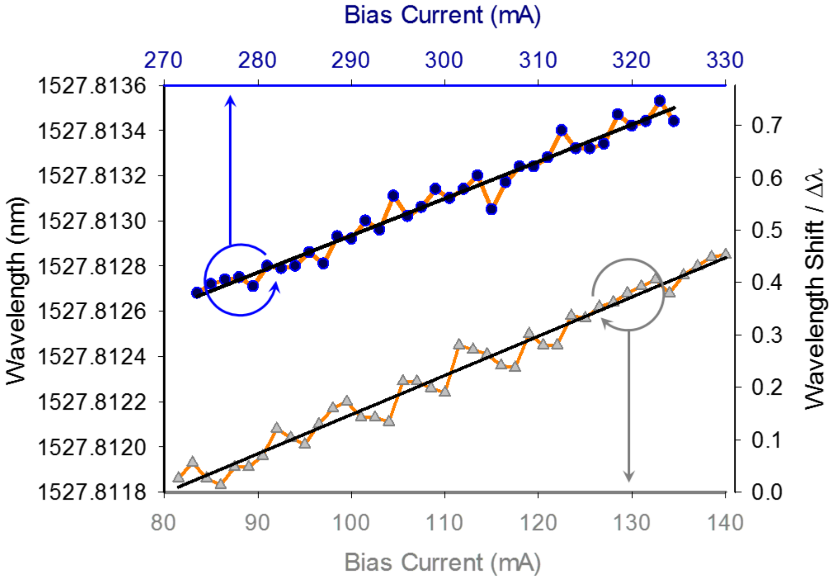

Figure 6.3: Fine-tuning wavelength of the hybrid laser over 1.7-pm spectral range with changing current. The slopes of the lower (gray triangles) and upper (blue circles) fitted lines are 0.0174 pm/mA and 0.0164 pm/mA, respectively. The right-hand axis is offset to an operating wavelength of 1527.8118 nm and normalized to the mode spacing, Δλ=2.32 pm and hence, the wavelength shift within a single mode spacing can be seen clearly.

The measured temperature drift of a replica of the fiber cavity holder, which follows the laboratory temperature in the absence of the temperature controller, is simultaneously recorded and shown in Figure 6.2(b). In fact, the stages holding the SOA and the fiber cavity exhibit different transient thermal responses owing to their heat capacities. This, in combination with the increasing drive current affects the fiber-chip coupling as the fiber lensed end is held in free space and consequently, disturbs the enhanced reflectivity. This happens during the experiment and can be tracked in Figure 6.2(a) by abrupt jumps in the wavelength and the output power, indicated by the dashed arrows. However, real-time calibration is performed manually when observing the RF self-beat signals on the flat baseline of the ESA spectrum. In this way, the full SMSR is quickly recovered and single-frequency operation is maintained by the next reading cycle. Without this intervention a deterioration in single-frequency operation gradually occurs with the drive current as observed in a separate experiment, illustrated in Figure 6.4.

Throughout mode competition initiated in the SOA, a single operating mode dominates by a sequential process of absorbing a mode by an adjacent stronger one. However, this process is not possible unless it is synchronized by the enhanced reflectivity of a developing dynamic grating, which is iteratively fed by additional reflections and the increasing power pushes the cavity towards single-frequency operation. On the other hand, this synchronization may interfere with the optical feedback of a subcavity, created by disturbing the fiber-chip coupling-state and located between the front end of the fiber lens and the facets of the SOA. This explains the deterioration of single-frequency operation observed in Figure 6.4. This limitation can be overcome by attaching the fiber end, held in free space at the moment, to the SOA properly. Also, the SOA is supplied with an intermediate heatsink, shown in Figure 3.9, that can be adjusted as it is not well-suited for our configuration and exacerbates the misalignment.

Figure 6.2(a) shows that the output power, monitored on the Anritsu power meter, increases with the drive current and reaches its maximum value (8.7 dBm) at a current of 239 mA. Further increase in the current decreases the output power because the operating mode tunes to the longer-wavelength edge of the FBG reflection envelope.

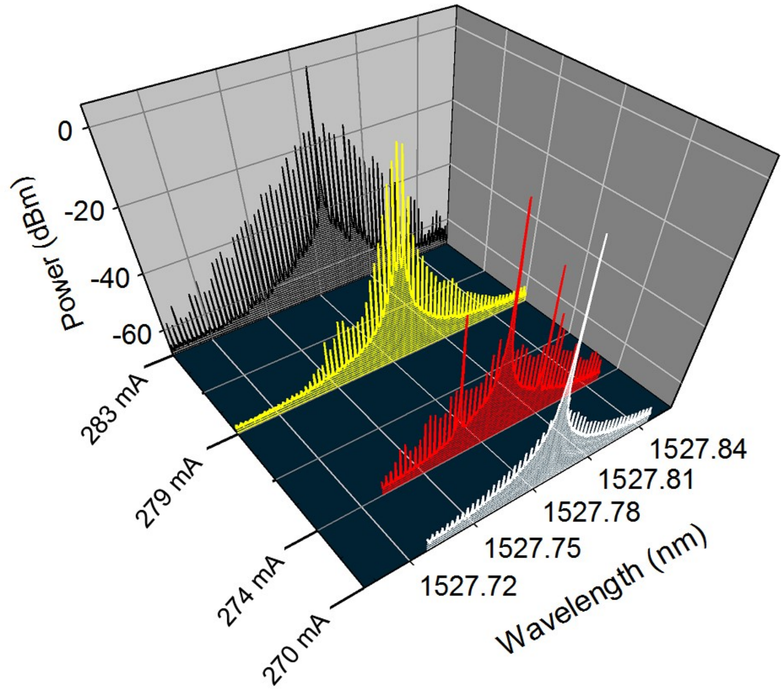

Figure 6.4: Optical spectra of the hybrid device, measured without performing real-time calibration of the fiber-chip coupling, illustrating deterioration in single-frequency operation with the drive current due to the formation of a subcavity between the front end of the fiber lens and the facets of the SOA.

A continuous wavelength tuning range of 1.7 pm (~218 MHz) can be achieved by shifting the drive current from the first range of 81.5-140 mA to 273.5-324.5 mA [82]. The slopes of both fitted lines, shown in Figure 6.3, are very close to each other and can be expressed as 0.0169±0.0005 pm/mA (~2.17±0.06 MHz/mA). This may open the possibility of continuous fine-tunability across consecutive EC modes, which can initially be selected by temperature tuning the Bragg wavelength of the FBG, as shown in the next section.

The wavelength-current coefficient of a commercial DFB laser, (Lucent D2570H57), is measured to be 4.9 pm/mA (~626 MHz/mA) as illustrated in Figure 6.5 [71]. Thus for a given current source, our hybrid laser has shown a 288-fold enhancement in the tunability resolution, shown in Figure 6.5, in addition to a better SMSR that is independent from the bias current, which is in contrast to the DFB laser case, shown previously in Figure 5.3.

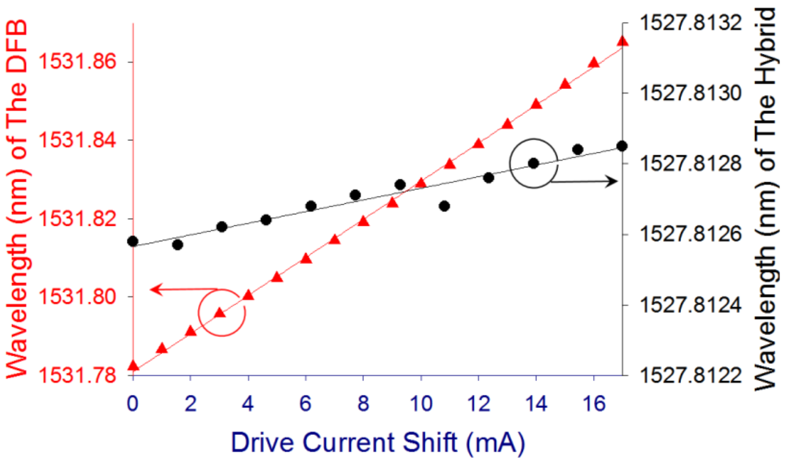

Figure 6.5: Fine tunability of the hybrid laser (black circles) and the DFB laser (red triangles) with shifting drive current. The wavelength-current coefficient of the hybrid laser is 0.017 pm/mA against 4.9 pm/mA, measured for the DFB laser. Some data points deviate from the black fitted line since the hybrid laser is not packaged [71].

6.3.2 Coarse tunability & maintaining high SMSR

The SOA is driven by 230 mA and ~5% of the laser output power is directed to the Apex OSA. The fiber lensed end is lifted from the U-groove in the copper plate and held away to maintain the fiber-chip coupling state while the temperature of the fiber cavity, including the external FBG, is altered in an averaged step of ~ 58.27 mK. This mean value, set digitally, represents the best achieved resolution and varies due to the performance of the digital-to-analog convertor, whose maximum resolution is ~76 µV/step [83]. The SMSR remains high at more than 40 dB as illustrated in Figure 6.6. The operating wavelength is tuned without mode hopping at a resolution of ~1.389 pm (178.4 MHz), which is less than the mode spacing of 298MHz of the external cavity, over a spectral range of 13.89-pm (1.784 GHz), i.e., 6 consecutive mode-spacings, with a wavelength-temperature coefficient of 23.837 pm/K (~3.062 GHz/K) as show in Figure 6.7 [82]. Thus, the operating mode tunes with the Bragg wavelength associated with the cavity length change. However, a tunability over a wider range is subject to mode hops unless the external FBG and the fiber cavity are also separately temperature controlled.

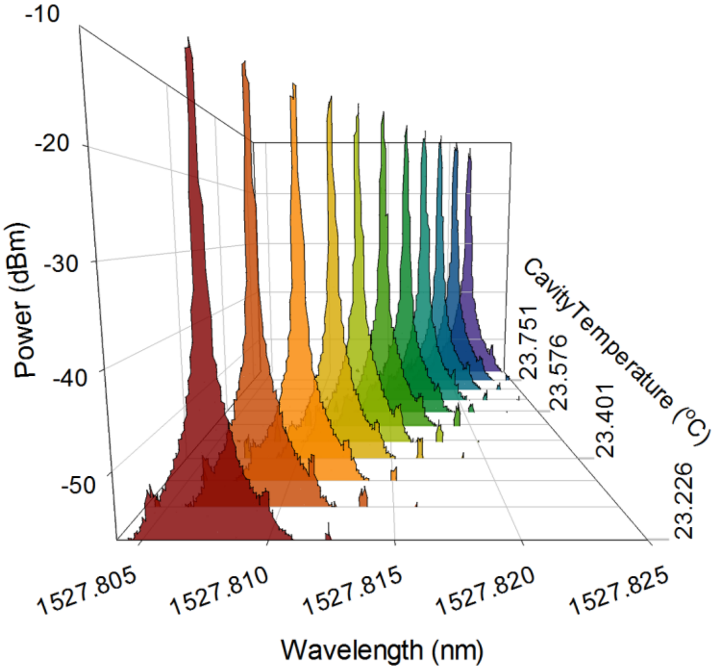

Figure 6.6: Optical spectra of the hybrid laser show a high SMSR>40 dB when tuning Bragg wavelength of the external FBG using a temperature controller.

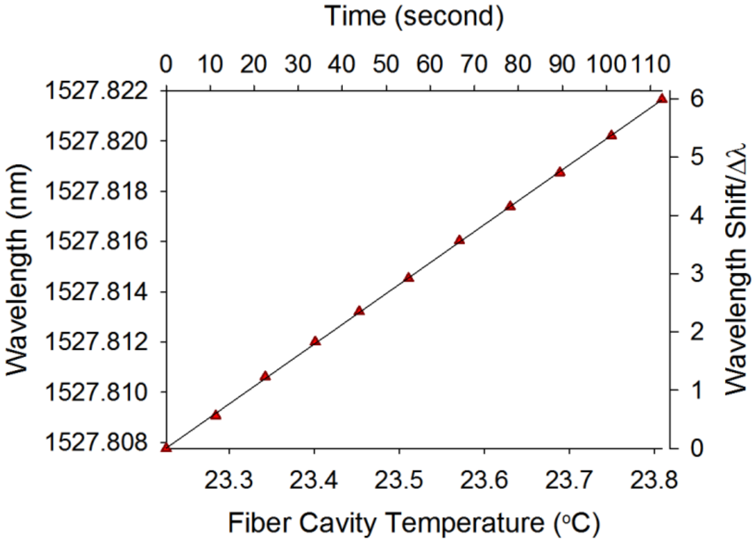

Figure 6.7: Operating wavelength shift when increasing the external FBG temperature in steps of ~58 mK every ~11seconds. The slope of the fitted line is 23.837 pm/K. The right-hand axis is offset to an operating wavelength of 1527.8078 nm and normalized to the mode spacing, Δλ=2.32 pm. Thus, a linear tuning of the operating wavelength across 6 mode spacings at a resolution of 1.389 pm is achieved [82].

In summary, the operating frequency has been tuned linearly at a resolution of 2.17 MHz/mA to scan a spectral range of 218 MHz within 298-MHz mode spacing [82] as schematically illustrated in Figure 6.8. On the other hand, the coarse tunability has been achieved by changing the temperature of the fiber cavity with a step of ~ 58 mK. Accordingly, the operating mode tunes linearly over a spectral range of 1.784 GHz, which is 6 consecutive mode-spacings without mode hopping at a resolution of 178.4 MHz/step as shown in Figure 6.8.

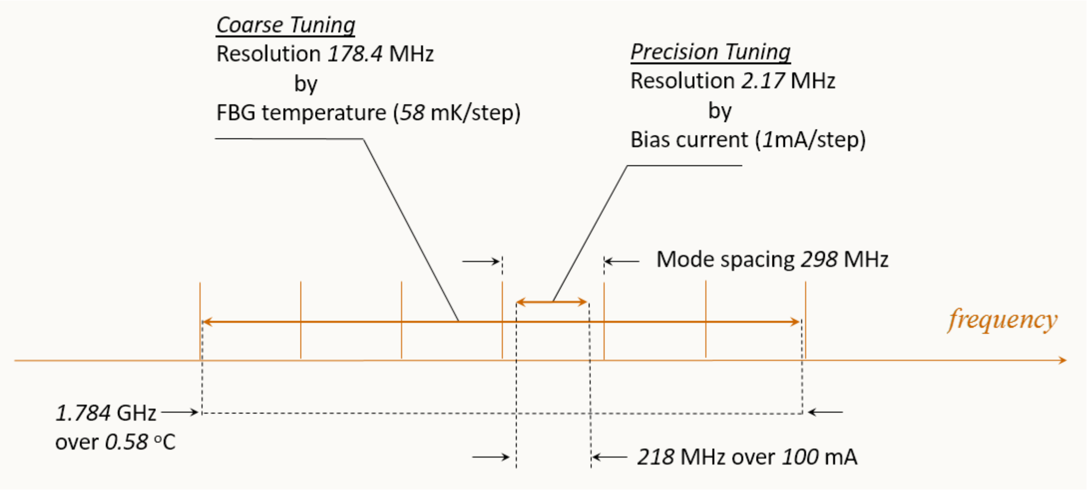

Figure 6.8: Schematic diagram of the measured spectral ranges demonstrating the precision tunability with the bias current and the coarse tunability of the Bragg wavelength with changing FBG temperature.

6.4 Conclusion

The unique tunability of our device has been fully investigated. High-resolution mode-hop free tunability has been achieved within a range of several EC mode spacings for the first time. A linear dependence of the operating frequency on the bias current and FBG temperature has been reported. The noise disturbing the current source accuracy has been found to have a negligible effect on the linewidth of our hybrid laser due to its long fiber cavity. Therefore, the hybrid laser has been demonstrated as a continuously tunable source with a tunability resolution of ~2.17 MHz/mA over a range of 218 MHz, which spectrally locates within a single mode spacing, 298 MHz.

In addition, the thermal noise affecting the cavity length, or the frequency accuracy, has been successfully minimized experimentally and limited to the steady state error of the PID loop which is commercially available at low price for an excellent performance. A resolution of 0.6 mK/step has been measured while the temperature set-point resolution has been enhanced to 58.27 mK/step. Utilizing those capabilities, the operating wavelength has thus been tuned without mode hopping at a resolution 178.4 MHz within the mode spacing to scan a range 1.784 GHz. At the same time the SMSR has been measured and assured to be more than 40 dB. The wavelength-temperature coefficient of 3.062 GHz/K has been measured. Owing to the linear spectral change of the operating mode with the bias current and the Bragg wavelength, a resolution of ~2.17 MHz/mA can be easily transferred to any desired frequency within a given spectral range that may be scanned by tuning the Bragg wavelength with a coefficient of ~3.1GHz/K at a resolution of 178.4 MHz.

CHAPTER 7 STABILITY OF THE OPERATING WAVELENGTH

7.1 Overview

The primary challenge associated with the hybrid laser development is faced in stabilizing operating frequency. Leave aside the question of high stability, the operating wavelength of a hybrid laser with such a long fiber cavity has never been locked to a single EC mode for long-term operation before this work. The high spectral purity of our device, achieved in terms of the narrow linewidth and high SMSR that is independent of the bias current, cannot be fully invested unless the operating mode is stabilized within a minimum tolerance. Utilizing the linearity of the wavelength-to-current curve, a tuning resolution in terms of a few kHz can be reached by using a stable current source, which may be digitally controlled via a high resolution digital-to-analog convertor chip providing a current step of a μA [84]. However in practice, a kHz tunability cannot be deployed unless a much better spectral stability is realized. In fact, high stability permitting such precision tunability is associated with a low phase noise that is desirable for many microwave photonics applications such as distributed antenna systems and coherent detection [85]. For instance, a higher transmission capacity of WDM links is going to be demanded due to the rapidly rising data-traffic volumes, led by the fast development in information technologies [86]. This can be achieved over the preinstalled infrastructures by enhancing the laser wavelength stability of the transmitters, allowing a channel spacing reduction, better spectral efficiency and higher data rate for a given bandwidth [87].

The wavelength stability of an EC laser mainly depends on the stability of the cavity length that can be expressed as

$$\Delta\lambda = \frac{2n}{m}\ \Delta L_{ex} + \frac{2n_D}{m}\ \Delta l_D . \tag{7.1}$$

The change in the lasing wavelength $\Delta\lambda$ as a function of the EC length ΔL_{ex} and the diode cavity length Δl_D whose refractive indices are n and n_D, respectively. Δl_D is mainly the change of the SOA cavity length with the injected current. The effect of this change on the operating wavelength is diluted by a factor of $\frac{m}{2n_D}$, which is ~1.03x10^5 in the demonstrated hybrid laser. Consequently, the main drift in the lasing wavelength can be suppressed by reducing the fluctuations of the fiber cavity length ΔL_{ex} . Fortunately, optical fibers have an inherently high ratio of surface area to core volume [88], which promotes efficient cooling. This allows to maintain the ED fiber cavity length with a minimum change by an efficient thermal stabilizer (TEC). By virtue of the electronic transitions in erbium ions, the operating wavelength can be insensitive to such a trivial change in the fiber cavity length owing to the newly proposed recirculating process. This process along with the dynamic grating will be demonstrated in this chapter as a frequency-stabilizing mechanism, observed by means of synchronized high-resolution measurements. Eventually, it is proven that the device is stabilized under free running conditions without the complications associated with the deployment of a feedback control system.

7.2 Wavelength stability & the PM-ED fiber cavity

Owing to the use of PM-ED fiber constraining the energy of the standing wave intensity in a single-axis plane along the fiber cavity and due to the concentration of the erbium ions, non-radiative transitions amongst the energy levels of erbium ions are possible as previously reported in the literature [89-94]. Based on the laser's operating characteristics, we believe that those transitions can possibly initiate a recirculating process, which will now be discussed in the following sections.

7.2.1 Recirculating process

The concentration of the erbium ions (Er^{3+}) in the fiber cavity is 15×10^{24} m^{-3}, a concentration at which cooperative energy transfer (CET) certainly occurs [89,90]. It was found that, owing to the equally-spaced energy levels in Er^{3+}, an excellent ladder for 1.5-μm upward transitions promotes multistep Er^{3+}-Er^{3+} CET through a quantum-counter process [91, 92], shown in Figure 7.1(a). However, the decay nature and destination of each excited state depends on the host medium [93]. Except for the radiative decay of $^4I_{13/2}$, the decay of Er^{3+} levels in silica-based optical fiber prevails predominantly by strong non-radiative transitions as shown in Figure 7.1(a) [94]. The probability of an upward transition to occur at each level depends mainly on the ion-ion CET rate, which is proportional to the infrared pump intensity [91] or, in other words, to the intra-cavity power. The energy of the intra-cavity standing wave intensity is located within the slow-axis plane of the PM fiber cavity as it is aligned to the polarization axis of the SOA. Two energy levels of Er^{3+}, $^4I_{11/2}$ and $^4S_{3/2}$, with relatively long non-radiative lifetime of ~10 μs and ~0.8 μs [95,96], respectively, are able to recirculate the ion population of the long-lived upper state, $^4I_{13/2}$, through a cross relaxation process as demonstrated in Figure 7.1 [82]. Since the fiber cavity operates in the self-pumped regime (two-level system) with the transit time in the cavity of ~1.7 ns, we believe that the recirculating process can be maintained for a sufficient intracavity power, at which the absorption of the ED fiber cavity is saturated by a smaller value of the SOA pump-power. The recirculating process is proposed here as a plausible explanation for the characteristics of the hybrid laser. However, this has not been proven but remains a suggestion. Currently, this proposal is based on the observation that the lifetimes of the energy levels $^4I_{11/2}$ and $^4S_{3/2}$ seem to match a multiple of the transit time in the cavity. However, this can change for different cavity lengths and extensive experimental and theoretical investigations are therefore needed to verify such a process, to prove its validity.

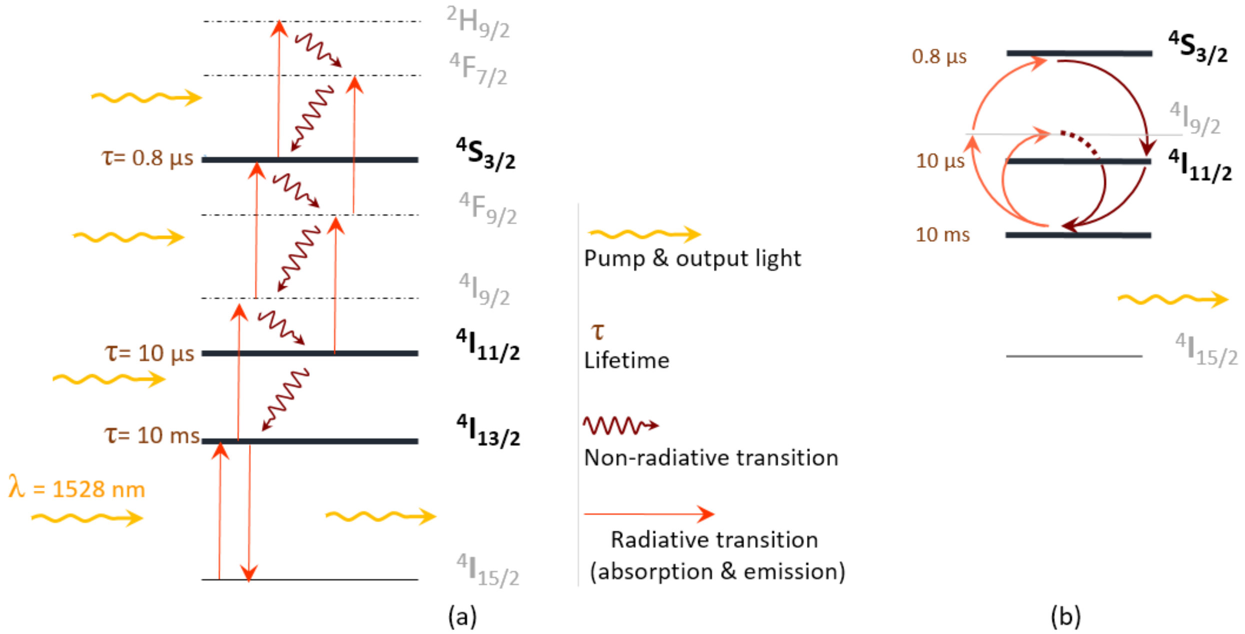

Figure 7.1: (a) Energy levels of Er $^{3+}$ demonstrating the quantum-counter process occurring at the operating wavelength (~1528 nm), non-radiative transitions and the lifetime (τ) of the three energy levels that are involved in the recirculating process while the lifetime of the non-radiative transitions of the other levels are too small and negligible. (b) Schematic representation of the recirculating process. The red arrows represent light absorption and the dark arrows stand for non-radiative transitions among the energy levels, whose non-radiative lifetimes are relatively long [82].

7.2.2 Hysteresis in light-power characteristics

From a similar perspective, single-frequency operation should be maintained even when decreasing drive current below the lasing threshold. Indeed, a significant hysteresis is unprecedentedly observed [82], giving rise to two lasing thresholds based on the fiber-chip coupling state: up-ramp and down-ramp thresholds are observed at 77.4 mA and 55.7 mA, respectively, and separated by 7 dB in output power as shown in Figure 7.2.

When decreasing drive current of the operating laser below the up-ramp threshold (77.4 mA), stimulated photons experience less absorption in each roundtrip than that required to build up the spatial-hole burning pattern. Simply, this is because the absorption is already bleached by the established standing wave intensity and any partial decay in the associated Er^{3+} population inversion is quickly substituted within the cavity transit time of ~1.7 ns. In other words, this hysteresis is not possible unless the population inversion is maintained for low currents. This is because the upper state, $^4I_{13/2}$, is pumped at a rate ~6 orders of magnitude faster than the decay rate. However decreasing drive current, the absorption of the ED fiber cavity as a saturable absorber increases (see Figure 3.2). Thus, the optical power, consumed to maintain that absorption pattern, reduces the output power ~5 times (7 dB) below that of the up-ramp threshold. Below this value the pattern collapses and the lasing mode lacks feedback due to excessive fiber cavity absorption.

For the first time to our knowledge, this high hysteresis in light-power characteristics of such a long doped fiber EC laser is reported. The hysteresis can be expressed as a strong ability of the long-lived dynamic grating to lock the laser to a single operating EC mode with a high SMSR ≥ 42 dB at low drive currents as demonstrated in Figure 7.3 [82]. This explains the discrepancy with what was reported on a long cavity hybrid laser [36], where the single-frequency regime deteriorated depending on the SOA drive current or, equivalently, on the intra-cavity power.

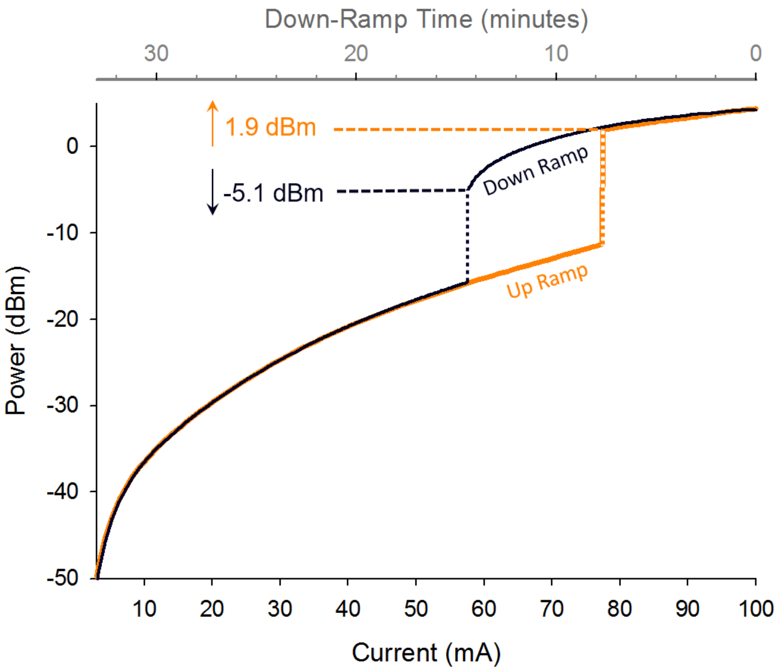

Figure 7.2: High hysteresis in the laser power as the bias current is programed to up ramp from 0-100 mA in 0.1 mA steps every 2 seconds and is likewise down ramped. Two well separated lasing-thresholds are observed at 77.4 mA and 55.7 mA, with output powers spaced by 7 dB.

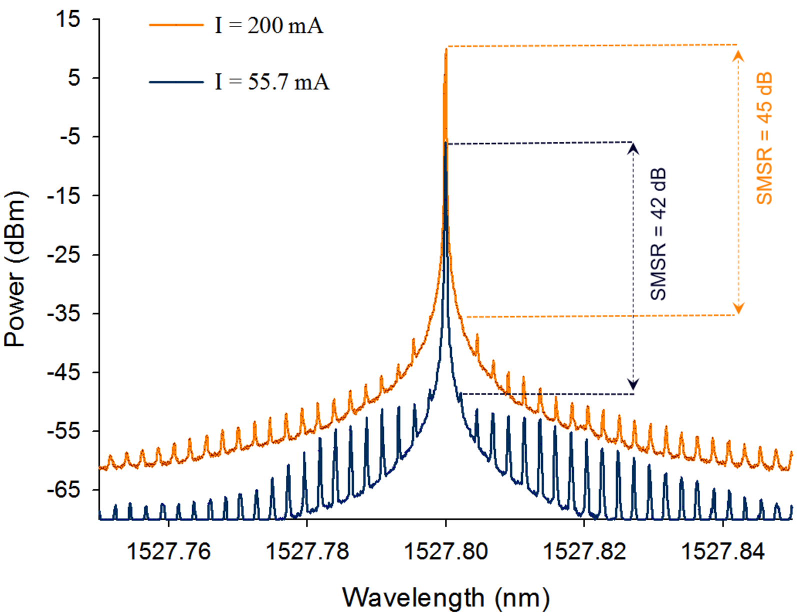

Figure 7.3: Optical spectra illustrating single-frequency operation with a SMSR of 42 dB is observed at ramp-down threshold and maintained at higher drive currents.

7.2.3 Frequency-stabilizing mechanism

An interesting observation, relating the presence of the proposed recirculating process to the frequency stability, is realized. Recalling chapter 6, the wavelength-to-current curve, shown in Figure 7.4, demonstrates that most of the data points have a tendency to deviate from the fitted line at low drive currents, understood to be due to the laser operating under free running conditions. However, this tendency is eliminated at a drive current of ~124 mA. This may be a direct effect of the non-radiative recirculating process. The knee observed in the power-to-current curve, shown in Figure 7.5, illustrating a slower gain in the output power with the drive current may indicate this effect.

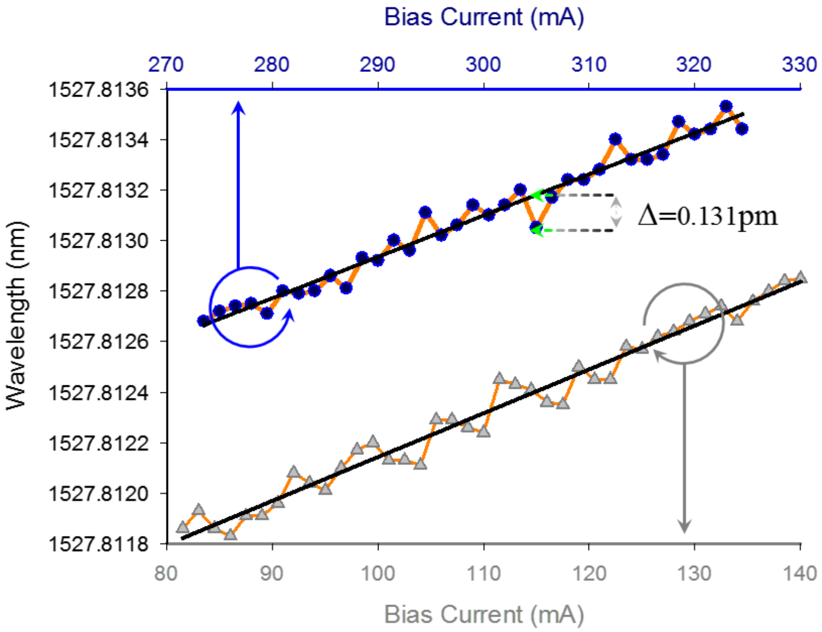

Figure 7.4: Fine-tuning wavelength of the hybrid laser over 1.7-pm spectral range with changing bias current. Long-term wavelength stability under free running conditions, determined by a maximum deviation from the fitted line Δ= ±0.131 pm (±16.8 MHz).

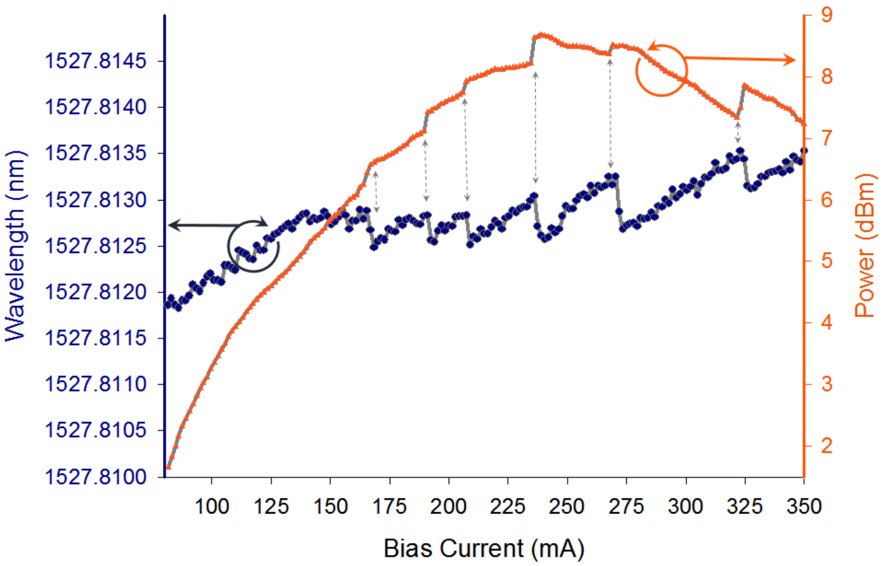

Figure 7.5: Wavelength (blue circles) and output power (orange triangles) of the hybrid laser versus drive current, which is gradually swept over a period of ~ 30 minutes.

Eventually, this recirculating process may be thought of as a frequency-stabilizing mechanism entrenching the spatial energy distribution of the long-lived dynamic grating pattern. Also, this explains the slow gain in the output power with increasing drive current, shown in Figure 7.5, as the intra-cavity power will be shared with the non-radiative transitions of the proposed recirculating process. In other words, the absorption, induced by this mechanism, is expected to be pump power-dependent and increases with the drive current. Inevitable heat generation, associated with non-radiative transitions, increases the optical path length of the fiber cavity including the FBG and hence, contributes to the saturation of the output power at 239-mA drive current, which otherwise should be closer to the lasing threshold (81.5 mA) [82] as shown in Figure 7.5.

In summary, this process helps to stabilize the spatial distribution of the dynamic grating occupying the entire fiber cavity, based on the principle of spatial-hole burning associated with the standing wave intensity. This leads to the refractive index modulation, the Bragg grating, via the periodic absorption bleaching of erbium ions, distributed evenly along the fiber cavity. By virtue of the long-lived upper state of erbium ions whose radiative lifetime is ~10 ms, a maximum cut-off frequency is set [97] so that the hybrid laser is unable to react to faster instabilities, whether originating from the SOA dynamics or due to environmental effects. The possible recirculating process should also resist transient attenuated disturbances of the cavity optical length occurring at low-frequency due to thermal instabilities that cannot be removed by the PID temperature controller. Although those thermal disturbances penetrate the low-frequency filtering effect, set by the long-lived dynamic grating (~100Hz), they get attenuated to a level at which the recirculating process can demolish their effect on the operating frequency. Eventually, the operating wavelength may be locked under free running conditions as will experimentally be demonstrated in the following section.

Moreover, the proposed recirculating process and its role in entrenching the dynamic grating within the energy levels of Er $^{3+}$ may be the reason for the observation of a high SMSR, which remains at more than 40 dB while the operating single mode is coarsely tuned as illustrated in the previous chapter, Figure 6.6.

Even though the recirculating process above mentioned is inferred based on the operational characteristics of the hybrid laser through the well-known nonradiative transitions in Er $^{3+}$, more experimental work on different types ED fibers has to be conducted to prove this process. This may be of great interest for erbium fiber lasers. However, this suggested process is limited to ED fibers where the excited energy levels of Er $^{3+}$, $^4I_{11/2}$ and $^4S_{3/2}$, have relatively long non-radiative lifetimes. Thus, it cannot be applied to explain stability of other doped fibre external cavity lasers, such as the ones made with ytterbium rare earth ions [35], in which there are no other excited states available at a wavelength of 1 micron.

7.3 Stability expected for packaged device

Recalling subcavity formation, used for linewidth measurements and demonstrated in Chapter 5, a subcavity is created. Its optical length is one-tenth of the hybrid laser cavity's optical length. Hence, the self-beat notes of the coupled-cavity modes, observed in the electrical spectrum, are equally separated by 10 mode spacings as shown in Figure 7.6 (a). The electrical spectra of the strongest self-beat note are enhanced up in Figure 7.6 (b) [63]. The ESA is centered at the frequency of that beat note (2986.8 MHz) while the RBW is set to 6.8 kHz. The instantaneous linewidth of our laser has been presented in Chapter 5 and measured to be 2.238 kHz at 3 dB.

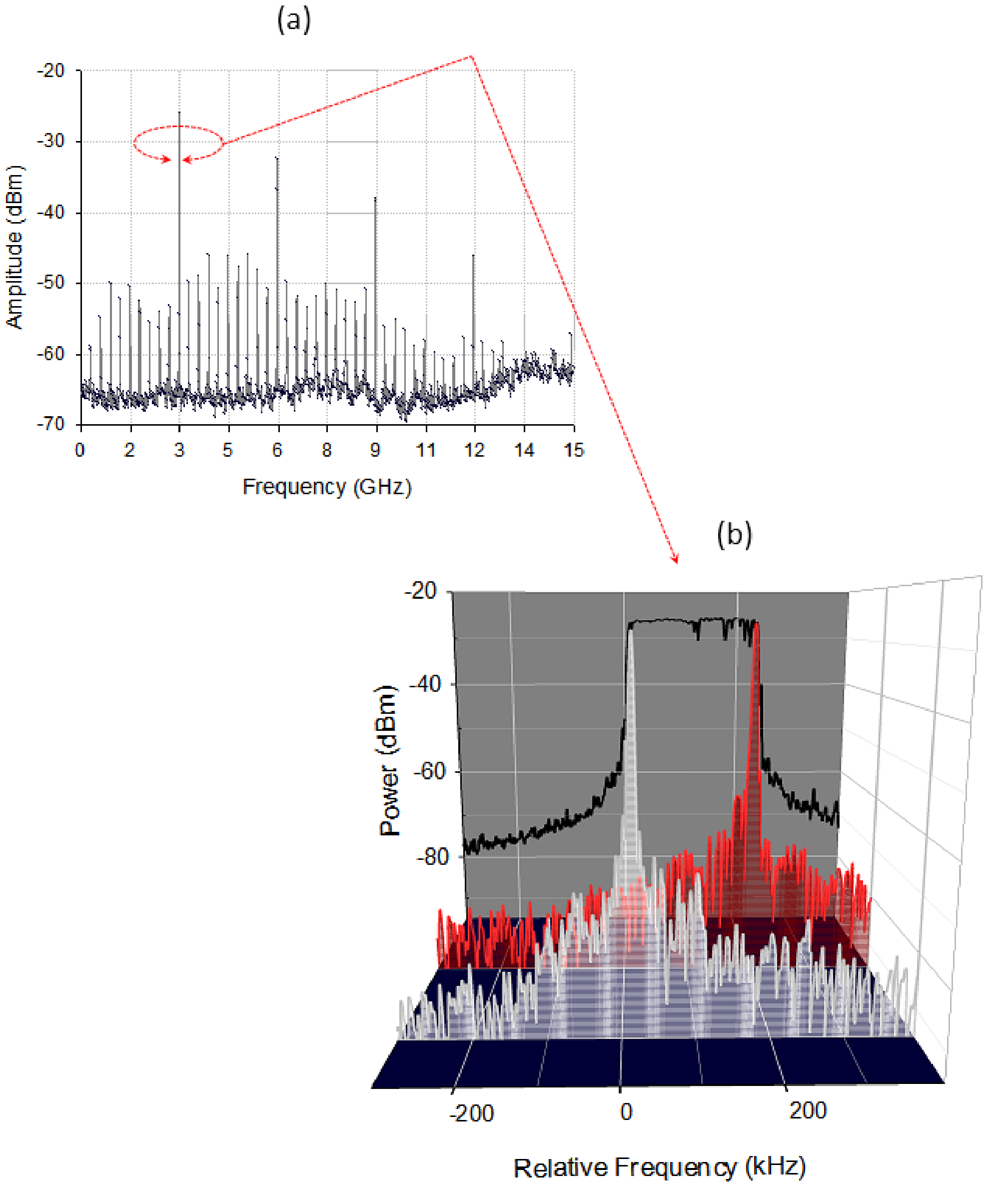

Figure 7.6: Electrical spectrum showing the equally-spaced microwave self-beat notes of the operating coupled-cavity modes (b) Frequency stability measurement of the hybrid device using the self-beating technique. The frequency is offset at 2986.8 MHz. The instantaneous linewidth is 2.238 kHz, half the width of the beat note [75] whose frequency drift, 226 kHz, is demonstrated using the maximum hold option offered by the ESA. The long-term linewidth is deduced to be 2.26 kHz. The difference between the instantaneous and long-term linewidth, 22 Hz, represents the long-term spectral stability of this device once it is packaged.

The subcavity can only be coupled to a stable state of the hybrid laser, whose allowed modes are locked by the condition of phase matching the subcavity modes. Thus within the formation time of the subcavity, the background noise is filtered out by the dynamic gratings and the long-term linewidth of the subcavity can be precisely captured using the self-beating technique. In this case, albeit the three subcavity modes oscillating in the main cavity are subject to the slow response of the associating long-lived dynamic gratings, the long-term frequency drift originates from the frequency fluctuations characterizing the subcavity's linewidth, given by [98]

$$\Delta v_d = \Delta v_{SOA} \left(\frac{\tau_{SOA}}{\tau_{SOA} + \tau_{ext}} \right)^2 . \tag{7.2}$$

τ_{SOA} and τ_{ext} are the round-trip time of the SOA and external cavities, respectively, and Δv_{SOA} is the virtual linewidth of the SOA chip without antireflection coating. Thus, the long-term linewidth of our single frequency laser, $\Delta v_{long-term}$, can be calculated from the measured frequency drift through the following ratio

$$\frac{\Delta v_{long-term}}{\Delta v_d} = \left(\frac{\tau_{subcavity}}{\tau_{cavity}} \right)^2 , \tag{7.3}$$

where $\tau_{subcavity}$ and τ_{cavity} are, respectively, the round-trip time of the subcavity and the main cavity producing single-frequency operation. The long-term linewidth is therefore

$$\Delta v_{long-term} = \frac{\Delta v_d}{100} = 2.26\,\text{kHz} \tag{7.4}$$

Consequently, the long-term linewidth is 22 Hz wider than the instantaneous linewidth (2.238 kHz). Therefore eliminating low-frequency mechanical and thermal drifts by a hermetically sealed package, the long-lived dynamic grating is expected to lock the operating frequency of our device to within ±11 Hz for long-term single mode operation [63]. The stability of such a packaged device that has shown such excellent purity and tunability may be attributed to the long-lived dynamic grating, supported by the proposed recirculating process.

7.4 Stability for unpackaged device

As mentioned previously the fiber-chip coupling is subject to environmental noise, acoustic pickup and mechanical vibrations. Consequently in the case of unpackaged device, the operating wavelength is susceptible to environment conditions' fluctuations, which randomly change the refractive index of the cavity medium affecting the cavity optical length. However owing to the continuity of the dynamic grating, which is thought to be secured by the recirculating process, and high temperature stability, the wavelength stability has been measured for the unpackaged device under free running conditions. The achieved wavelength stability has not been possible before in such a hybrid laser at its best [56,99] as demonstrated below.

7.4.1 Experimental set-up

The device is followed by a ~52 dB return loss isolator. The Anritsu power meter receives 1% of the incident power while the 99% is then split by another 10/90 coupler, whose 10%-power port is driven to the Apex OSA and Burleigh wave meter through a 3 dB coupler. The other port of the second coupler delivers ~90% of the optical power to a photodetector. The generated photocurrent is then directed to the Agilent ESA as depicted in Figure 7.7.

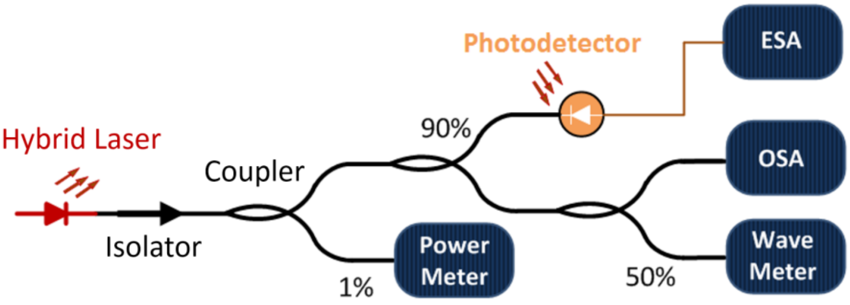

Figure 7.7. Experimental setup to measure the spectral stability of single-frequency operation of the hybrid laser.

Single frequency operation is monitored during the experiment on the Agilent ESA whose spectra show the amplitude RF beat-signals of lower than -74 dBm, which indicates single mode operation with a high SMSR. The laser's long-term spectral stability is measured using the Apex OSA and monitored over a period of 45 minutes while the data is collected every 3.2 seconds. Even though the device operates as a free-running laser that is not packaged, the operating wavelength shows high stability. For the first time to our knowledge, such a long-cavity hybrid laser is locked to a single cavity-mode within spectral fluctuations of ±0.2 pm (±26 MHz) as illustrated in Figure 7.8.

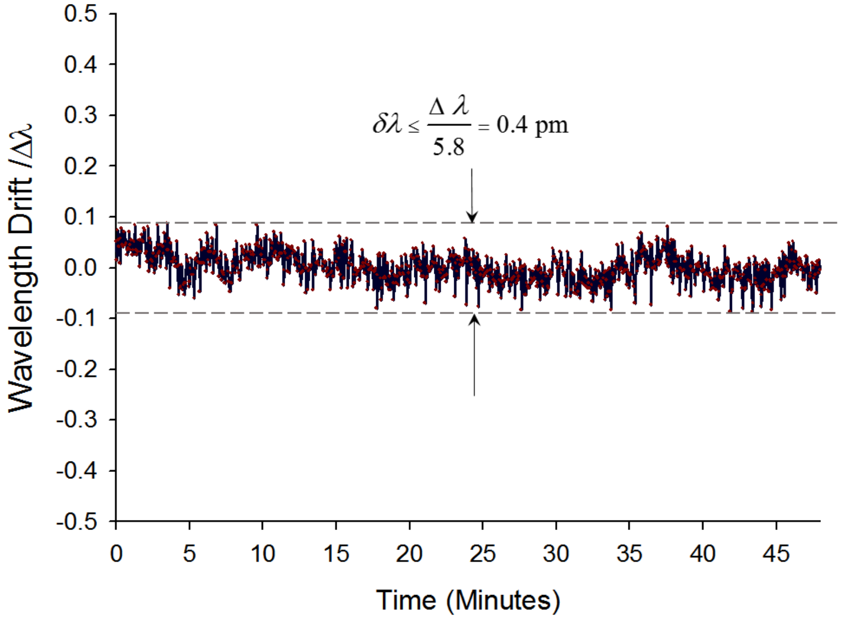

Figure 7.8: Long-term wavelength stability within ±0.2 pm is measured every 3.2 seconds over a period of ~45 minutes and shown in terms of the mode spacing, where the spectral drift is offset to the operating wavelength and is normalized to the mode spacing Δλ = 2.32 pm.

Recalling Figure 7.4, as the data has been collected over a period of ~30 minutes, the long-term stability for this unpackaged device can be estimated from the maximum deviation around the fitted line, which is found to be Δ = ±0.131 pm (±16.8 MHz). This better stability can be understood for the unpackaged device as the experiment conditions are different; the fiber cavity holder was covered by thermal isolating foam and the laboratory was extremely quiet.

Although our device is not packaged, its stability is at least 5-times better than that of a fully packaged commercial DFB laser (Lucent D2570H57), whose stability is measured to be ±1.03 pm as shown in Figure 7.9 [71].

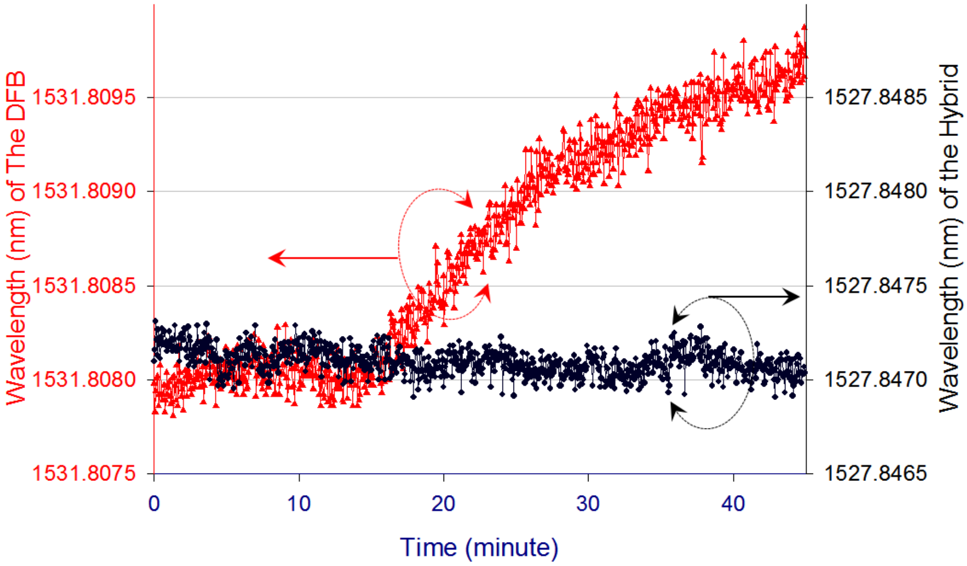

Figure 7.9: Long-term wavelength stability of the unpackaged hybrid laser (black circles) along with that of the DFB laser (red triangles). The stability of the hybrid laser is found to be at least 5 times better.

7.5 Conclusion

The precision tunability of the hybrid laser can only be beneficial if the operating frequency is locked to a minimum drift. Thus, the challenge is to stabilize the operating wavelength in order to transfer the precision tunability to any desired frequency within a given spectral range. It is more challenging to do so under free running conditions. However, this has been overcome by the unique design and assembly of the demonstrated device. Using a PM-ED fiber cavity, a significant hysteresis in light power-current characteristics has been observed while for higher currents the non-radiative recirculating process may be inferred based on the laser's operating characteristics. This has two crucial effects on the spectral purity and stability of single-frequency operation. It maintains single frequency operation with a high SMSR of $\geq$ 42 dB despite a large reduction in the bias current below the ramp-up lasing threshold. Also at high drive currents, the non-radiative transitions are believed to work in conjunction with the spatial energy distribution in the long-lived dynamic grating pattern to promote additional frequency-stabilizing mechanism. As a result, mode-hop free coarse tuning has been possible with a SMSR of $\geq$40 dB as shown in Chapter 6. Therefore, in order to achieve a robust device, the output power and the stability have to be balanced through the Er $^{3+}$ concentration, which determines the absorption bleaching depth and the CET at a given drive current. The design of our device, incorporated with a precise temperature stabilizing loop, has been shown to be a significant improvement over previous hybrid lasers with a long term stability of ±16.8 MHz, associated with an optical cavity-length change of ±43 nm and measured for the unpackaged device under free running conditions. However when the device is packaged properly, a long-term frequency stability within ±11 Hz has been inferred.

Based on the wavelength-to-current curve, non-radiative transitions in Er $^{3+}$ have been found to be power dependent as the number of contributing photons increases with the drive current. On one hand, the proposed recirculating process could have an operational advantage offering additional frequency-stabilizing mechanism, entrenching the spatial energy distribution in the long-lived dynamic grating pattern. Thus, it can enhance the long-term wavelength stability. On the other hand, inevitable heat generation, associated with the non-radiative electronic transitions, imposes thermal noise fluctuating the optical length of the fiber cavity including the FBG and destabilizes the operating frequency. This disadvantage affecting the long-term wavelength stability has been removed by deploying an optimized TEC loop. Consequently, the thermal effect of heat generation has been cancelled out or minimized to a limit, within which the attenuated thermal fluctuations in the optical cavity length cannot affect the spatial distribution of the dynamic grating (or the operating frequency). Consequently stabilizing device temperature, the net advantage of the use of PM-ED fiber cavity can be summarized as follows:

1. It stabilizes the frequency of long-term operation
2. It resists transient low-frequency attenuated disturbances of the cavity optical length that penetrate the maximum cut-off frequency (~100Hz) filtering effect, set by the long-lived dynamic grating.

Indeed, the proof of concept has been verified by promoting a long-term frequency stability of ± 11 Hz for a packaged device operating under free running conditions [63].

CHAPTER 8 CONCLUSIONS AND POTENTIAL APPLICATIONS

8.1 Overview

A hybrid laser, based on a C-band SOA coupled to a long PM-ED fiber cavity, has been carefully engineered to operate with high spectral purity and outstanding stability. Combining the attributes of an FBG, PM-ED fiber and SOA in the thermally stabilized device, a highly stable narrow linewidth laser operating with a high side mode suppression ratio has been locked to a single EC mode. Moreover, continuous precision tunability within the mode spacing in addition to mode-hop free coarse tunability have been demonstrated. In order to determine the performance of this device for any potential application, the following specifications of the hybrid laser operating under free running conditions have been identified.

8.1.1 Single frequency

The FBG selects the operating frequency while dynamic grating selects a single operating mode as follows.

1. The FBG grating selects the operating mode whose frequency coincides with spectral location of the grating peak reflectivity.
2. The FWHM of the dynamic grating bandwidth must be smaller than the mode spacing of the cavity to ensure single frequency operation. This condition has been satisfied by making the fiber cavity with ED fiber, where the FBG and micro-lens are created directly in the ED fiber.

8.1.2 Spectral purity

The spectral purity of our hybrid device has been expressed by the SMSR and linewidth. The SMSR has been maximized by reducing bandwidth of the dynamic grating that is ensured by the full occupation of the ED fiber in the fiber cavity. The linewidth has been reduced by extending the cavity, so that the phase fluctuation due to the spontaneous emission has been diluted as the cavity photon lifetime increases. The SMSR has been optically measured to be always more than 40 dB and has been verified by electrical measurements by using the heterodyne-beating technique. Contrary to previous published results and apart from a better SMSR, our device has shown such a high SMSR at any bias current above the lasing threshold. This characteristic is of great interest in practice as the variations of the spectral purity with the bias current may impose conflicting constrains when tuning operating frequency.

The linewidth of our device has been directly measured by using the self-beating technique. This was allowed by subcavity formation, in which environmental and external noise affecting the cavity optical length is cancelled out. Thus, a long-term linewidth of 2.26 kHz has been measured for our hybrid device [63].

It is worthwhile to mention that the linewidth can be reduced to a sub-kHz by further increasing fiber cavity length.

8.1.3 Stability of the operating wavelength

Using PM-ED fiber to construct the fiber cavity, the energy of the intra-cavity standing wave intensity is constrained within the slow-axis plane throughout the cavity. This increases the probability of upward transitions among upper erbium energy levels based on the ion-ion CET, which is proportional to the intra-cavity power. Consequently, the ion population of the long-lived upper state, $^4I_{13/2}$, is possibly recirculated cooperatively with two upper energy levels, $^4I_{11/2}$ and $^4S_{3/2}$. While non-radiative lifetimes of those two levels are relatively long, 10 µs and 0.8 µs, the standing wave intensity oscillates at a much faster rate within the cavity. This is thought to strengthen the dynamic grating pattern that forms a filter, whose maximum cut-off frequency is ~100 Hz, making the device impermeable to faster instabilities. Also, it resists transient low-frequency disturbances that penetrate the dynamic grating filtering effect, making the device impervious to slow fluctuations affecting the optical cavity length. Such fluctuations may be attributed mainly to thermal fluctuations of the fiber cavity in the case of a packaged device, owing to imperative heat generation associated with non-radiative transitions. However, this explanation cannot be considered a general principle covering other rare earth doped lasers. This thermal noise has been efficiently attenuated by embedding the fiber cavity on a heatsink, placed on an active TEC whose PID loop has been experimentally optimized to eliminate its steady state error. A resolution of 0.6 mK/step has been achieved. Using subcavity formation, the self-beating technique that is insensitive to environmental and external noise has been utilized based on the phase matching condition of the coupled-cavity modes. Eventually, the stability of a packaged device has been inferred to be ±11 Hz for long-term single mode operation [63].

8.1.4 Tunability of the operating wavelength

The tunability has been studied with changing bias current of the SOA and temperature of the fiber cavity including the FBG so that two aspects of frequency tuning have been distinguished;

1. Precision tunability. Although our device has not been packed, it has been demonstrated as a continuously tunable source. This is because the operating frequency has been tuned linearly at a resolution of 2.17 MHz/mA to scan a spectral range of 218 MHz within 298-MHz mode spacing [82].
2. Coarse tunability. The temperature of the fiber cavity, including the external FBG, is altered with a step of ~ 58 mK. The operating mode has been tuned linearly without mode hopping at a resolution of 178.4 MHz/step over a spectral range of 1.784 GHz, which is 6 consecutive mode-spacings. The wavelength-temperature coefficient has been measured to be ~3.062 GHz/K [82].

It is worth mentioning that the dynamic grating, entrenched within the energy levels of Er^{3+}, enables this coarse-tuning of the operating single mode with a high SMSR, which remains more than 40 dB. However, a tunability over a wider range is subject to mode hops unless the external FBG and the fiber cavity are also separately temperature controlled. Also if a better resolution of the coarse tuning is required to scan a smaller range, a better temperature-step resolution can be simply exploited, owing to the linear dependency of frequency on temperature.

In the case of a hermitically packaged device, where the long-term spectral stability of ±11 Hz is estimated, a resolution of ~2.17 kHz/μA can be achieved as the frequency tunes linearly with the drive current. This resolution is then easily transferred to any desired frequency within a spectral range of several mode spacings, scanned by temperature tuning the FBG at a resolution of 178.4 MHz and with a coefficient of ~3.1GHz/K.

The measured specifications of the demonstrated hybrid laser operating under free running conditions are listed in Table 8.1 [63,71,82]. Nevertheless, the listed values may vary with changing fiber cavity length. A related point to consider is that the erbium concentration in the finer cavity also affects some of those values.

Table 8.1: Hybrid laser specifications that have been measured in our laboratory [63,71,82]. The listed values may vary with the fiber cavity length and erbium ions concentration.

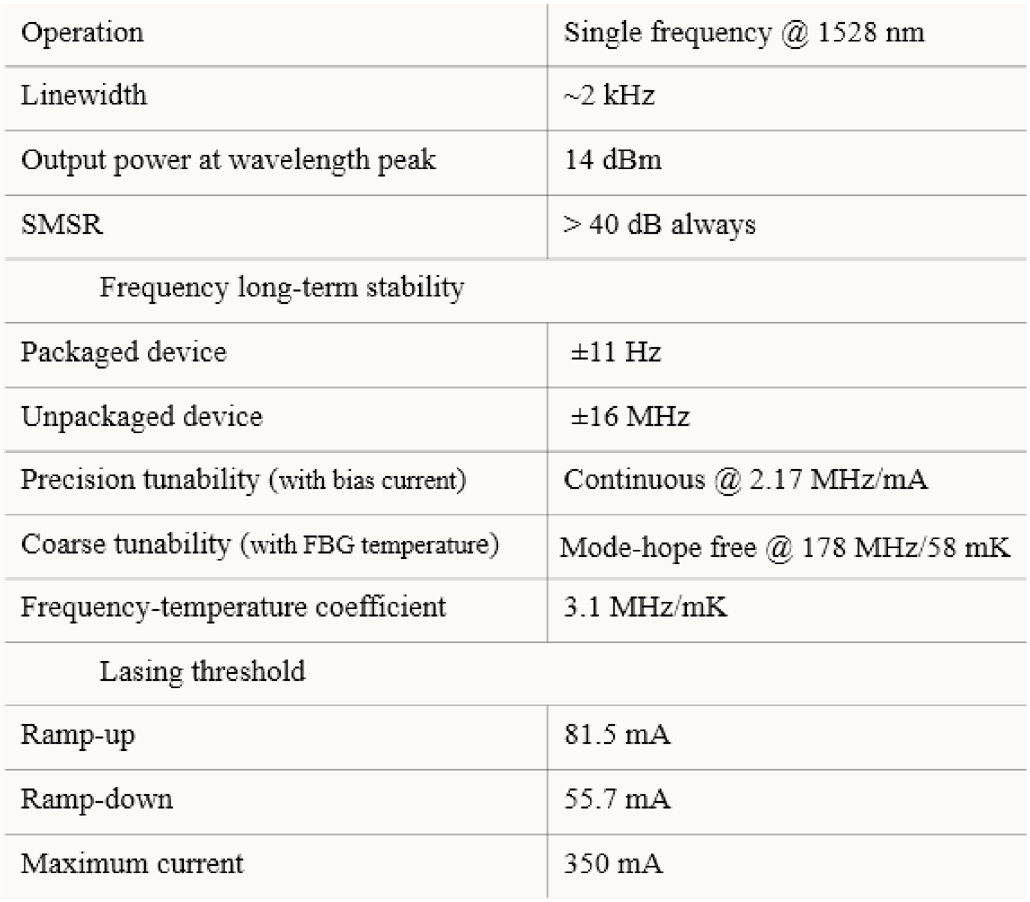

Operation	Single frequency @ 1528 nm
Linewidth	~2 kHz
Output power at wavelength peak	14 dBm
SMSR	> 40 dB always
Frequency long-term stability	
Packaged device	±11 Hz
Unpackaged device	±16 MHz
Precision tunability (with bias current)	Continuous @ 2.17 MHz/mA
Coarse tunability (with FBG temperature)	Mode-hope free @ 178 MHz/58 mK
Frequency-temperature coefficient	3.1 MHz/mK
Lasing threshold	
Ramp-up	81.5 mA
Ramp-down	55.7 mA
Maximum current	350 mA

8.2 Future work

The work, achieved in this thesis, has presented the proof-of-concept highly pure hybrid laser, whose long-term stability is limited to a couple tens of Hz. The dynamic performance, described by the continuous precision and mode-hop free coarse tunability with maintaining an excellent side mode suppression, has been unprecedented for such a hybrid laser operating under free running conditions. The presented work opens the way to a wide range of possibilities for constructing and customizing lasers sources meeting the stringent requirements for many up-to-date technologies. The roles of the fiber cavity length and erbium ion concentration must be understood and systematically developed to be useful tools with the aim of designing and customizing hybrid lasers. Also seeking the optimal performance, other types of SOAs must be tested.

8.3 Potential applications and possible advantages

8.3.1 Potential applications

Due its characteristics, highlighted above in this chapter, the presented hybrid device may have high potential for the following applications.

A) High-end applications for optical communications:

   1. Ideal optical transmitter for systems demanding high stability and precision tunability.
   2. RF photonic and coherent detection systems, e.g., coherent detection employing complex multi-level signals such as 16-quadrature amplitude modulation (QAM) and 64-QAM.
   3. Distributed antenna system (DAS).

B) Fiber-optic sensors:

   1. Distributed strain temperature sensors (DSTS).
   2. Light detection and ranging (LIDAR).
   3. Distributed acoustic sensing.
   4. Coherent optical time-domain reflectometer (OTDR).
   5. Phase shift applications: seismic/pressure/Brillouin.

C) Industrial lasers in medical and pharmaceutical fields.

D) Aircraft and space shuttle communications using light-weight fiber optic cables.

8.3.2 Possible advantages

1. Boost up the performance of many current applications requiring compact, cost effective laser sources operating with higher stability and better wavelength control precision.
2. Eliminate the need for high-frequency feedback control systems adding more complication and expenses.
3. Support multi-service providers and telecommunication companies rolling out fiber-cable networks as a single infrastructure that is scalable for multi-technologies such as 3G, 4G and WiFi.

4. Increase data transmission capacity, demanded by smart applications.
5. In the case of faulty devices, the possibility of replacing the standard SOA and keeping the fiber cavity selecting the operating frequency in transmitter cards may eliminate the implications, associated with customization prior to packaging. This also reduces the requirements for maintenance and inventory of lasers.

REFERENCES

1. G. Ghione, *Semiconductor devices for high-speed optoelectronics* (Cambridge University Press, 2009).
2. F. J. Duarte, *Tunable lasers handbook* (Elsevier Science, 1996).
3. G. Keiser, *Optical fiber communications* (McGraw-Hill, 1983), p. 158.
4. K. Peterman and G. Arnold, "Noise and distortion characteristics of semiconductor lasers in optical fiber communication systems", *in IEEE Transactions on Microwave Theory and Techniques*, vol. 30, no. 4, pp. 543-555, 1982.
5. J. E. Carroll, J. Whiteaway, and D. Plumb, *Distributed feedback semiconductor lasers* (Institution of Electrical Engineers, 1998).
6. O. Svelto, *Principles of lasers* (Springer US, 2010), p.421.
7. H. Kogelnik, C. V. Shank, "Coupled-wave theory of distributed feedback lasers", *Journal of Applied Physics,* vol. 43, no. 5, pp. 2327–2335, 1972.
8. H. Haus and C. Shank, "Antisymmetric taper of distributed feedback lasers", *IEEE Journal of Quantum Electronics*, vol. 12, no. 9, pp. 532-539, 1976.
9. K. Utaka, S. Akiba, K. Sakai and Y. Matsushima, "λ/4-shifted InGaAsP/InP DFB lasers by simultaneous holographic exposure of positive and negative photoresists", *Electronics Letters,* vol. 20, no. 24, pp. 1008-1010, 1984.
10. G. P. Agrawal, *Semiconductor lasers: past, present, and future* (AIP Press, Woodbury, NY, 1995), Ch. 2.
11. W. Demtröder, *Laser spectroscopy: basic concepts and instrumentation* (Springer, 1996), p.251.
12. H. Talvitie, J. Aman, H. Ludvigsen, A. Pietilainen, L. Pendrill, and E. Ikonen, "Improved frequency stability of an external cavity diode laser by eliminating temperature and pressure effects", *Applied Optics.* vol.35, no. 21, pp. 4166, 1996.

13. H. Talvitie, A. Pietilainen, H. Ludvigsen, and E. Ikonen, "Passive frequency and intensity stabilization of extended-cavity diode lasers", *Review of Scientific Instruments*, vol. 68, no. 1, pp. 1-7, 1997.

14. L. Rodriguez-Cobo, M. A. Quintela, S. Rota-Rodrigo, M. López-Amo, and J. M. Lopez-Higuera, "Single-longitudinal mode laser structure based on a very narrow filtering technique", *Optics Express,* vol. 21, no. 8, pp. 10289-10294, 2013.

15. R. E. Bartolo, C. K. Kirkendall, V. Kupershmidt, and S. Siala, "Achieving narrow linewidth low-phase noise external cavity semiconductor lasers through the reduction of 1/f noise", *Proc. SPIE* 6133, pp. 61330I-61330I-8, 2006.

16. Y. Painchaud, M. Aube, G. Brochu, and M. Picard, "Ultra-narrowband notch filtering with highly resonant fiber Bragg gratings", *in Advanced Photonics & Renewable Energy, OSA Technical Digest* (*Optical Society of America*, 2010), paper BTuC3.

17. X. Baillard, A. Gauguet, S. Bize, P. Lemonde, P. Laurent, A. Clairon, et al., "Interference-filter-stabilized external-cavity diode lasers", *Optics Communications*, vol. 266, no. 2, pp. 609-613, 2006.

18. W. H. Loh, R. I. Laming, M. N. Zervas, M. C. Farries, and U. Koren, "Single frequency erbium fiber external cavity semiconductor laser", *Applied Physics Letters*, vol. 66, no. 25, pp. 3422-3424, 1995.

19. K. Y. Liou, Y. K. Jhee, G. Eisenstein, R. S. Tucker, R. T. Ku, T. M. Shen, U. K. Chakrabarti, P. J. Anthony, "linewidth characteristics of fiber-extended-cavity distributed-feedback lasers", *Applied Physics Letters*, vol. 48, no. 16, pp. 1039-1041, 1986.

20. G. Meltz, W.W. Morey, "Bragg grating formation and germanosilicate fiber photosensitivity", *SPIE 1516, International Workshop on Photo-induced Self-Organization effects in Optical Fibre*, (1991), p. 185.

21. E. Brinkmeyer, W. Brennecke, M. Zürn and R. Ulrich, "Fibre Bragg reflector for mode selection and line-narrowing of injection lasers", *Electronics Letters*, vol. 22, no. 3, pp. 134-135, 1986.

22. R. Wyatt, W. J. Devlin, "10 kHz linewidth 1.5 μm InGaAsP external cavity laser with 55 nm tuning range", *Electronics Letters*, vol. 19, no. 3, pp. 110-112, 1983.

23. C. A. Park, C. J. Rowe, J. Buus, D. C. J. Reid, A. Carter and I. Bennion, "Single-mode behaviour of a multimode 1.55 μm laser with a fibre grating external cavity", *Electronics Letters,* vol. 22, no. 21, pp. 1132-1134, 1986.

24. G. Meltz, W. W. Morey, and W. H. Glenn, "Formation of Bragg gratings in optical fibers by a transverse holographic method", *Optics Letters*, vol. 14, no. 15, pp. 823-825, 1989.

25. W. W. Morey, G. Meltz, W. H. Glenn, "Fiber optic Bragg grating sensors", *Proc. SPIE 1169, Fiber Optic and Laser Sensors VII, 98*, 1990.

26. D. M. Bird, J. R. Armitage, R. Kashyap, R. M. A. Fatah and K. H. Cameron, "Narrow line semiconductor laser using fibre grating", *Electronics Letters*, vol. 27, no. 13, pp. 1115-1116, 1991.

27. P. A. Morton, V. Mizrahi, S. G. Kosinski, L. F. Mollenauer, T. Tanbun-Ek, R. A. Logan, D. L. Coblentz, A. M. Sergent, K. W. Wecht, "Hybrid soliton pulse source with fibre external cavity and Bragg reflector", *Electronics Letters,* vol. 28, no. 6, pp. 561-562, 1992.

28. P. A. Morton, V. Mizrahi, P. A. Andrekson, T. Tanbun-Ek, R. A. Logan, P. Lemaire, D. L. Coblentz, A. M. Sergent, K. W. Wecht, P. F. Sciortino Jr., "Mode-locked hybrid soliton pulse source with extremely wide operating frequency range", *IEEE Photonics Technology Letters*, vol. 5, no. 1, pp. 28-31, 1993.

29. P. A. Morton, V. Mizrahi, P. J. Lemaire, T. Tanbun-Ek, R. A. Logan, H. M. Presby, T. Erdogan, S. L. Woodward, M. R. Phillips, A. M. Sergent, and K. W. Hecht, "High-power, narrow-linewidth, stable single-mode hybrid laser", *in Conference on Optical Fiber Communication, Vol. 4 of 1994 OSA Technical Digest Series* (*Optical Society of America*, 1994), paper WG4.

30. C. A. Edwards and H. M. Presby, "Coupling-sensitivity comparison of hemispheric and hyperbolic microlenses", *Applied Optics,* vol. 32, no. 9, pp. 1573-1577, 1993.

31. P. A. Morton, V. Mizrahi, T. Tanbun, R. A. Logan, P. J. Lemaire, H. M. Presby, et al., "Stable single mode hybrid laser with high power and narrow linewidth", Applied Physics Letters, vol. 64, no. 20, pp. 2634-2636, 1994.

32. E. Desurvire, *Erbium-doped fiber amplifiers: device and system developments* (Wiley-InterScience, 2002).

33. S. J. Frisken, "Transient Bragg reflection gratings in erbium-doped fiber amplifiers", *Optics Letters,* vol. 17, no. 24, pp. 1776-1778, 1992.

34. Y. Cheng, J. T. Kringlebotn, W. H. Loh, R. I. Laming, and D. N. Payne, "Stable single-frequency traveling-wave fiber loop laser with integral saturable-absorber-based tracking narrow-band filter", *Optics Letters,* vol. 20, no. 8, pp. 875-877, 1995.

35. F. Timofeev and R. Kashyap, "High-power, ultra-stable, single-frequency operation of a long, doped-fiber external-cavity, grating-semiconductor laser", *Optics Express,* vol. 11, no. 6, pp. 515-520, 2003.

36. R. Liu, I. A. Kostko, K. Wu, and R. Kashyap, "Side mode suppression using a doped fiber in a long external-cavity semiconductor laser operating at 1490 nm", *Optics Express,* vol. 14, no. 20, pp. 9042-9050, 2006.

37. R. Liu, I. A. Kostko, K. Wu, and R. Kashyap, "Stable and continuous wavelength tuning of a hybrid semiconductor laser with an erbium-doped fiber external cavity", *Optics Letters*, vol. 32, no. 12, pp. 1635-1637, 2007.

38. M. Born and E. Wolf, *Principles of Optics* (New York: Pergamon,1987). sec. 8.6.1, eq. (8).

39. R. Kashyap, *Fiber Bragg gratings* (Elsevier Science, 2009).

40. P. E. Dyer, R. J. Farley, R. Giedl, C. Ragdale, D. Reid, "Study and analysis of submicron period grating formation on polymers ablated using a KrF laser irradiated phase mask", *Applied Physics Letters*, vol. 64, no. 25, pp. 3389-3391, 1994.

41. G. Pakulski, R. Moore, C. Maritan, F. Shepherd, M. Fallahi, I. Templeton,G. Champion, "Fused silica masks for printing uniform and phase adjusted gratings for distributed feedback lasers", *Applied Physics Letters*, vol. 62, no. 3, pp. 222-224, 1993.

42. T. Erdogan, "Fiber grating spectra", *in Journal of Lightwave Technology*, vol. 15, no. 8, pp. 1277-1294, 1997.

43. H. M. Presby, A. F. Benner, and C. A. Edwards, "Laser micromachining of efficient fiber microlenses", *Applied Optics*, vol. 29, no. 18, pp. 2692-2695, 1990.

44. H. Ghafoori-shiraz and T. Asano, "Microlens for coupling a semiconductor laser to a single-mode fiber", *Optics Letters,* vol. 11, no. 8, pp. 537-539, 1986.

45. G. Wenke and Y. Zhu, "Comparison of efficiency and feedback characteristics of techniques for coupling semiconductor lasers to single-mode fiber", *Applied Optics*, vol. 22, no. 23, pp. 3837-3844, 1983.

46. H. M. Presby and C. A. Edwards, "Near 100% efficient fibre microlenses", in *Electronics Letters*, vol. 28, no. 6, pp. 582-584, 12 , 1992.

47. C. A. Edwards, H. M. Presby and C. Dragone, "Ideal microlenses for laser to fiber coupling", *in Journal of Lightwave Technology*, vol. 11, no. 2, pp. 252-257, 1993.

48. H. Kogelnik and T. Li, "Laser beams and resonators", *Applied Optics,* vol. 5, no. 10, pp. 1550-1567, 1966.

49. R. K. Luneburg, *Mathematical theory of optics* (Berkeley, CA, University of California Press, 1966).

50. B. E. A. Saleh and M. C. Teich, *Fundamentals of photonics* (New Jersey: John Wiley & Sons, Inc., 2007).

51. L. Thevenaz, *Advanced fiber optics: concepts and technology* (EFPL Press, 2011).

52. J. Noda, K. Okamoto, *et al*., "Polarization-maintaining fibers and their applications", *Journal of Lightwave Technology*, vol. 4, no. 8, pp. 1071-1089, 1986.

53. S. Stepanov, "Dynamic population gratings in rare-earth-doped optical fibres", *Journal of Physics D: Applied Physics*, vol. 41, no. 22, p. 224002, 2008.

54. A. Ghatak and K. Thyagarajan, *An introduction to fiber optics* (Cambridge University Press, 1998). p.290

55. https://www.thorlabs.com/newgrouppage9.cfm?objectgroup_id=3944
56. W. Rideout, R. Holmstrom, J. LaCourse, E. Meland, and W. Powazinik, "Ultra-low-reflectivity semiconductor optical amplifiers without antireflection coatings", *Electronics Letters*, vol. 26, no. 1, pp. 36-38, 1990.
57. https://www.thorlabs.com/thorproduct.cfm?partnumber=SAF1126C
58. R. N. Liu, I. A. Kostko, R. Kashyap, K. Wu, and P. Kiiveri, "Inband-pumped, broadband bleaching of absorption and refractive index changes in erbium-doped fiber", *Optics Communications*, vol. 255, no. 3, pp. 65-71, 2005.
59. H. Statz, C. L. Tang, and J. M. Lavine, "Spectral output of semiconductor lasers", *Journal of Applied Physics,* vol. 35, no. 9, pp. 2581-2585, 1964.
60. M. Yamada and Y. Suematsu, "Analysis of gain suppression in undoped injection lasers", *Journal of Applied Physics,* vol. 52, no. 4, pp. 2653-2664, 1981.
61. A. Yariv, *Quantum electronics* (Wiley, 1989), p.161.
62. Y. Cheng, J. T. Kringlebotn, W. H. Loh, R. I. Laming, and D. N. Payne, "Stable single-frequency traveling-wave fiber loop laser with integral saturable-absorber-based tracking narrow-band filter", *Optics Letters,* vol. 20, no . 8, pp. 875-877, 1995.
63. M. Wahbeh, and R. Kashyap, "Purity of the single frequency mode of a hybrid semiconductor-fiber laser", *Optics Express*, vol. 23, no. 12, pp. 16084-16095, 2015.
64. M. Lax, "Classical noise V. noise in self-sustained oscillators", *Physical Review*, vol. 160, no. 2, pp. 290-307, 1967.
65. O. Svelto *et. al.*, *Lasers and coherent light sources handbook of Lasers and Optics* (New York: Springer, 2007). chapter 11
66. G. P. Agrawal and N. K. Dutta, *Semiconductor lasers* (Van Nostrand Reinhold, 1993).
67. M. Fleming and A. Mooradian, "Spectral characteristics of external-cavity controlled semiconductor lasers", *IEEE Journal of Quantum Electronics*, vol. 17, no. 1, pp. 44-59, 1981.

68. R. Kazarinov and C. Henry, "The relation of line narrowing and chirp reduction resulting from the coupling of a semiconductor laser to passive resonator", *IEEE Journal of Quantum Electronics,* vol. 23, no. 9, pp. 1401-1409, 1987.
69. A. L. Schawlow, and C. H. Townes, "Infrared and optical masers", *Physical Review*, vol. 112, no. 6, pp. 1940-1949, 1958. see eq. 17
70. https://www.usbid.com/datasheets/usbid/2000/2000-q3/ds00165-1.pdf
71. M. Wahbeh, and R. Kashyap, "Ultra-narrow linewidth and highly stable laser for radio over fiber distributed antenna systems", *in 2015 IEEE International Conference on Ubiquitous Wireless Broadband*, Montreal, Canada, Oct. 4-7, 2015. pp.1-4.
72. Y. Sidorin and D. Howe, "Diode-laser-to-waveguide butt coupling: extremely short external cavity", *Applied Optics,* vol. 36, no. 18, pp. 4273-4277, 1997.
73. Y. Sidorin and D. Howe, "Laser-diode wavelength tuning based on butt coupling into an optical fiber", *Optics Letters*, vol. 22, no. 11, pp. 802-804, 1997.
74. A. E. Siegman, *Lasers* (University Science Books, 1986) p. 526.
75. D. Derickson, *Fiber optic test and measurement* (Prentice Hall PTR, 1998), p.187.
76. M. Wahbeh, and R. Kashyap, "Tunability of the highly stable single-frequency mode of a hybrid laser", *Photonics West conference, Laser Source Engineering*, San Francisco, USA, Feb. 13-18, 2016, 9726-59.
77. W. Liang, V. S. Ilchenko, D. Eliyahu, A. A. Savchenkov, A. B. Matsko, D. Seidel, et al., "Ultralow noise miniature external cavity semiconductor laser", *Nature Communications,* pp. 1-6, 2015.
78. C. H. Henry, "Theory of the linewidth of semiconductor lasers"*, IEEE Journal of Quantum Electronics*, vol. 18, no. 2, pp. 259-264, 1982.
79. A. Yariv, *Quantum electronics* (Wiley, 1989) p. 253.
80. M. Fleming and A. Mooradian, "Spectral characteristics of external-cavity controlled semiconductor lasers", *IEEE Journal of Quantum Electronics,* vol. 17, no. 1, pp. 44-59, 1981.

81. E. Pinkas, B. I. Miller, I. Hayashi, and P. W. Foy, "GaAs–AlxGa1−xAs double heterostructure lasers-effect of doping on lasing characteristics of GaAs", *Journal of Applied Physics,* vol. 43, no. 6, pp. 2827-2835, 1972.

82. M. Wahbeh, and R. Kashyap, "Precision tunability of a hybrid semiconductor-fiber laser", On hold due to confidentiality, 2016.

83. http://www.artisantg.com/info/ilx_ldt5910b_manual.pdf

84. C. J. Erickson, M. Van Zijll, G. Doermann, and D. S. Durfee, "An ultrahigh stability, low-noise laser current driver with digital control", *Review of Scientific Instruments*, vol. 79, no. 7, pp. 073107/1-8, 2008.

85. T. Huynh, F. Smyth, L. Nguyen, and L. Barry, "Effects of phase noise of monolithic tunable laser on coherent communication systems", *Optics Express*, vol. 20, no. 26, pp. B244-249, 2012.

86. S. Binetti, S. Chemiakina et. al. "Impact of fiber non-linearity in high capacity WDM systems and in Cross-Connected Backbone Networks." *Photonic Network Communications,* vol. 3, no. 3, pp. 237-243, 2001.

87. N. Massa, *Fundamentals of photonics: fiber optic telecommunication* (SPIE, University of Connecticut, 2000) see Module 1.8, p. 317.

88. X. C. Tong, *Advanced materials for integrated optical waveguides*, (Springer International Publishing, 2013), p.123.

89. P. Blixt, J. Nilsson, T. Carlnas, and B. Jaskorzynska, "Concentration-dependent upconversion in Er $^{3+}$ doped fiber amplifiers: Experiments and modeling", *IEEE Photonics Technology Letters,* vol. 3, no. 11, pp. 996-998, 1991.

90. J. L. Wagener, P. F. Wysocki, M. J. F. Digonnet, H. J. Shaw, and D. J. DiGiovanni, "Effect of concentration on the efficiency of erbium-doped silica fiber lasers", *Proc. SPIE,* pp. 1789, 80-89, 1992.

91. L. F. Johnson, H. J. Guggenheim, T. C. Rich, and F. W. Ostermayer, "Infrared-to-visible conversion by rare-earth ions in crystals", *Journal of Applied Physics,* vol. 43, no. 3, pp. 1125-1137, 1972.

92. J. P. van der Ziel, L. G. Van Uitert, W. H. Grodkiewicz, and R. M. Mikulyak, "1.5-μm infrared excitation of visible luminescent in Y1−xErxF3 and Y1−x−yErxTmyF3 via resonant-energy transfer", *Journal of Applied Physics,* vol. 60, no.12, pp. 4262-4267, 1986.

93. F. E. Auzel, "Materials and devices using double-pumped-phosphors with energy transfer", *in Proceedings of IEEE Conference* (IEEE, 1973), pp. 758-786.

94. E. Desurvire, *Erbium-doped fiber amplifiers: principles and applications* (Wiley-InterScience, 2002), p.285.

95. C. Layne, W. H. Lowdermilk, and M. J. Weber, "Nonradiative relaxation of rare-earth ions in silicate laser glass", *IEEE Journal of Quantum Electronics,* vol. 11, no. 9, pp. 798-799, 1975.

96. C. B. Layne, W. H. Lowdermilk, and M. J. Weber, "Multiphonon relaxation of rare-earth ions in oxide glasses", *Physical Review B*, vol. 16, no. 1, pp. 10-20, 1977.

97. H. Rideout, R. Liu, J. Seregelyi, S. Paquet, and R. Kashyap, "Microwave signal generation using an erbium-doped external cavity laser", *Proc. SPIE 7099, Photonics North,* pp. 70990O-70990O-7, 2008.

98. E. Patzak, A. Sugimura, S. Saito, T. Mukai, H. Olesen, "Semiconductor laser linewidth in optical feedback configurations", *Electronics Letters,* vol. 19, no. 24, pp. 1026-1027, 1983.

99. M. Wahbeh, R. Kashyap, L. Wen-Yi, W. Po-Yi, L. Hai-Han, and J. Seregelyi, "Long term stability of a long intra-cavity saturable absorber external cavity semiconductor laser", *in International Conference on Advanced Infocomm Technology*, (IEEE, 2013), pp. 95-96.